



VNIVERSITAT DE VALÈNCIA

Leptons, top quarks and Higgs bosons in ATLAS: Electron identification with neural networks and $t\bar{t}H(\tau\tau)$ measurements

Tesis Doctoral
Enrique Valiente Moreno

Institut de Física Corpuscular (Universitat de València - CSIC)
Departament de Física Atòmica, Molecular i Nuclear
Programa de Doctorat en Física - 3126

Supervisor:
Dr. Joaquín Poveda Torres

València, Novembre de 2025

Contents

Preface	1
1 Introduction to Standard Model and Higgs Boson Physics	3
1.1 The Standard Model of Particle Physics	3
1.2 The Structure of the Standard Model and the Higgs Mechanism	4
1.2.1 Quantum Chromodynamics	6
1.2.2 Electroweak Theory and Gauge Unification	8
1.2.3 Spontaneous Symmetry Breaking and the Higgs Mechanism	10
1.3 Success and fundamental limitations of the SM	13
1.4 Phenomenology of the Top Quark and the Higgs Boson at the LHC	16
1.4.1 The Top quark	16
1.4.2 The Higgs Boson in the LHC Physics Program	18
1.4.3 The $t\bar{t}H$ process: a gateway to the Yukawa sector	23
1.4.4 Measurements of cross-section and branching ratios: the STXS framework	24
2 The LHC and the ATLAS Experiment	31
2.1 The Large Hadron Collider	31
2.2 The ATLAS detector	37
2.2.1 Reference frames and coordinate system	38
2.2.2 Inner detector	39
2.2.3 Calorimeters	43
2.2.3.1 LAr electromagnetic calorimeter	44
2.2.3.2 LAr hadronic calorimeters	46
2.2.3.3 Tile hadronic calorimeter	46
2.2.4 Muon spectrometer	48
2.2.5 Forward detectors	49
2.2.6 Trigger, Data Acquisition and Detector Control Systems	50

3 Data and simulated samples	55
3.1 Proton-Proton event simulation	55
3.2 Detector response simulation	58
3.3 Monte Carlo simulation generators	59
3.4 Data and MC simulated samples	60
3.4.1 Simulation of electron samples	60
3.4.2 Higgs boson and backgrounds simulated samples	61
4 Physics objects reconstruction	67
4.1 Tracks, vertices and energy clusters	67
4.2 Muons	70
4.3 Jets and flavour tagging	72
4.4 Hadronic tau-leptons	74
4.5 Missing transverse momentum	76
5 Statistical methods	77
5.1 Statistical Modelling	77
5.2 Statistical Inference	78
5.3 Machine Learning Techniques	78
5.3.1 Deep Neural Networks	81
5.3.1.1 Activation functions	82
5.3.1.2 Regularization	83
5.3.1.3 Optimization and Training	84
5.3.1.4 Preprocessing	85
5.3.1.5 Input Data and Preprocessing	85
5.3.2 Boosted Decision Trees	86
6 Electron Reconstruction, Identification and Efficiency Measurements	89
6.1 Electron Reconstruction	90
6.1.1 Cluster Building	91
6.1.2 Track-to-Cluster Matching	92
6.1.3 Superclusters and calibration	93
6.2 Electron Identification	94
6.2.1 Likelihood-based identification	95
6.2.2 Deep neural network for electron identification	97
6.2.2.1 Samples and electrons selection	98
6.2.2.2 Classes	99
6.2.2.3 Inputs and preprocessing	101
Shower-shape variables corrections	104
Preprocessing	106
6.2.2.4 Training procedure	110

6.2.2.5	Electron classification	110
6.2.2.6	Identification Performance	115
6.2.2.7	Tuning and working points definition	116
6.3	Electron Isolation	119
6.4	Electron efficiency measurements	120
6.4.1	Identification efficiency computation	121
6.4.1.1	Z_{mass} efficiency method	122
6.4.2	Identification efficiency measurements: DNN versus LH	128
7	Results	137
8	Conclusion	139
References		141
Appendix		155
List of Acronyms		157

Preface

Here it should be written the preface of this document.

Chapter 1

Introduction to Standard Model and Higgs Boson Physics

The present chapter describes the theoretical frame needed to understand and motivate the physical contents of this thesis. It firstly introduces the Standard Model of particle physics, a theory that describes the foundations that rule the subatomic world.

1.1 The Standard Model of Particle Physics

The Standard Model (SM) of particle physics [1–4] is one of the most successful and rigorously tested theories in modern science. Matured through the second half of the 20th century, it provides an unified quantum field theoretical description of three of the four known fundamental interactions of nature: the electromagnetic, weak, and strong forces. Gravity could not be included in this theoretical framework, as a consistent quantum theory of gravity remains elusive. At its core, the SM is a gauge theory, meaning that the Lagrangian which describes the dynamics and kinematics of the underlying fields is invariant under local gauge transformations (a so called Yang-Mills theory [5]). The group of these gauge transformations is known as gauge symmetry group, that in the case of the SM it is represented by the Lie's symmetry group:

$$SU(3)_C \times SU(2)_L \times U(1)_Y, \quad (1.1)$$

where C is the "colour" charge, L is the weak isospin and Y is the so called hypercharge. Each component corresponds to one of the interactions: the strong

interaction is governed by the non-Abelian $SU(3)_C$ gauge group, known as Quantum Chromodynamics (QCD), while the electroweak interaction unifies electromagnetism and the weak force under the $SU(2)_L \times U(1)_Y$ symmetry.

The fundamental constituents of matter in the SM are the fermions, which are spin- $\frac{1}{2}$ particles following Fermi-Dirac statistics. These particles are organized into three families, each consisting of two quarks and two leptons:

$$\text{1st: } \begin{pmatrix} u \\ d \end{pmatrix}, \begin{pmatrix} \nu_e \\ e \end{pmatrix} \quad \text{2nd: } \begin{pmatrix} c \\ s \end{pmatrix}, \begin{pmatrix} \nu_\mu \\ \mu \end{pmatrix} \quad \text{3rd: } \begin{pmatrix} t \\ b \end{pmatrix}, \begin{pmatrix} \nu_\tau \\ \tau \end{pmatrix} \quad (1.2)$$

Each generation mirrors the same quantum numbers and gauge charges, but differs in mass. Each lepton generation doublet includes an electrically charged particle (l) and a corresponding neutral particle (ν). Leptons are assigned a leptonic quantum number, 1 for leptons and -1 for anti-leptons. Excluding the phenomenon of neutrino oscillations [6, 7], quantum numbers are conserved and therefore the total number of leptons of the same family must remain equal in any particle interaction. It means that leptons can only be created in lepton/anti-lepton pairs of the same family.

Quarks have fractional electric charge, each doublet is formed by a $+2/3$ electric charged up-type quark and a $-1/3$ electric charged down-type quark. The six different types of quarks are referred to as flavours, and these particles have assigned a "colour" quantum number that can be understood as a conserved charge under the SM, analogous to the electric charge. Each flavour of quarks can have any of the three different colours; red (R), green (G) and blue (B), so that there are actually triple the number of quarks shown in Table 1.1. Quarks also have their antiparticle, so called antiquark (\bar{q}) carrying the anti-colours \bar{R} , \bar{G} , \bar{B} . The force carriers, or gauge bosons, arise as a consequence of gauge symmetries of this theory. For QCD, eight massless gluons mediate the strong force between the coloured particles. The electroweak interaction is mediated by W^\pm , Z , and the photon (γ), which result from the mixing of the $SU(2)_L$ and $U(1)_Y$ gauge fields after electroweak symmetry breaking. This mechanism, and the associated generation of particle masses, will be discussed in Section 1.2.3. The properties of gauge bosons and the Higgs boson are presented in Table 1.2.

1.2 The Structure of the Standard Model and the Higgs Mechanism

The Standard Model provides a quantum field theoretical framework describing the three fundamental interactions of nature: strong, weak, and electromagnetic, through gauge symmetries and their associated gauge bosons. In

Fermions (Spin = 1/2)

Leptons				Quarks		
Gen.	Flavour	Charge (e)	Mass	Flavour	Charge (e)	Mass
1st	e	-1	0.511 MeV	d	-1/3	4.7 MeV
	ν_e	0	< 2 eV	u	+2/3	2.2 MeV
2nd	μ	-1	105.7 MeV	s	-1/3	96 MeV
	ν_μ	0	< 0.19 MeV	c	+2/3	1.28 GeV
3rd	τ	-1	1776.9 MeV	b	-1/3	4.18 GeV
	ν_τ	0	< 18.2 MeV	t	+2/3	173.1 GeV

Table 1.1: Fundamental fermions in the Standard Model, grouped by generation. Leptons and quarks are listed with their electric charge and approximate mass values. Neutrino masses are extremely small and not precisely determined.

Bosons (Spin = 0 or 1)

Name	Spin	Charge (e)	Mass (GeV)	Force	Rel. strength
Gluon (g)	1	0	0	Strong	1
Photon (γ)	1	0	0	Electromagnetic	10^{-2}
W^\pm	1	± 1	80.385	Weak	10^{-13}
Z	1	0	91.188	Weak	10^{-13}
H	0	0	125.09	—	—

Table 1.2: Gauge bosons and the Higgs boson in the Standard Model, with their spin, electric charge, mass, associated fundamental interaction (when applicable), and relative interaction strengths. Mass values from Ref. [8].

this section, we review the essential elements of Quantum Chromodynamics, the proton structure relevant for hadron collider physics, the Electroweak Theory, and the Spontaneous Symmetry Breaking mechanism responsible for generating masses via the Higgs field.

1.2.1 Quantum Chromodynamics

The strong interaction is described within the Standard Model by Quantum Chromodynamics (QCD), a non-Abelian gauge theory based on the $SU(3)_C$ symmetry group. It governs the dynamics of quarks and gluons, the fundamental constituents carrying colour charge. Unlike photons in Quantum Electrodynamics (QED), gluons themselves carry colour, leading to self-interactions and a rich non-linear structure.

The QCD Lagrangian is given by:

$$\mathcal{L}_{\text{QCD}} = -\frac{1}{4}G_{\mu\nu}^a G^{a\mu\nu} + \sum_f \bar{\psi}_f (i\gamma^\mu D_\mu - m_f) \psi_f, \quad (1.3)$$

where ψ_f denotes the Dirac field for quarks of flavour f , and $G_{\mu\nu}^a$ is the gluon field strength tensor defined as:

$$G_{\mu\nu}^a = \partial_\mu G_\nu^a - \partial_\nu G_\mu^a + g_s f^{abc} G_\mu^b G_\nu^c, \quad (1.4)$$

with f^{abc} the structure constants of the $SU(3)$ algebra and the coupling constant between quarks and gluons is parametrized by g_s .

Two of the most striking properties of QCD are the asymptotic freedom and colour confinement. At high energies (short distances), the effective coupling $\alpha_s = g_s^2/4\pi$ becomes small, and quarks and gluons behave as quasi-free particles, enabling perturbative calculations. Conversely, at low energies (long distances), the coupling grows, and colour-charged particles cannot exist as free states. This leads to confinement: quarks and gluons are bound into colour-singlet hadrons.

This energy dependence is encoded in the running of the strong coupling constant, scaling at leading order like $\alpha_s(Q^2) \propto \ln(Q^2/\Lambda_{\text{QCD}}^2)^{-1}$, where Λ_{QCD} is the QCD scale parameter, a reference energy scale at which the strong coupling becomes large (typically a few hundred MeV). The logarithmic running reflects the weakening of the interaction at high momentum transfers, a phenomenon known as asymptotic freedom.

Hadrons structure and partons description

In high-energy hadron colliders, the relevant degrees of freedom are not the hadrons themselves but their constituent quarks (valence and sea quarks)

and gluons, collectively referred to as partons. Due to confinement before-hand mentioned, these partons cannot be observed as free particles, but can be probed in hard-scattering processes when the momentum transfer is high enough.

The internal structure of the proton is encoded in the parton distribution functions PDFs, $f_i(x, Q^2)$, which represent the probability density of finding a parton of type i (quark, antiquark, or gluon) carrying a fraction x of the proton's longitudinal momentum when probed at a scale Q^2 . The evolution of the PDFs with energy scale Q^2 is given by the Dokshitzer–Gribov–Lipatov–Altarelli–Parisi (DGLAP) equations [9–11]. Figure 3.1 shows as an example the momentum distributions $xf(x, Q^2)$ of partons in protons. Protons contain two valence *up* and one *down*-quark, which carry significant momentum fractions as visible in the figure. The contributions from sea quarks decreases at higher x .

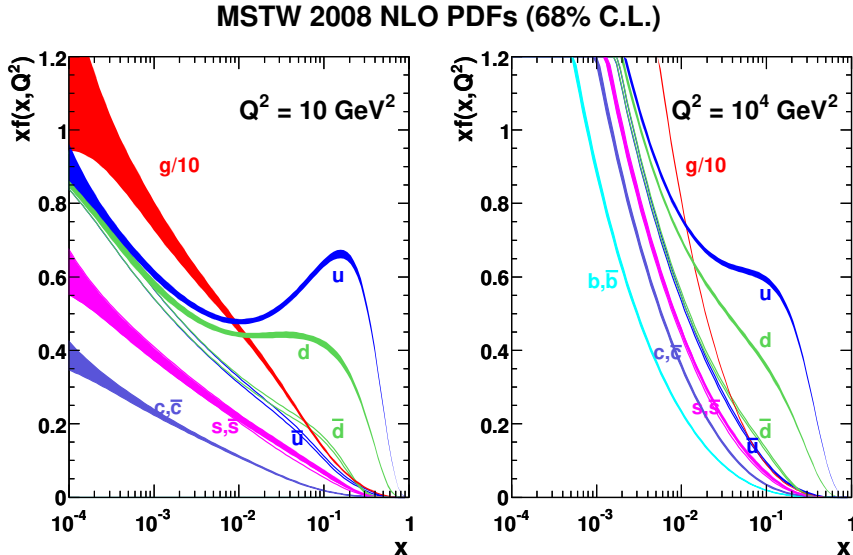


Figure 1.1: Typical momentum fraction distributions of partons inside the proton at a factorisation scale of $Q^2 = 10 \text{ GeV}^2$. The plot shows the gluon and the first two generations of quarks, including valence components u_V and d_V [12].

Parton-parton scattering

From these principles, the cross-sections for the processes that unfold at hadron colliders can be factorized into two contributions. The PDFs describe the col-

liding partons i, j , within the colliding hadrons H_1, H_2 . In the collision, the hard scattering process of interest corresponds to the short-distance interaction between both partons, each carrying a fraction of the parent hadrons's momentum. These interactions are characterised by a large momentum transfer and are described within the framework of perturbative QCD. However, the collision environment also includes soft interactions with low momentum transfer, collectively referred to as the underlying event (UE), which encompasses remnants of the hadron-hadron system as well as potential multi-parton interactions (MPI), which are cases where more than one partonic interaction occurs within a single event.

Radiative processes such as Bremsstrahlung are inherent to high-energy collisions due to the acceleration of colour and electric charges. Initial State Radiation (ISR) arises from the incoming partons before the hard interaction, while Final State Radiation (FSR) originates from the outgoing partons. Following the hard interaction, partons undergo hadronisation, a non-perturbative QCD process in which coloured partons are confined into colour-singlet hadrons. These hadrons are typically collimated into jets, observable in the detector.

Hence, the total cross-section for a given final state X in a pp collision is obtained via the factorisation theorem [13, 14]:

$$\sigma_{AB \rightarrow X} = \sum_{a,b} \int dx_a dx_b f_{a/A}(x_a, \mu_F^2) f_{b/B}(x_b, \mu_F^2) \hat{\sigma}_{ab \rightarrow X}(\hat{s}, \mu_R^2), \quad (1.5)$$

where $f_{a/A}$ and $f_{b/B}$ are the PDFs containing the non-perturbative component of the soft interaction, μ_F is the factorisation scale, and μ_R the renormalisation scale associated with the running of α_s . The partonic cross-section $\hat{\sigma}$ is computed as a perturbative expansion in $\alpha_s(\mu_R)$:

$$\hat{\sigma}_{ab \rightarrow X} = \hat{\sigma}_0 + \alpha_s(\mu_R^2) \hat{\sigma}_1 + \alpha_s^2(\mu_R^2) \hat{\sigma}_2 + \dots \quad (1.6)$$

While leading order (LO) calculations offer basic estimates, they suffer from large theoretical uncertainties due to strong dependence on μ_F and μ_R . Higher-order corrections at next-to leading order (NLO) or next-to-next-to leading order (NNLO) reduce this dependence and yield more accurate predictions. The impact of these corrections is often quantified via the K -factor, defined as the ratio of the NLO to LO cross-sections.

1.2.2 Electroweak Theory and Gauge Unification

The electroweak (EW) theory unifies the weak and electromagnetic interactions within a single gauge framework. It is formulated as a non-Abelian gauge theory based on the symmetry group $SU(2)_L \times U(1)_Y$, where $SU(2)_L$ accounts

for weak isospin and $U(1)_Y$ for weak hypercharge. The theory was developed independently by Glashow, Weinberg, and Salam [15–17], and constitutes a central component of the Standard Model. The electroweak Lagrangian can be written as:

$$\begin{aligned} \mathcal{L}_{\text{EW}} = & \sum_{\text{flavours}} i(\bar{L}\gamma^\mu D_\mu L + \bar{Q}\gamma^\mu D_\mu Q + \bar{l}_R\gamma^\mu D_\mu l_R + \bar{u}_R\gamma^\mu D_\mu u_R + \bar{d}_R\gamma^\mu D_\mu d_R) \\ & - \frac{1}{4}W_{\mu\nu}^a W^{a\mu\nu} - \frac{1}{4}B_{\mu\nu}B^{\mu\nu} \end{aligned} \quad (1.7)$$

The gauge fields associated with $SU(2)_L$ are denoted by $\vec{W}_\mu = (W_\mu^1, W_\mu^2, W_\mu^3)$, while the gauge field corresponding to $U(1)_Y$ is B_μ . The corresponding gauge couplings are g and g' , respectively. The covariant derivative acting on fermion fields is given by:

$$D_\mu = \partial_\mu - i g \frac{\vec{\tau}}{2} \cdot \vec{W}_\mu - i g' \frac{Y}{2} B_\mu, \quad (1.8)$$

where $\vec{\tau}$ are the Pauli matrices and Y is the weak hypercharge of the field.

Left-handed fermions are arranged in $SU(2)_L$ doublets, while right-handed fermions transform as singlets. For instance, the first-generation leptons are written as:

$$L_e = \begin{pmatrix} \nu_e \\ e \end{pmatrix}_L, \quad e_R, \quad (1.9)$$

with L_e transforming as a doublet under $SU(2)_L$ and e_R as a singlet. It similarly applies to left-handed quark doublets, Q , and singlets, u and d . The weak hypercharges are assigned such that the electric charge Q of each field is given by the Gell-Mann–Nishijima relation:

$$Q = T_3 + \frac{Y}{2}, \quad (1.10)$$

where T_3 is the third component of weak isospin.

The kinetic term of the gauge fields is given by:

$$\mathcal{L}_{\text{gauge}} = -\frac{1}{4}\vec{W}_{\mu\nu} \cdot \vec{W}^{\mu\nu} - \frac{1}{4}B_{\mu\nu}B^{\mu\nu}, \quad (1.11)$$

where the field strength tensors are defined as:

$$W_{\mu\nu}^i = \partial_\mu W_\nu^i - \partial_\nu W_\mu^i + g \epsilon^{ijk} W_\mu^j W_\nu^k, \quad (1.12)$$

$$B_{\mu\nu} = \partial_\mu B_\nu - \partial_\nu B_\mu. \quad (1.13)$$

Fermion interactions with the gauge bosons arise from the kinetic term of the fermion fields:

$$\mathcal{L}_{\text{fermion}} = \sum_{\psi} \bar{\psi} i \not{D} \psi, \quad (1.14)$$

leading to charged and neutral current interactions. The charged currents couple only to left-handed fermions via W^{\pm} bosons (linear combinations of W^1 and W^2), while neutral currents arise from couplings to W^3 and B .

At this stage, all gauge bosons and fermions are massless. Mass terms are forbidden by gauge invariance, and it is only through spontaneous symmetry breaking that physical masses are generated, as discussed in the next section. Additionally, the structure of the theory prior to breaking ensures parity violation in weak interactions due to the chiral nature of the $SU(2)_L$ coupling.

This unbroken EW theory thus describes the fundamental structure of weak and electromagnetic interactions prior to the introduction of the Higgs field, which provides masses to the gauge bosons and fermions while preserving gauge invariance through the Higgs mechanism.

1.2.3 Spontaneous Symmetry Breaking and the Higgs Mechanism

In order to generate the mass of weak vector bosons and fermions while preserving renormalizability and unitarity, the Standard Model introduces a Spontaneous Symmetry Breaking mechanism in the electroweak theory. This mechanism is referred to as the Brout–Englert–Higgs (BEH) mechanism [18, 19], and it introduces a complex scalar field doublet ϕ with hypercharge $Y = +1$, whose dynamics are governed by the gauge-invariant Lagrangian:

$$\mathcal{L}_\phi = (D_\mu \phi)^\dagger (D^\mu \phi) - V(\phi), \quad (1.15)$$

where $V(\phi)$ is the scalar potential:

$$V(\phi) = \mu^2 \phi^\dagger \phi + \lambda (\phi^\dagger \phi)^2, \quad (1.16)$$

with $\lambda > 0$ ensuring the potential is bounded from below. The sign of μ^2 determines the nature of the vacuum: for $\mu^2 > 0$, the potential has a single minimum at $\phi = 0$, preserving the gauge symmetry. However, for $\mu^2 < 0$, the potential takes the shape of a “Mexican hat”, as illustrated in Figure 1.2, with a continuous set of degenerate minima.

Since the Lagrangian is gauge invariant, the Higgs field can be described

using an exponential decomposition:

$$\phi(x) = \frac{1}{\sqrt{2}} e^{i\tau_a \theta^a(x)/f} \begin{pmatrix} 0 \\ \rho(x) \end{pmatrix}, \quad (1.17)$$

where $\theta^a(x)$ and $\rho(x)$ are real fields, τ_a are the SU(2) generators¹, and f is a normalisation constant.

One of the degenerate minima can be chosen without loss of generality as:

$$\langle \phi \rangle = \frac{1}{\sqrt{2}} \begin{pmatrix} 0 \\ v \end{pmatrix}, \quad (1.18)$$

which spontaneously breaks the $SU(2)_L \times U(1)_Y$ gauge symmetry down to the electromagnetic subgroup $U(1)_{\text{EM}}$.

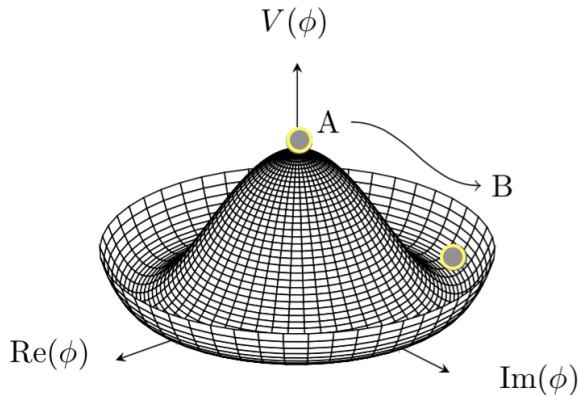


Figure 1.2: Illustration of the shape of the Higgs complex scalar potential with vacuum expectation value v . The symmetry is spontaneously broken when a singular ground state is chosen ($A \rightarrow B$).

The simplest way to expand the Higgs field is to keep the minimum number of degrees of freedom, so replacing $v \rightarrow v + h(x)$ in the previous equation and substituting in the potential Lagrangian (Eq. 1.16):

¹Elements of the group that generate the group when combined with themselves using the group's operations

$$\begin{aligned}\mathcal{L}_H = & \frac{1}{2}(\partial_\mu h)(\partial^\mu h) + \frac{1}{2}(2\mu^2)h^2 \\ & + \frac{1}{2}\frac{g_W^2 v^2}{4}(W_\mu^1 W^{1\mu} + W_\mu^2 W^{2\mu}) \\ & + \frac{1}{8}v^2(g_W W^{3\mu} - g_B B^\mu) \\ & + \mathcal{O}(h^2)\end{aligned}\tag{1.19}$$

This expression contains quadratic terms interpreted as the mass terms of the particles associated to the fields. Since gauge boson terms here are not linearly independent, they cannot be interpreted as observables. Physical bosons can be obtained diagonalizing this sector, resulting in:

$$W_\mu^\pm = \frac{1}{\sqrt{2}}(W_\mu^1 \mp iW_\mu^2),\tag{1.20}$$

$$Z_\mu = \cos\theta_W W_\mu^3 - \sin\theta_W B_\mu,\tag{1.21}$$

$$A_\mu = \sin\theta_W W_\mu^3 + \cos\theta_W B_\mu,\tag{1.22}$$

where θ_W is the weak mixing angle defined by $\tan\theta_W = g_B/g_W$. Using these definitions, the corresponding masses of the gauge bosons can be obtained from the Lagrangian as follows:

$$m_W^\pm = \frac{1}{2}gv,\tag{1.23}$$

$$m_Z = \frac{1}{2}\sqrt{g^2 + g'^2}v,\tag{1.24}$$

$$m_\gamma = 0,\tag{1.25}$$

where $v = 246$ GeV is the Higgs field vacuum expectation value and g is the weak isospin coupling constant. This mechanism results in two massive vector bosons W^\pm which corresponds to the weak charged current, and other massive boson Z , carrier of the neutral weak current. It also remains a massless gauge boson, A_μ , which corresponds to the photon and is consistent with the unbroken QED symmetry $U(1)$.

From eq. 1.19, the mass term for the scalar field H turns to be:

$$m_H^2 = 2\mu^2,\tag{1.26}$$

where it depends on the free parameter μ^2 that can be experimentally measured and it has been done with LHC Run 1 and Run 2 data by ATLAS and CMS [20]:

$$m_H = 125.09 \pm 0.24 \text{ GeV}\tag{1.27}$$

Moreover, the BEH mechanism can also be used to provide mass terms for the fermions preserving the gauge invariance of the theory. Adding the Yukawa terms [21] describing fermion couplings to the Higgs field into the EW Lagrangian, one gets:

$$\mathcal{L}_{\text{Yukawa}} = \sum_{\text{flavours}} \left(-\lambda_\ell \bar{L} \phi \ell_R - \lambda_d \bar{Q} \phi d_R - \lambda_u \epsilon^{ab} \bar{Q}_a \phi_b^\dagger u_R + \text{h.c.} \right) \quad (1.28)$$

where λ_e , λ_d and λ_u are arbitrary parameters and ϵ^{ab} is the two dimensional total anti-symmetric tensor with $\epsilon^{12} = 1$. After symmetry breaking we get the following mass terms for the fermion fields after proper diagonalization:

$$m_l = \lambda_l \frac{v}{\sqrt{2}}, \quad m_d = \lambda_d \frac{v}{\sqrt{2}}, \quad m_u = \lambda_u \frac{v}{\sqrt{2}}, \quad (1.29)$$

from where the Yukawa coupling strength of fermions to the Higgs field can be defined as

$$y_f = \sqrt{2} \frac{m_f}{v} \quad (1.30)$$

Moreover, these fermion mass eigenstates and the weak eigenstates are related via the 3×3 unitary Cabibbo-Kobayashi-Maskawa (CKM) matrix, V_{CKM} ,

$$\begin{pmatrix} d^0 \\ s^0 \\ b^0 \end{pmatrix} = V_{CKM} \begin{pmatrix} d \\ s \\ b \end{pmatrix} = \begin{pmatrix} V_{ud} & V_{us} & V_{ub} \\ V_{cd} & V_{cs} & V_{cb} \\ V_{td} & V_{ts} & V_{tb} \end{pmatrix} \begin{pmatrix} d \\ s \\ b \end{pmatrix}, \quad (1.31)$$

where the off-diagonal elements cause flavour changing weak charged current interactions of quarks with their transition probabilities being proportional to $|V_{nm}|^2$.

1.3 Success and fundamental limitations of the SM

After integrating all the essential elements forming the Standard Model, the theory is characterized by nineteen undetermined parameters:

- a total of nine Yukawa couplings corresponding to the three charged leptons and six quarks,
- three gauge coupling constants governing the strengths of the interactions: g_s , g , and g' ,
- two parameters characterizing the Higgs potential: the vacuum expectation value v and the Higgs boson mass m_H ,
- four resulting mixing angles defining the structure of the CKM matrix,

- a single strong CP-violating phase θ_{CP} , which is conventionally assumed to be zero, implying the absence of CP violation in strong interactions.

Despite being defined by only 19 free parameters, the Standard Model has demonstrated extraordinary predictive power, with theoretical predictions consistently matching experimental results over several decades. This success is exemplified in Figure 1.3, which presents the cross-sections measured by the ATLAS experiment for a variety of processes occurring across multiple orders of magnitude.

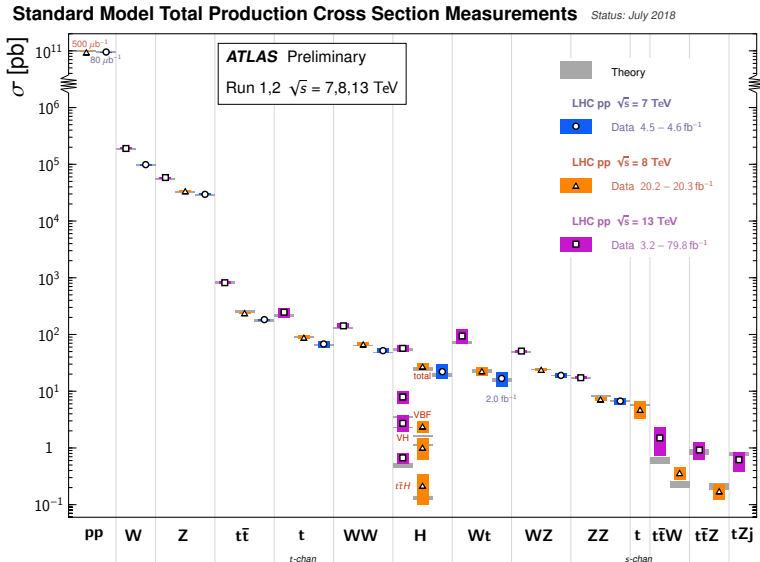


Figure 1.3: Summary of several Standard Model total production cross-section measurements, compared to the corresponding theoretical expectations. All theoretical expectations were calculated at NLO or higher [22].

Open questions

Despite its remarkable success, the SM is not considered a complete theory of fundamental interactions. Some of the most relevant issues that this theory does not address are listed here:

Dark Matter

Astrophysical and cosmological observations provide compelling evidence for the existence of dark matter (DM), a form of non-luminous matter not ac-

counted for in the Standard Model. Measurements of galactic rotation curves, gravitational lensing in galaxy clusters (e.g., the Bullet Cluster [23]), and the cosmic microwave background anisotropies consistently indicate that approximately 85% of the matter content of the universe is non-baryonic [24]. While several extensions of the Standard Model propose viable DM candidates, such as weakly interacting massive particles (WIMP) or axions, the SM itself does not provide a suitable particle to explain these phenomena.

Neutrino Masses and Oscillations

Experimental evidence from solar, atmospheric, reactor, and accelerator neutrino experiments has firmly established that neutrinos undergo flavor oscillations, implying they have non-zero masses and mixings [25]. This observation requires the existence of mass terms beyond the Standard Model's original framework, which assumes massless neutrinos. Mechanisms such as the seesaw model, introducing right-handed neutrinos or Majorana mass terms, are common in theories beyond the SM, but are not present in its minimal formulation.

Matter-Antimatter Asymmetry

The observed universe is dominated by matter over antimatter, a phenomenon known as baryon asymmetry. While the Standard Model includes a source of CP violation through the complex phase in the CKM matrix, it is insufficient to account for the observed phenomena. Additional sources of CP violation and new physics at high energy scales are required to explain this asymmetry.

Hierarchy Problem

The mass of the Higgs boson receives large quantum corrections proportional to the square of the energy cutoff scale of the theory. Stabilizing the Higgs mass at the electroweak scale without unnatural fine-tuning requires a mechanism to cancel these divergences. Supersymmetry, composite Higgs models, and extra-dimensional theories have been proposed as potential solutions, but no evidence of such physics has yet been observed.

Gravity and the Lack of Unification

The Standard Model does not incorporate gravity, which is described by General Relativity. Moreover, the gauge couplings of the SM do not unify at a single energy scale, unless new physics (e.g., supersymmetry) is introduced. A

complete theory of fundamental interactions would require a quantum theory of gravity and a framework capable of unifying all known forces, such as string theory or grand unified theories (GUTs).

Vacuum Stability and the Top Quark Yukawa Coupling

The stability of the (EW) vacuum depends critically on the running of the Higgs self-coupling λ , governed by the renormalization group equations. Among all parameters, the top quark Yukawa coupling y_t has the largest impact due to its sizeable contribution to the β -function of λ .

A large value of y_t tends to drive λ to negative values at high energy scales, which would imply that the EW vacuum is only metastable, with a deeper minimum appearing at large field values. In this case, our universe resides in a long-lived but not absolutely stable vacuum. Current measurements of m_H , α_s , and especially m_t suggest that this is indeed the case.

The precise value of y_t , and thus the top quark mass, is crucial: small shifts can determine whether the vacuum is stable, metastable, or unstable. Accurate measurements of processes such as $t\bar{t}H$ production are therefore essential not only for testing the Standard Model but also for probing its validity up to the Planck scale.

1.4 Phenomenology of the Top Quark and the Higgs Boson at the LHC

The top quark and the Higgs boson play a central role in the (SM) and in the exploration of physics beyond it. Their large masses, unique interactions, and profound implications for electroweak symmetry breaking and vacuum stability make them particularly interesting from both theoretical and experimental perspectives.

1.4.1 The Top quark

The top quark, proposed by Kobayashi and Maskawa in 1973 [26] and discovered at the Tevatron in 1995 [27, 28] is the heaviest known elementary particle, with a mass around 173 GeV. This them to decay into W bosons and b quarks, which always happens before they can form hadrons. They can also decay into other down-type quarks, but due to the CKM matrix, this is practically negligible in practice. Due to its large mass, the top quark has a Yukawa coupling almost equal to unity.

Top quark production

At hadron colliders such as the LHC, the top quark production mostly occurs in pairs ($t\bar{t}$) through the strong interaction. At LO, the two leading subprocesses are gluon-gluon fusion (ggF) and $q\bar{q}$ annihilation, as represented in Figure 1.4. Gluon fusion accounts for roughly 90% of the total $t\bar{t}$ cross-section at a centre-of-mass energy of 13 TeV, which is the practical scenario when protons collide at LHC where gluon parton densities are dominant.

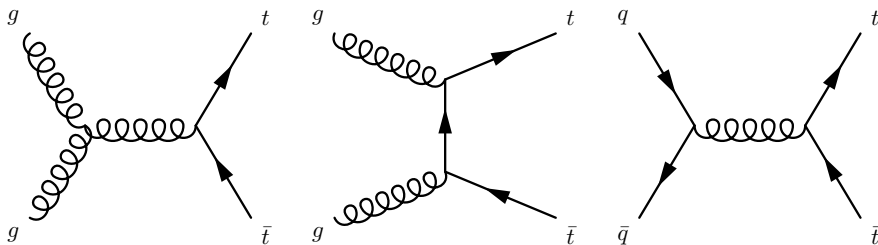


Figure 1.4: Leading-order Feynman diagrams contributing to top quark pair production in hadron colliders. The dominant process at the LHC is gluon-gluon fusion, first and second from the left, while quark-antiquark annihilation (third) dominates at lower center-of-mass energies (Tevatron).

Nevertheless, top quarks can also be produced singly via the electroweak interaction, either alone or in association with other particles. Single-top has a much smaller cross-section, but processes like tW or tH also encapsulate important complementary information. Among all of them, tH and $t\bar{t}H$ play a central role in this thesis by forming the signal processes that are discussed in the last chapters of the thesis. They will be further covered in more detail at the end of this chapter.

Top-antitop system decay

As mentioned, top quarks are mainly produced at hadron colliders in $t\bar{t}$ pairs. Given that the top quark decays nearly 100% of cases as $t \rightarrow Wb$, the properties of $t\bar{t}$ final states mainly depend on how the W boson decays, as it is shown in Figure 1.5.

The fully hadronic final state corresponds to the case where both W bosons decay into quark-antiquark pairs. This is the most frequent decay mode. A smaller fraction of events corresponds to the semileptonic final state, in which one of the bosons decays hadronically, while the other decays leptonically.

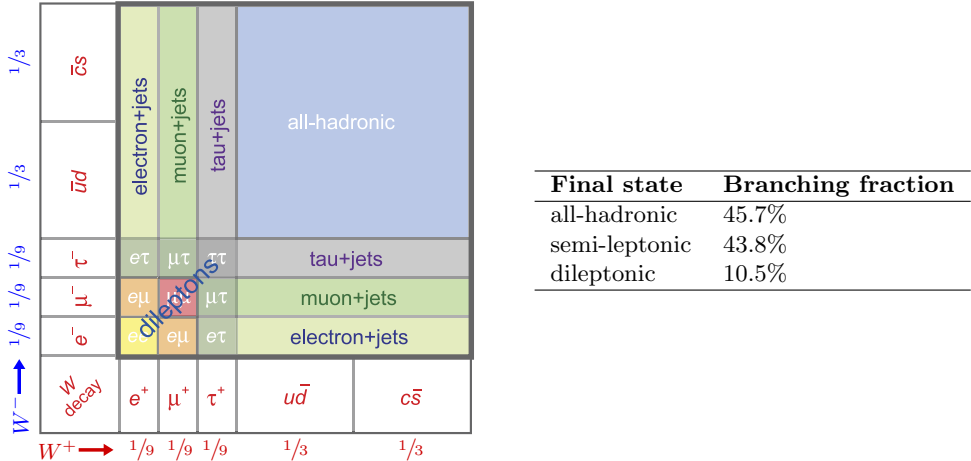


Figure 1.5: Left: classification of $t\bar{t}$ decay channels based on the W decay modes [29]. Right: inclusive branching ratios for the $t\bar{t}$ system decay [8].

producing a charged lepton and a neutrino. In the case of the dileptonic final state, both W bosons decay into leptons.

The table in Figure 1.5 considers τ -leptons within the general category of leptons. However, in the context of physics analysis, it is common for the term "leptonic decay" to be used only to refer to decays into light charged leptons, i.e. electrons and muons, including those from the decay of τ leptons. For experimental reasons, hadronic decays of τ -leptons are treated differently, as discussed in Section 1.4.3.

1.4.2 The Higgs Boson in the LHC Physics Program

Since its discovery in 2012 by ATLAS and CMS [30, 31], the Higgs boson has become a central component of the LHC physics program. Its role in providing masses to the W and Z bosons through the Brout–Englert–Higgs mechanism, and subsequently to all fermions in nature, is a cornerstone of the SM. Studying its properties in detail allows stringent tests of the SM and provides sensitivity to BSM scenarios.

The ATLAS and CMS experiments have undertaken a comprehensive program of Higgs boson measurements. These include the determination of its mass, spin and CP properties, as well as its couplings to fermions and bosons. The precision of these measurements continues to improve with each LHC run, and new production and decay channels are explored regularly.

Higgs boson production mechanisms

The main production modes at tree level in which the Higgs boson can be produced at proton-proton collisions are presented in Figure 1.6. The right plot in Figure 1.7 shows the cross-section as a function of the centre-of-mass energy for a Higgs boson with mass $m_H = 125$ GeV.

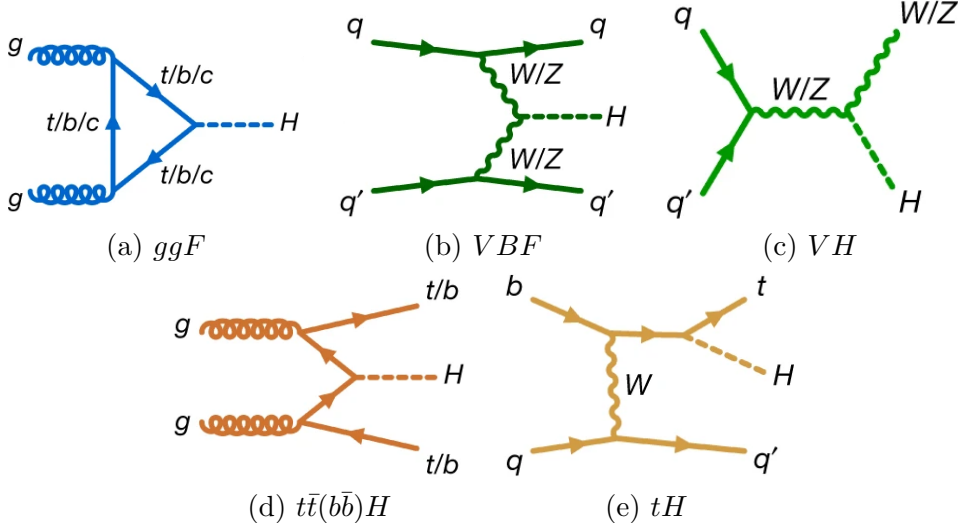


Figure 1.6: Examples of leading order Feynman diagrams for Higgs-boson production modes at the LHC [32].

The dominant production mode is gluon-gluon fusion, where two gluons from the colliding protons interact via a heavy quark loop, primarily involving the top quark, to produce a Higgs boson. This process accounts for about 90% of the total Higgs boson production cross-section at a centre-of-mass energy of 13 TeV, due to the high gluon density within the proton.

Another important channel is vector boson fusion (VBF), responsible of 6.8% of the total cross-section. The Higgs boson is produced via a t -channel exchange of two weak bosons radiated from the incoming quarks, being this mechanism characterized by the presence of two high-momentum hard jets emitted at small angles from the colliding protons, while the Higgs is typically produced between them in the central region, offering a clean and efficient experimental signature.

Associated production with a vector boson (VH), also called "Higgs-strahlung", where the Higgs is produced alongside a W or Z boson, is particularly useful in final states with leptons, providing strong handles for background discrimination in a hadronic environment. It provides around the 4% of the Higgs

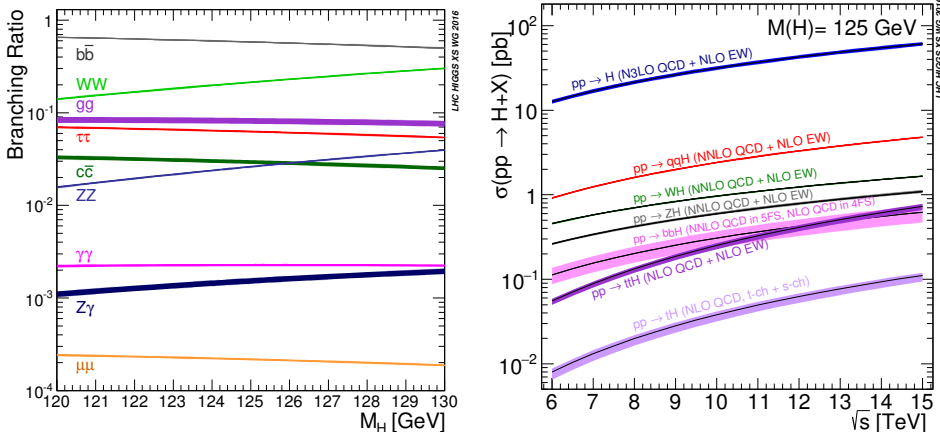


Figure 1.7: (a) Cross-sections measured for Higgs boson production at center of mass energy of 13 TeV as a function of the Higgs boson mass. (b) Branching ratios for the different Higgs boson decay modes as a function of the Higgs boson mass [32]

cross-section.

Finally, the associated production with a pair of top quarks ($t\bar{t}H$) provides a direct probe of the Yukawa coupling between the Higgs and the top quark, the strongest coupling in the SM. Although its cross-section is significantly lower than other channels, around the 0.92%, it plays a strategic role in testing the interaction responsible for the top quark mass generation, which will be discussed in the following. The rarest considered production mode is the associated production with a single top quark, accounting for a 0.16%. This process could also contribute to the determination of the direct top quark Yukawa coupling. However, its cross-section is significantly smaller than that of $t\bar{t}H$ production. Furthermore, additional LO diagrams for tH production involve the W -Higgs coupling, which already blurs the measurement. It is also worth noting that this process is sensitive to the sign of the top quark Yukawa coupling, which causes the interference between the dominant contributing channels to be destructive, hence its small cross-section.

Additionally, there are other production modes that remain experimentally challenging, such as Higgs boson production in association with bottom quark pairs, $b\bar{b}H$. While this mode has a cross-section comparable to that of $t\bar{t}H$, it suffers from a much less clean experimental signature due to the large background contribution from QCD processes.

Higgs boson decay modes

The SM Higgs boson, with a lifetime of approximately 10^{-22} seconds, decays into a wide range of experimentally accessible final states that enable its observation, as its extremely short existence precludes direct detection.

As mentioned in Section 1.2.3, the coupling of the Higgs boson to fermions is proportional to the fermion mass, while for gauge bosons the coupling is proportional to m_Z^2 and m_W^2 in the HZZ and HWW vertices, respectively. Consequently, the Higgs boson decays preferentially into the heaviest particles kinematically allowed.

Figure 1.7 shows the predicted branching ratios for the decay of the SM Higgs boson as a function of its mass. In what follows, we focus on the branching ratios (\mathcal{B}) extracted from the ParticleDataGroup [8] for a Higgs boson with a mass of $m_H = 125.09$ GeV. Representative Feynman diagrams for the dominant decay modes are displayed in Figure 1.8.

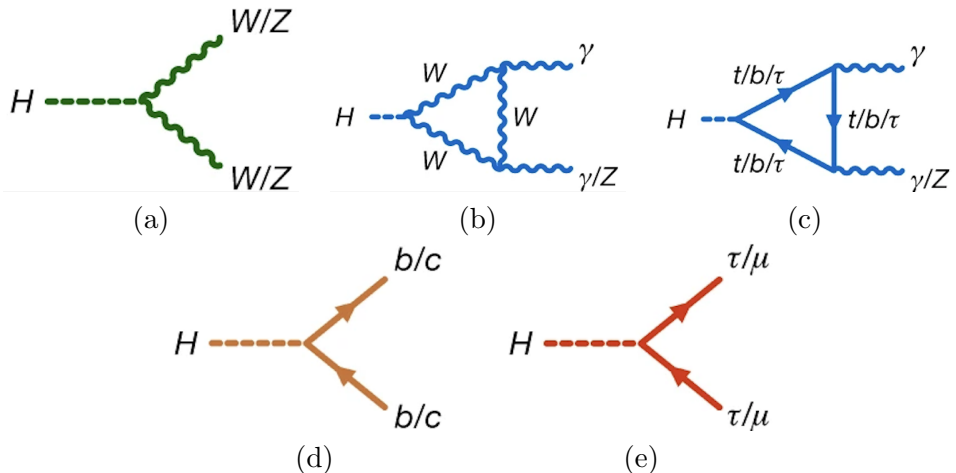


Figure 1.8: Representative LO Feynman diagrams for the main decay modes of a Higgs boson of 125 GeV to (a) a pair of vector bosons, (b) a pair of photons or a Z boson and a photon, (c) a pair of quarks, and (d) a pair of charged leptons [32].

The Higgs boson predominantly decays into a pair of bottom quarks, $H \rightarrow b\bar{b}$, with a branching ratio of approximately $\mathcal{B}(H \rightarrow b\bar{b}) \approx 0.581$. However, the measurement of this decay mode at the LHC is particularly challenging due to the overwhelming background from multijet production. Despite this, its large branching ratio motivates dedicated studies, especially in channels involving the associated production of a Higgs boson with a vector boson, which enhances sensitivity.

Decays into pairs of gauge bosons are suppressed, since at least one of the two bosons must be produced off-shell due to the limited mass of the Higgs boson. The corresponding branching ratios are approximately $\mathcal{B}(H \rightarrow WW^*) \approx 0.22$ and $\mathcal{B}(H \rightarrow ZZ^*) \approx 0.03$. Among these, the $H \rightarrow ZZ^*$ decay mode stands out due to its clean experimental signature and high resolution, as the Z bosons can decay fully leptonically into pairs of electrons or muons that can be efficiently reconstructed and identified in the detector. In contrast, for $H \rightarrow WW^*$, the W bosons can decay hadronically, leading to final states that are more difficult to discriminate from the large QCD background present in hadron colliders like the LHC. Alternatively, they can decay leptonically, resulting in final states with neutrinos that escape detection and complicate the event reconstruction.

The Higgs boson can also decay into a pair of photons, $H \rightarrow \gamma\gamma$, via a one-loop radiative process involving virtual top-antitop quarks or W boson loops. Although this decay has one of the lowest branching ratios, alongside $H \rightarrow Z\gamma$, with $\mathcal{B}(H \rightarrow \gamma\gamma) \approx 0.227\%$ and $\mathcal{B}(H \rightarrow Z\gamma) \approx 0.15\%$, it plays a key role in Higgs boson studies at the LHC due to its excellent signal-to-background ratio. This leads to a very clean experimental signature with high resolution, especially when compared to the background from prompt photon pair production.

The decay into a pair of τ leptons is also possible for the SM Higgs boson, with a branching ratio of approximately 6%. This decay mode plays a central role in this thesis. From the experimental point of view, the $H \rightarrow \tau\tau$ decay presents several challenges. Firstly, the presence of neutrinos in tau decays prevents a full reconstruction of the di-tau final state, complicating the determination of the Higgs boson mass. To overcome this limitation, advanced reconstruction techniques must be employed to estimate the mass of the di- τ system.

Secondly, the $H \rightarrow \tau\tau$ decay is affected by a significant background from $Z \rightarrow \tau\tau$ events, whose production cross-section is several orders of magnitude larger than that of the Higgs boson. Despite these difficulties, this decay channel offers an unique opportunity to probe the Yukawa interaction between the Higgs boson and the tau lepton, providing the most precise measurement of a fermionic coupling to date due to its relatively large branching ratio. Furthermore, it allows for the study of the CP properties of the Higgs boson, both in its production mechanisms and decay, and offers good sensitivity to the vector boson fusion (VBF) production mode.

In the context of the Yukawa sector, the SM also predicts Higgs boson decays to fermions of the first and second generation. The decay into muons, $H \rightarrow \mu\mu$, although having a very small branching ratio of about 0.02%, presents a clean experimental signature with two well-reconstructed muons

in the final state. However, its measurement is significantly affected by the dominant background from the Drell–Yan process. On the other hand, the $H \rightarrow c\bar{c}$ decay has a larger branching ratio of approximately 2.9%, but its measurement at the LHC is hampered by the large QCD multijet background. In addition, the identification of charm quarks remains a difficult task in the environment of a hadron collider. Decays of the Higgs boson to lighter fermions have exceedingly small branching fractions, rendering their direct observation unfeasible with current experimental sensitivity [33].

1.4.3 The $t\bar{t}H$ process: a gateway to the Yukawa sector

As already highlighted in previous sections, the top quark Yukawa coupling, y_t , is the strongest among all Standard Model fermions, owing to the large mass of the top quark. This makes y_t particularly sensitive to possible BSM contributions and an essential parameter to explore the nature of electroweak symmetry breaking [34–37]. Moreover, direct access to y_t is crucial for probing the CP structure of the Higgs sector [38, 39], and plays an indirect role in constraining the Higgs self-coupling [40, 41].

While a direct measurement via the $H \rightarrow t\bar{t}$ decay is not accessible due to kinematic suppression because of top quarks large mass, the associated production of a Higgs boson with a top-quark pair $t\bar{t}H$ offers an unique and direct probe of y_t . Contrary to (ggF), where the coupling appears in a loop and may receive BSM contributions, the $t\bar{t}H$ process provides tree-level sensitivity to y_t . This complementarity is particularly useful when comparing indirect constraints from loop-induced processes to direct measurements [42–44].

The $t\bar{t}H$ production mode was first observed in 2018 by the ATLAS and CMS collaborations [45, 46], following the combination of multiple analyses targeting different Higgs boson decay channels. Among these, the $H \rightarrow b\bar{b}$ and $H \rightarrow \gamma\gamma$ analyses provided the first observations due to their high branching ratio or clean experimental signature, respectively. However, both channels come with significant limitations: the former suffers from large backgrounds with additional b -jets and sizeable modeling uncertainties, while the latter is constrained by its very low branching fraction.

The decay of the Higgs boson to a pair of τ leptons offers an alternative approach that strikes a balance between statistical power and experimental cleanliness. The $H \rightarrow \tau\tau$ branching ratio is significantly larger than that of $H \rightarrow \gamma\gamma$, and although τ leptons are more challenging to reconstruct than electrons or muons, they produce relatively clean final states. Furthermore, $H \rightarrow \tau\tau$ decays provide unique sensitivity to the Yukawa coupling to leptons and to potential CP-violating effects in the Higgs sector.

The analysis of $t\bar{t}H$ production with $H \rightarrow \tau\tau$ decays is typically grouped with other multilepton ($H \rightarrow WW^*, ZZ^*$) final states, due to similarities in event topology. This grouping facilitates background suppression and signal extraction strategies, though it makes the isolation of the di- τ system contribution more challenging.

However, the main analysis presented in this thesis focuses on the case where both τ leptons decay hadronically. This channel is not included within the leptonic or semileptonic categories of the $t\bar{t}H \rightarrow \tau\tau$ analyses, which are integrated into the aforementioned “multilepton analysis”. Instead, it is treated as part of the $H \rightarrow \tau\tau$ analysis, which will be introduced later and combines $t\bar{t}H$ with other production modes, in semileptonic, dileptonic, and fully hadronic final states. In Section ??, it will be exploited the distinctive experimental signature and the potential of this process.

1.4.4 Measurements of cross-section and branching ratios: the STXS framework

Measurements targeting a Higgs boson signal commonly focus on determining a signal strength modifier, denoted as μ . This parameter is defined as the ratio of the measured production cross-section times the branching ratio to the corresponding Standard Model (SM) prediction, i.e.,

$$\mu = \frac{\sigma \times \mathcal{B}}{\sigma_{\text{SM}} \times \mathcal{B}_{\text{SM}}}, \quad (1.32)$$

Such measurements aim to maximize sensitivity to the Higgs boson signal by comparing observed event yields in data to the expected yields from the SM for each of the main Higgs boson production modes.

During the Run 2 period of the Large Hadron Collider (LHC), all the main Higgs boson production and decay modes have been observed with varying degrees of significance. The latest combined results from the ATLAS experiment for production cross-section and decay branching ratio measurements show a remarkable agreement with SM expectations, as illustrated in Figure 1.9, resulting in a measured inclusive signal strength of $\mu = 1.05 \pm 0.06$ [32]. Similar value was obtained by the CMS collaboration [47]. Evidence for rare decay modes, such as $H \rightarrow Z\gamma$ and $H \rightarrow \mu\mu$, has also been reported [48, 49].

Despite their overall success, these inclusive measurements exhibit limited sensitivity to BSM effects that could manifest in specific phase space regions where few signal events are expected. Furthermore, these inclusive analyses depend heavily on theoretical predictions, as the uncertainty in the global signal strength μ is directly influenced by the uncertainties in the SM cross-section and branching ratio calculations that are assumed. Additionally, anal-

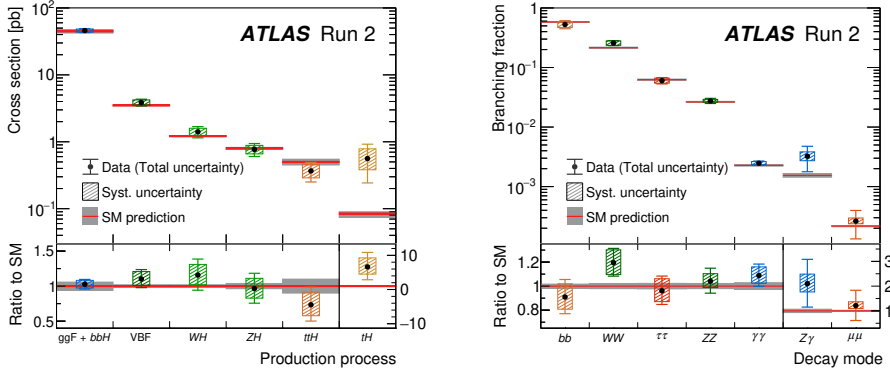


Figure 1.9: Summary of the Higgs boson production cross-section on the left, assuming SM values for the Higgs boson branching ratios, and decay branching ratio measurements on the right assuming SM predictions for the production cross-sections. All results were obtained using ATLAS Run 2 data, combining different analysis and are consistent with the SM predictions within uncertainties [32].

ysis strategies and event selection criteria typically assume SM kinematics for the expected signal, which may reduce sensitivity to BSM scenarios.

An alternative approach to reduce the dependence on SM theoretical extrapolations is the measurement of fiducial cross-sections. In these analyses, a fiducial phase space is defined at particle level², designed to closely resemble the reconstructed event selections to minimize the extrapolation from the measured phase space. Detector effects are corrected via simulation, allowing a direct comparison of the measured fiducial cross-section with theoretical predictions. However, the requirement of similar selections at particle and detector levels often necessitates simplified event selections, which might not be optimal for signal-to-background discrimination. The use of multivariate techniques is typically limited in fiducial measurements due to the complexity of mapping reconstructed variables to particle-level definitions.

Fiducial cross-section measurements can be further extended to differential cross-section measurements, where the production rates are measured as functions of relevant kinematic observables. These measurements provide richer information on the Higgs boson production dynamics and possible deviations from SM predictions.

To find a balance between inclusive and fiducial differential measurements,

²The particle level indicates the level in which all the physical objects are defined using stable particles in their final states, after parton shower and hadronisation, but without any interaction with the detector.

the Simplified Template Cross-Section (STXS) framework has been developed [50]. The STXS framework partitions the Higgs boson production phase space into multiple exclusive regions or bins, each defined by kinematic criteria involving the Higgs boson and associated objects in the final states such as jets or vector bosons. This binning scheme is optimized to enhance sensitivity to possible BSM effects while keeping a reasonable independence and control over theoretical uncertainties.

STXS measurements offer differential information about Higgs boson production, allowing the use of complex multivariate analysis techniques in event selections. This is particularly advantageous for decay channels with challenging final-state reconstruction, such as $H \rightarrow \tau\tau$ or $H \rightarrow b\bar{b}$, where detector resolution and background contamination are more significant compared to cleaner channels like $H \rightarrow \gamma\gamma$ or $H \rightarrow ZZ^*$.

The STXS framework also facilitates the combination of results from analyses targeting different Higgs boson decay modes, maximizing the overall experimental sensitivity. The current binning scheme, referred to as Stage 1.2 and shown in Figure 1.10, refines the granularity introduced in earlier stages (so called Stage 1.1 [51]) to better exploit the available data. A simplified fiducial volume common to all STXS analyses requires the Higgs boson to have rapidity $|y| < 2.5$, matching the typical detector acceptance, where the pseudorapidity is defined as $y = 0.5 \ln \left(\frac{E+p_Z}{E-p_Z} \right)$.

Higgs boson production modes are classified into categories within the STXS scheme, based on the production mechanism and associated particles:

- **Gluon-gluon fusion (ggF):** including the dominant gluon-gluon fusion process and gluon-induced associated production with a Z boson decaying hadronically, $gg \rightarrow ZH \rightarrow q\bar{q}H$. Production of $b\bar{b}H$ is also included here.
- $qq' \rightarrow qq'H$: it includes the Higgs boson production via fusion of vector bosons and quark-initiated associated production of a Higgs boson with a vector boson where the vector boson decays hadronically ($qq' \rightarrow VH \rightarrow qq'H$).
- **Vector boson associated production ($VH \rightarrow (ll, l\nu)H$):** Higgs boson produced in association with a W or Z boson decaying leptonically.
- **Top-associated production ($t\bar{t}H$ and tH):** Higgs boson produced with a top quark pair or single top quark (in a single bin).

Within each category, the STXS bins are further subdivided based on key variables such as the transverse momentum of the Higgs boson (p_T^H) or vector

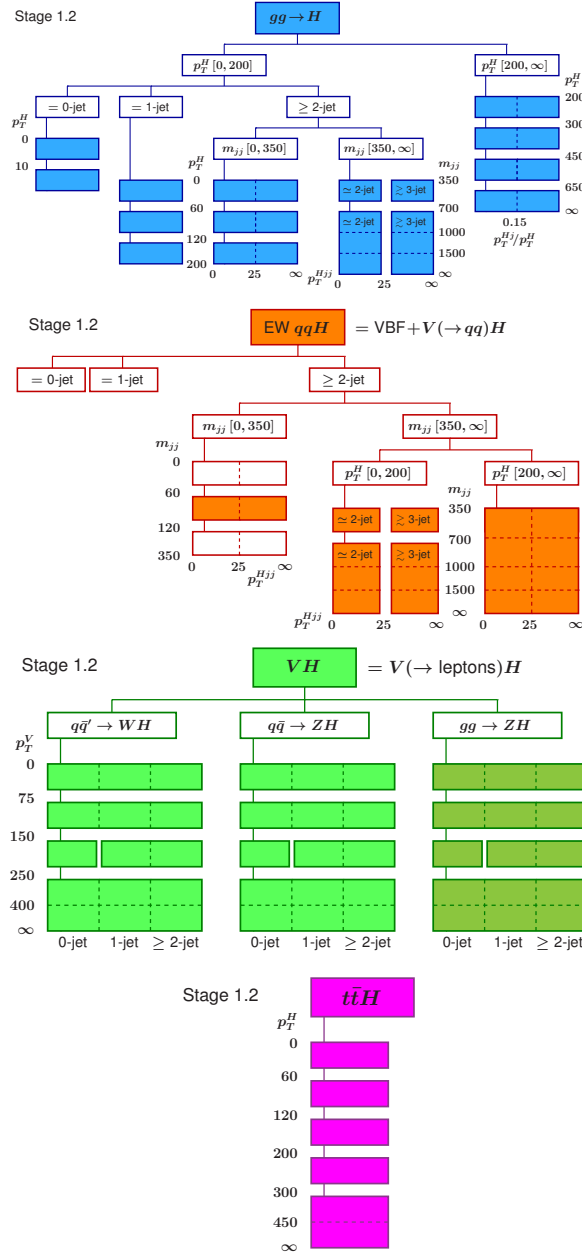


Figure 1.10: STXS stage 1.2 bin definition for (a) gluon-gluon fusion production, (b) vector boson fusion production and associated production with a hadronically decaying vector boson, (c) associated production with a leptonically-decaying vector boson and (d) associated production with a top-antitop quark pair [50].

boson (p_T^V), the number of jets, and the invariant mass of leading jets. The binning scheme is flexible and can be adapted to the experimental sensitivity: bins with insufficient data can be merged, and finer bins can be introduced as more data becomes available.

The latest combination of ATLAS Run 2 data using the STXS framework has produced measurements of the Higgs boson production cross-section in 36 exclusive kinematic regions [32]. The results are consistent with SM predictions, providing stringent constraints on BSM scenarios. Figure 1.11 summarizes these measurements.

This thesis contributes to extending the STXS measurements in the $H \rightarrow \tau\tau$ decay channel, with particular emphasis on the $t\bar{t}H$ production mode. The analysis strategy and detailed results are presented in Chapter ???. Note that the results shown in Figure 1.11 do not yet include the $H \rightarrow \tau\tau$ channel measurements presented in this document.

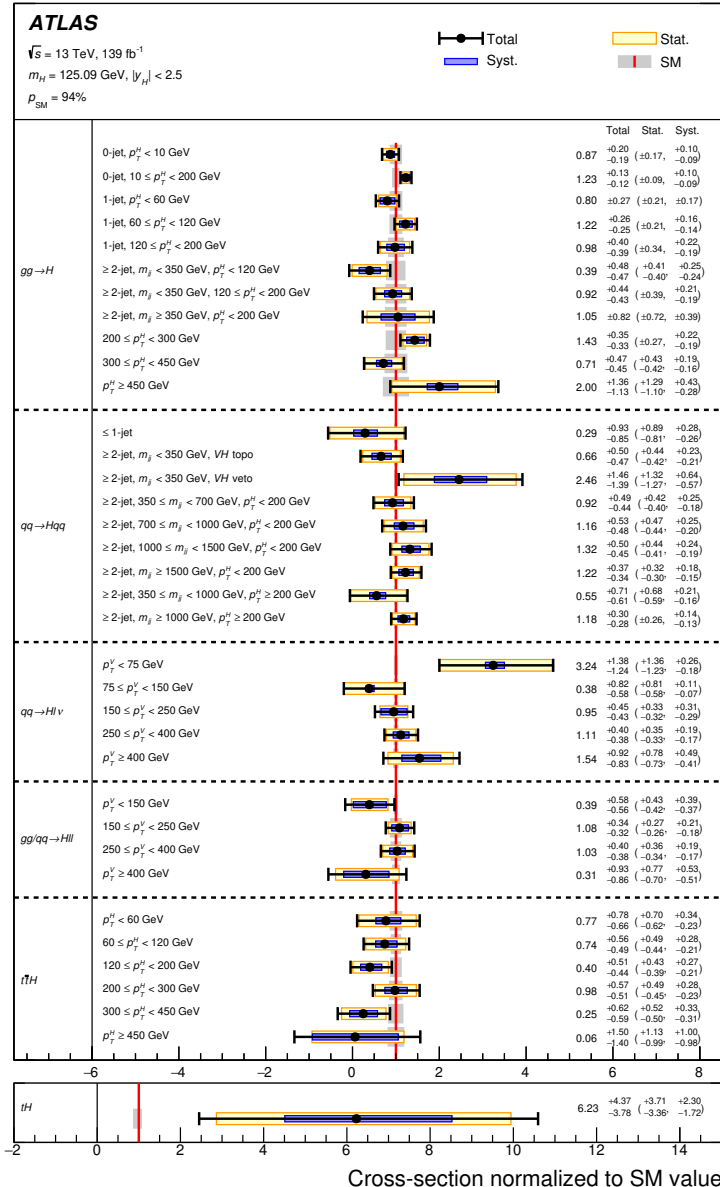


Figure 1.11: Measurement of the Higgs boson production cross-section normalized to the SM predictions in 36 exclusive STXS regions using ATLAS Run 2 data. All these results are obtained assuming SM branching ratios for the Higgs boson decays. The error bars represent the total uncertainty in the measurement (in black), the statistical uncertainty (in yellow) and the systematic uncertainty (in blue) [32].

Chapter 2

The LHC and the ATLAS Experiment

This chapter presents the experimental setup that has made possible the studies discussed throughout this thesis. It introduces the Large Hadron Collider (LHC), a proton–proton collider located at the research complex of the Conseil Européen pour la Recherche Nucléaire (CERN). Subsequently, a description of the ATLAS (A Toroidal LHC ApparatuS) detector is provided, as it is the experiment from which the data used in this analysis have been collected.

2.1 The Large Hadron Collider

The Large Hadron Collider (LHC) is the world’s largest and most powerful particle accelerator, situated at the CERN laboratory near Geneva, on the border between Switzerland and France. Founded in 1954, CERN is a European intergovernmental organization with the primary mission of advancing fundamental research in high-energy physics. It has become a global hub for scientific collaboration, involving over 20 member states and thousands of scientists and engineers from across the world.

The LHC is the flagship project of CERN’s accelerator complex, and represents one of the most ambitious scientific endeavours in history. Its primary goals include performing precision measurements of SM processes in order to be sensitive to any possible deviation, and searching for signs of new physics phenomena beyond the current theoretical framework, such as supersymmetry, extra dimensions, or dark matter candidates, as discussed in Section 1.3. The LHC’s predecessor in the energy frontier was the Tevatron collider at Fermilab (USA), which operated at a centre-of-mass energy of 1.96 TeV. With its de-

sign energy of up to 14 TeV, the LHC has dramatically extended the discovery potential in the high-energy frontier, culminating in landmark achievements such as the discovery of the Higgs boson in 2012 [30, 31].

Overview and layout of the LHC

The LHC is a nearly circular accelerator with a circumference of 27 km, located about 100 m underground [52]. It consists of two counter-rotating beam pipes, each containing a beam of protons (or heavy ions in some cases), which are accelerated to ultra-relativistic energies and made to collide at specific interaction points. These collision points are surrounded by four main detectors: ATLAS, CMS, ALICE, and LHCb, each optimized for different types of physics analyses. While ATLAS [53] and CMS [54] are general-purpose detectors designed to explore a broad range of physics topics, ALICE [55] focuses on the beforehand mentioned heavy-ion collisions to study the quark-gluon plasma, and LHCb [56] specializes in flavour physics and CP violation in the decays of heavy-flavour hadrons.

Protons are injected into the LHC via a complex chain of smaller accelerators. Firstly, hydrogen atoms are ionized and resulting protons are accelerated up to 50 MeV by the linear accelerator, the LINAC2. They are then injected in the Proton Synchrotron Booster (PSB), which is followed by the Proton Synchrotron (PS) and the Super Proton Synchrotron (SPS), ending with the beams of protons reaching energies of 1.4 GeV, 26 GeV and 450 GeV, respectively. All these stages are represented in Figure 2.1. The PS and SPS pack protons to the LHC ring in bunches, which in nominal conditions are separated by 25 ns and a total of 2808 bunches can be finally delivered. Each of these bunches, containing around 10^{11} protons, are kept circulating inside the LHC using superconducting magnets (mainly dipoles and quadrupoles) cooled to 1.9 K with liquid helium. Bending and focusing of the proton beams is needed since, as mentioned, the LHC ring is not really circular, but composed of eight arcs and eight straight sections between them, 520 meters long each. This straight sections connects to the surface installations by lifts, where the main experiments mentioned above are located.

Beam conditions and luminosity

Besides the energy that LHC can deliver to the colliding protons, another important performance characteristic of the accelerator is the number of events it is capable of producing. If one considers the instantaneous luminosity as a measure of the particle flux, then in a scattering process such as proton-proton collisions, the number of collisions can be expressed as:

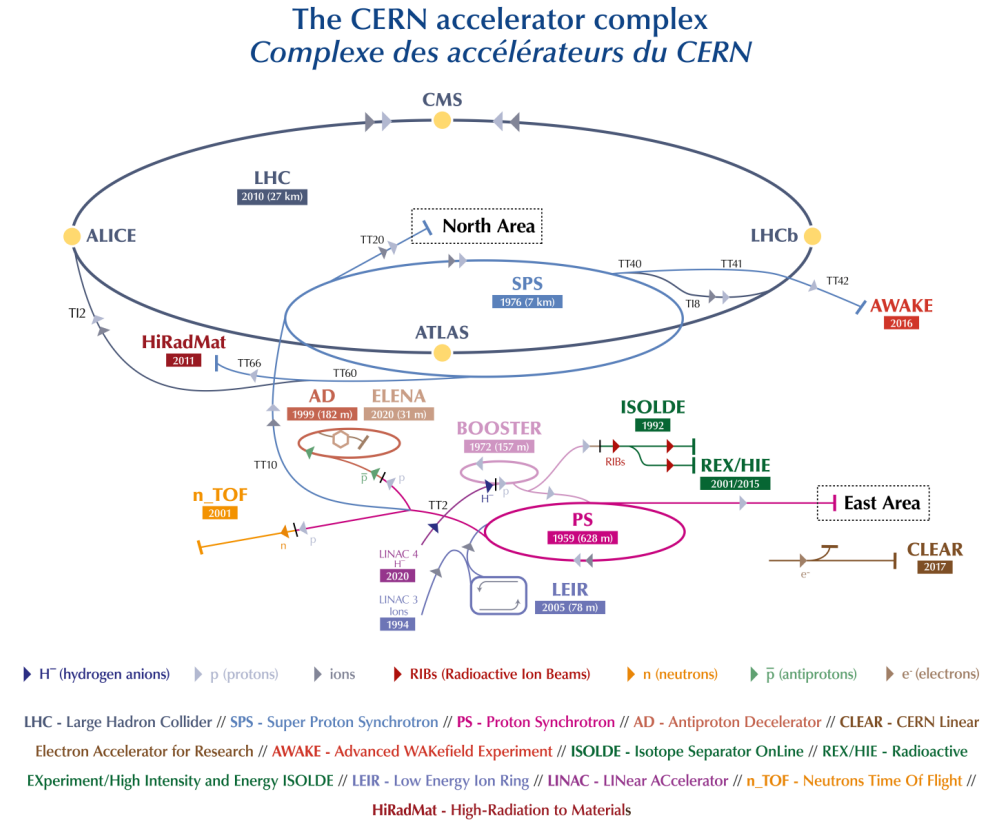


Figure 2.1: Schematic overview of the CERN accelerator complex: the Large Hadron Collider, its injection chain and the four main experiments that record the collisions [57]

$$N_{\text{events}} = \sigma_{\text{event}} \int L dt = \sigma_{\text{event}} \mathcal{L}, \quad (2.1)$$

which is proportional to the cross-section representing the underlying physics of the process of interest, σ_{event} , such as Higgs boson production. The time integral over the instantaneous luminosity is referred to as the integrated luminosity, \mathcal{L} . The instantaneous luminosity depends on the properties of the beams and can be expressed as follows [58]:

$$L = f_{\text{rev}} \frac{N_1 N_2 N_b}{4\pi\sigma_x\sigma_y}, \quad (2.2)$$

where N_b is the number of bunches per beam, N_1 and N_2 are the number of protons per bunch and f_{rev} is the revolution frequency. In practice not all bunches are filled with electrons, and moreover these proton packs have extensions in both two directions perpendicular to the beam propagation direction assuming an effective gaussian shape with area $4\pi\sigma_x\sigma_y$, being σ_x and σ_y the horizontal and vertical gaussian widths respectively.

The integrated luminosity is typically expressed in units of inverse femtobarns (fb^{-1}), where $1 \text{ fb}^{-1} = 10^{39} \text{ cm}^{-2}$. Figure 2.2(a) shows the integrated luminosity delivered to ATLAS for each year of data taking from 2011 to 2025. Figure 2.2(b) displays a comparison between the cumulative luminosity delivered and recorded by the ATLAS detector during Run 2, the data-taking period from 2015 to 2018, which constitutes the main dataset analysed in this thesis, along with the early years of Run 3.

ATLAS collected approximately 147 fb^{-1} of proton–proton collision data at a center-of-mass energy of 13 TeV during Run 2. However, not all delivered data are suitable for physics analysis. The dataset certified for physics-quality analyses, i.e. the one included in the Good Run List (GRL) [59], is slightly smaller due to quality and detector performance criteria. Specifically, ATLAS recorded a total of $140 \pm 1.2 \text{ fb}^{-1}$ of high-quality data during Run 2, and approximately 166 fb^{-1} during the years 2022–2024 of Run 3.

Pile-up and its challenges

As previously mentioned, the proton bunches that collide at the various interaction points (IPs) of the LHC contain a large number of protons. As a consequence, it is common for more than one hard proton–proton scattering to occur in a single bunch crossing. This phenomenon is known as pile-up.

More precisely, we refer to the average number of proton–proton interactions per bunch crossing to quantify this effect, since the number of interactions can vary depending on the beam conditions. Pile-up can be classified into

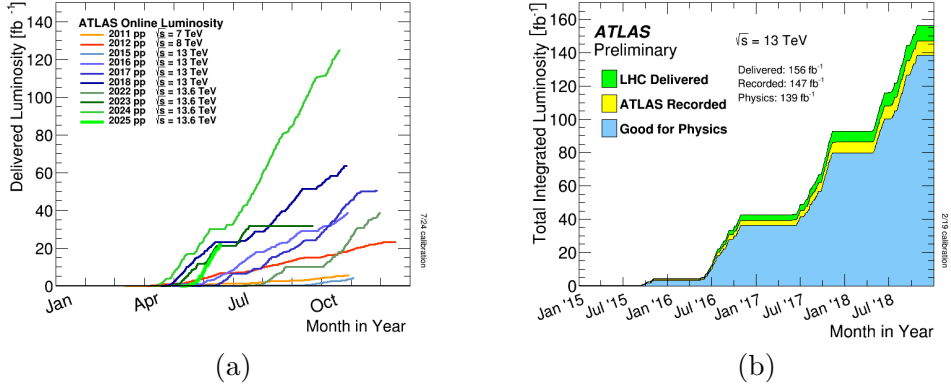


Figure 2.2: (a) Cumulative pp collision luminosity delivered to the ATLAS detector versus month of the year, separately for years between 2011 and 2024 [60] and (b) cumulative luminosity versus time delivered by the LHC (green), recorded by ATLAS (yellow) and used for physics (blue) during stable beams for pp collisions at 13 TeV centre-of-mass energy in years 2015–2018 [61]

two categories: in-time pile-up, which refers to multiple interactions occurring within the same bunch crossing, and out-of-time pile-up, which originates from proton–proton interactions taking place in neighboring bunch crossings. The latter can affect the measurements when the readout times of the detector systems exceed the time interval between consecutive bunches, complicating the identification of the primary vertex and the correct association of final-state particles to it.

The number of interactions per bunch crossing follows a Poisson distribution, with a mean value μ proportional to the product of the total inelastic proton–proton cross-section σ_{inel} and the instantaneous luminosity [62]

$$\mu = \frac{L_{\text{bunch}} \sigma_{\text{inel}}}{f_{\text{rev}}} . \quad (2.3)$$

Figure 2.3 shows the distribution of this mean number of interactions per bunch crossing during both Run 2 and Run 3 data-taking periods of ATLAS. Increasingly efforts are being devoted to develop mitigation strategies for this effect, especially thinking about future scenarios as the HL-LHC, including advanced pile-up suppression techniques, such as vertex association, pile-up subtraction in jets and missing energy, and the use of machine learning algorithms to distinguish primary vertices from pile-up vertices [63–65].

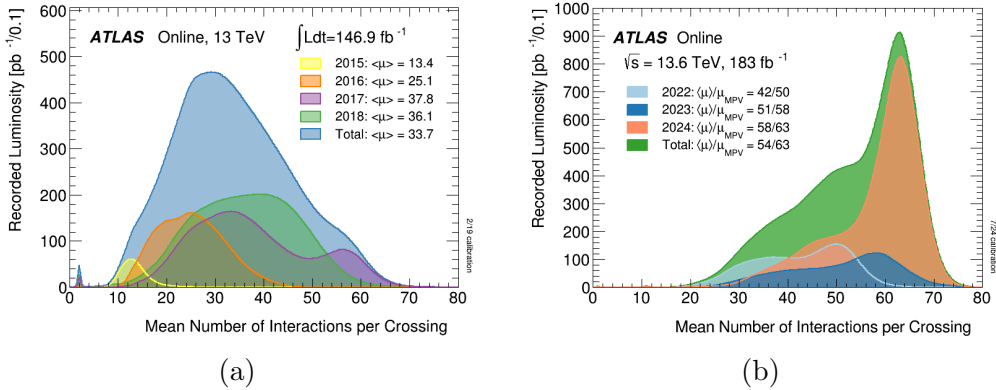


Figure 2.3: (a) Distribution of mean number of interactions per bunch crossing in data recorded by the ATLAS experiment at 13 TeV during Run 2 [61] and (b) at 13.6 TeV during Run 3 [61] data-taking periods.

LHC upgrade plans

To further push the frontiers of high-energy physics and enhance the physics reach of the LHC programme, a major upgrade of the collider and its experiments is underway. The High-Luminosity LHC (HL-LHC) project [66] aims to increase the integrated luminosity delivered to the experiments by more than an order of magnitude, targeting up to 3000 fb^{-1} of proton–proton collision data by the end of the next decade.

This increase in data volume will significantly improve the statistical precision of measurements of rare processes and enable detailed studies of the Higgs boson properties, electroweak interactions, and potential signals of physics beyond the Standard Model. In particular, the HL-LHC will allow for precise measurements of Higgs boson couplings, self-interactions, and rare decays, as well as the potential observation of extremely suppressed processes such as flavour-violating decays or double Higgs production.

Achieving the HL-LHC goals requires a broad range of upgrades to the accelerator complex and its associated infrastructure. Key improvements include the installation of new high-field superconducting quadrupole magnets near the interaction points, based on advanced Nb₃Sn technology [67], which will allow for a reduction in the beams width, and consequently, an increase in luminosity. Additionally, new cryogenic and collimation systems will be implemented to handle the increased beam power and radiation levels.

On the experiment side, all main LHC experiments, including ATLAS, are undergoing substantial upgrades to handle the harsher conditions of HL-LHC operation. These include the development of new inner trackers with extended

radiation hardness and granularity, the replacement of calorimeter and muon chamber readout electronics to support higher data rates, and a completely redesigned trigger and data acquisition system. The upgraded detectors must be capable of maintaining excellent performance in the presence of average pile-up levels exceeding $\langle \mu \rangle \sim 140$, more than a factor of two higher than those typically encountered during Run 3.

The HL-LHC project is expected to start operations by 2029, following the completion of the Long Shutdown 3 (LS3). It represents the next major milestone in the LHC physics programme, with the potential to open a new era of precision measurements and exploration of the unknown.

2.2 The ATLAS detector

Having already outlined the design, physics programme and scientific goals of the LHC experiment, this section presents in detail each of the main components that make up the ATLAS detector.

ATLAS (A Toroidal LHC ApparatuS) [53, 68] is a general-purpose detector designed to explore a wide spectrum of physics phenomena, ranging from precision tests of the Standard Model to searches for new particles and interactions beyond it. It is the largest detector ever constructed for a collider experiment, with a cylindrical geometry approximately 44 m long, 25 m diameter, and weighing over 7000 tons. Its conception, design and construction were carried out by a global collaboration of more than 3000 scientists and engineers from around 180 institutions in nearly 40 countries.

Data-taking with ATLAS began in 2009, when the LHC first delivered proton-proton collisions. Since then, the detector has been instrumental in several landmark achievements, most notably the discovery of the Higgs boson in 2012. The ATLAS detector is composed of multiple subdetectors arranged in concentric layers around the interaction point. The cylindrical structure is closed by two end-caps, providing almost 4π coverage of the solid angle. An illustration of the ATLAS detector can be found in Figure 2.4.

The different ATLAS subsystems are designed to measure the properties of different types of particles. In the innermost region, closest to the interaction point, the inner detector is built to record the properties of charged particles produced in the collisions. Their trajectories are bent by a 2 T magnetic fields produced by a superconducting solenoid. Then, the inner detector is surrounded by the calorimeter system which is in charge of measuring the energy of particles that can produce electromagnetic and hadronic showers in the detector. It is striped in a liquid argon electromagnetic calorimeter and a hadronic calorimeter composed by a scintillating barrel and liquid argon

end-caps. In the outermost region of the detector it is placed the muon spectrometer, devoted to the measurement of muons produced in the collision and which are bent by a 4 T magnetic field produced in this case by a toroidal magnet system. The following sections describe the purpose and operating principles of these components in detail, as well as the forward detectors and the trigger and data acquisition system.

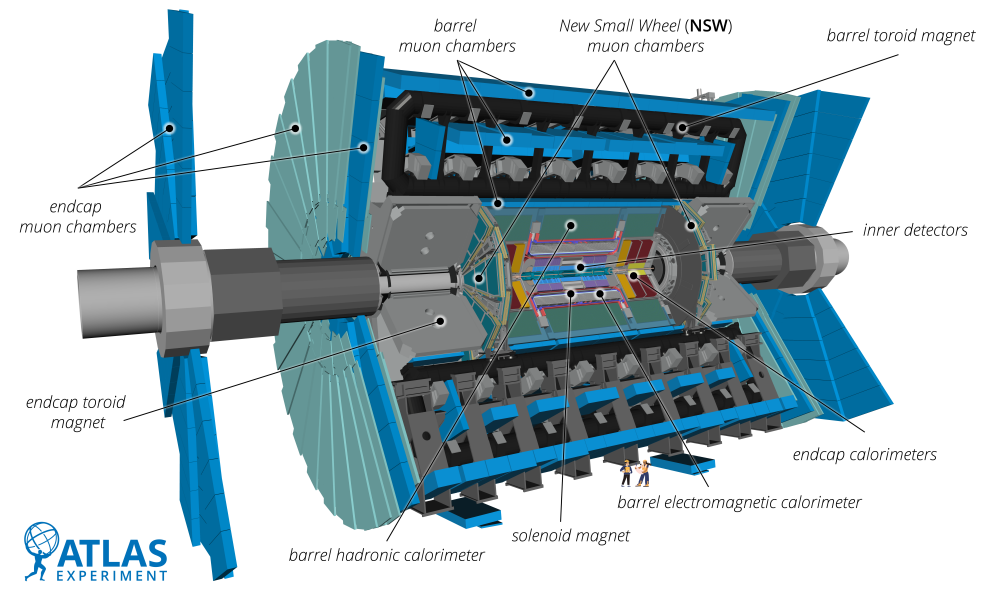


Figure 2.4: Cut-away view of the Run 3 configuration of the detector indicating the locations of the larger detector sub-systems [69].

2.2.1 Reference frames and coordinate system

The ATLAS experiment adopts a right-handed coordinate system, centered at the nominal interaction point (IP) where the proton–proton collisions take place. The origin of the coordinate system lies at the geometrical center of the detector. The z -axis is defined along the beam pipe, pointing in the direction of the anti-clockwise beam. The x -axis points from the IP towards the center of the LHC ring, while the y -axis points upwards, completing a right-handed coordinate system. The transverse plane defined by x and y directions locate important observables like the transverse momentum (p_T) and the so-called missing transverse momentum (E_T^{miss}).

In addition to the Cartesian coordinates (x, y, z) , a cylindrical coordinate system is often used due to the symmetry of the detector. In this system, the transverse plane is defined by the coordinates (r, ϕ) , where r is the radial

distance from the z -axis and ϕ is the azimuthal angle measured around the beam pipe. The longitudinal direction remains aligned with the z -axis.

To describe the polar angle of a particle's trajectory, defining deviations from the beam direction, the rapidity y is preferred over the polar angle θ , as it is invariant under Lorentz boosts along the z -axis:

$$y = \frac{1}{2} \ln \frac{E + p_Z}{E - p_Z}, \quad (2.4)$$

where E is the particle's energy and p_Z the longitudinal component of its momentum. In the ultra-relativistic limit, this variable can be approximated by the so-called pseudorapidity, η , since the mass of most of final-state particles is mostly negligible against their momenta:

$$\eta = -\ln \tan \left(\frac{\theta}{2} \right). \quad (2.5)$$

In this frame, if a particle is emitted in the beam direction, $\theta \rightarrow 0$, it would have assigned $\eta \rightarrow \infty$, while if it follows a direction perpendicular to the beam, $\theta = 90^\circ$ corresponds to $\eta = 0$. The angular distance between two objects in the detector is typically measured using the ΔR metric in the (η, ϕ) plane:

$$\Delta R = \sqrt{(\Delta\eta)^2 + (\Delta\phi)^2}. \quad (2.6)$$

This coordinate convention is used throughout the analysis and the design of the detector subcomponents, as well as in reconstruction and identification algorithms for physics objects such as jets, leptons, and missing transverse energy. It is illustrated in Figure 2.5.

2.2.2 Inner detector

The Inner Detector (ID) [71, 72] is the central tracking system of the ATLAS experiment and plays a fundamental role in the reconstruction of charged particles emerging from proton-proton collisions. It is the innermost component of the detector, positioned directly around the interaction point, and it is enclosed within a thin superconducting solenoid that generates a 2 T magnetic field parallel to the beam axis. This magnetic field bends the trajectory of charged particles in the ϕ direction, which allows the determination of their charge and momentum due to this curvature.

The ID is composed of three complementary subdetectors arranged in layers from the innermost to the outermost radii: the Pixel Detector, the Semiconductor Tracker (SCT), and the Transition Radiation Tracker (TRT). The Pixel and SCT systems are based on silicon technologies and are optimized for high

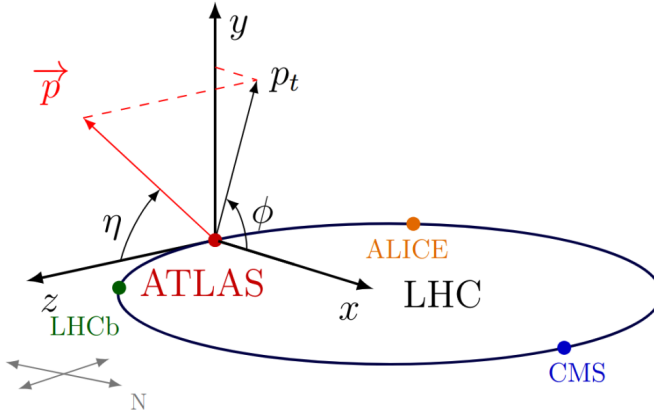


Figure 2.5: Illustration of the ATLAS coordinate system. Image obtained from Ref. [70].

spatial resolution and precision tracking, particularly near the primary vertex, which is the measured spatial location where the hard scattering of partons of interest in a given event took place. In contrast, the TRT is a gaseous detector made of straw tubes and is designed to extend the tracking capabilities at higher radii while also enhancing electron identification through the detection of transition radiation.

Together, these three subdetectors span a cylindrical volume of approximately 6.2 m in length and 2.1 m in diameter, and provide tracking coverage in the pseudorapidity range of $|\eta| < 2.5$. The layout of the ID is divided into a central barrel region ($|\eta| < 1.4$) and two symmetric endcap sections ($1.4 < |\eta| < 2.5$). As charged particles traverse the ID, they produce hits in the different layers, which are then used to reconstruct their trajectories with high efficiency and resolution. This track information is vital for identifying not only primary vertices, but other vertices that are displaced from the primary one and could originate from the decay of heavy-flavour hadrons that travel enough before decaying. This is clearly essential for tagging of these jets, and supporting particle identification algorithms throughout the ATLAS reconstruction chain, as will be explained in Chapter 4. An schematic view of the barrel section of the ID can be found in Figure 2.6.

Pixel detector

The Pixel Detector is the innermost and most granular component of the ID. Its layout consists of three cylindrical layers of silicon pixel sensors in the

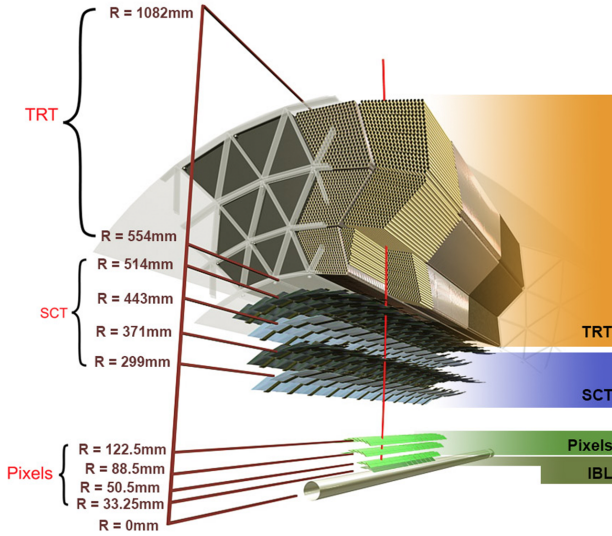


Figure 2.6: Cutaway representation of the barrel section of the ATLAS inner detector. From the innermost to the outermost layers, it shows the pixel detector, the four cylindrical and concentrical layer of the SCR and the straw tubes characteristic of the TRT [73].

barrel region, positioned at radial distances of 50.5, 88.5, and 122.5 mm, and three disks per endcap located at $z = \pm 495$, 580, and 650 mm. The sensors in these layers have pixel sizes of $50 \times 400 \mu\text{m}^2$ and a thickness of 250 μm . This geometry yields a spatial resolution of about 10 μm in the $r-\phi$ plane and 115 μm in z for the barrel region, and the opposite in the endcaps, where resolution is optimized along z .

In preparation for Run 2, an additional innermost layer known as the Insertable B-Layer (IBL) [74] was installed at a radius of 33.25 mm. The IBL significantly improved the impact parameter resolution, particularly for low- p_T tracks. It is composed of both planar and 3D silicon sensors with reduced pixel dimensions of $50 \times 250 \mu\text{m}^2$ and sensor thicknesses of 250 μm and 200 μm , respectively. The closer proximity of the IBL to the beamline and its finer segmentation improves its ability to separate primary and secondary vertices even under high occupancy conditions, which is crucial for the identification of jets originating from heavy-flavour quarks.

During Run 3, the Pixel Detector has been operating under increasingly harsh radiation environments and elevated levels of pile-up. These conditions challenge the performance and life-time of the system, especially the innermost layers. Dedicated calibration and alignment strategies, as well as enhanced

readout electronics, are employed to preserve the resolution and efficiency of tracking throughout this demanding phase of operation.

Semiconductor Tracker (SCT)

Outwards, the SCT subdetector follows the pixel one, consisting of four barrel layers and nine disks in each endcap, built with silicon microstrip modules. Each module includes two sensors, mounted back-to-back at a small stereo angle of 40 mrad, enabling precise 3D position reconstruction of $17\text{ }\mu\text{m}$ resolution in the transverse plane and $580\text{ }\mu\text{m}$ in the longitudinal direction. The SCT contains around 6 million readout channels.

Transition Radiation Tracker (TRT)

The TRT is the outermost component of the Inner Detector and extends tracking capabilities up to $|\eta| < 2.0$, complementing the precise position measurements from the inner silicon detectors with additional points along the track path. The TRT also provides particle identification (PID) capabilities, particularly useful for electron-pion discrimination via detection of transition radiation photons.

It consists of a large number of thin straw tubes, 52,544 in the barrel region and 122,880 in the two endcaps, each with a diameter of 4 mm. These tubes are originally filled with a gas mixture of 70% xenon, 27% carbon dioxide, and 3% oxygen. When a charged particle traverses a straw, it ionizes the gas along its path. A high negative voltage applied to the tube walls causes the liberated electrons to drift toward a central anode wire, producing a detectable signal.

The TRT delivers a spatial resolution of approximately $130\text{ }\mu\text{m}$ in the $r-\phi$ plane and contributes on average about 30 measurement points per track, thus enhancing the momentum resolution and the track reconstruction efficiency, especially for high- $|\eta|$ regions where fewer silicon hits are available. Its ability to identify transition radiation, photons emitted by relativistic electrons crossing dielectric boundaries embedded in the tracker, provides an additional layer of particle identification crucial for several physics analyses.

During Run 3, it has been used an argon-based gas mixture in the entire barrel and part of the end-cap region to minimize xenon loss and ensure gas stability. Although this reduces the barrel's PID performance due to weaker transition radiation photon absorption, it still provides useful electron identification when combined with dE/dx information. The end-cap PID performance remains largely preserved [75].

At this stage it is worth noting that, ahead of Run 3, an important part

of the read-out electronics in several sub-detectors were refurbished and optimised to withstand the higher data rates expected during this period. By the end of Run 3 the existing silicon trackers will be operating close to their radiation-tolerance limits, and the TRT will no longer be able to function under the nominal HL-LHC conditions. To preserve vertex-tagging and track-reconstruction performance, the entire Inner Detector will therefore be superseded by an all-silicon Inner Tracker (ITk). In addition, a High-Granularity Timing Detector will be installed in the forward region in order to match tracks with calorimeter clusters using precise time information, that is an essential tool for mitigating the extreme pile-up foreseen at the HL-LHC [76]

2.2.3 Calorimeters

Moving outwards again, beyond the solenoid magnet containing the Inner Detector, we find the ATLAS calorimeter system [77, 78], which fully encloses the previously described components. Both types of calorimeters, electromagnetic and hadronic, cover a total range up to $|\eta| < 4.9$, allowing for the measurement of the energy of particles traversing them, as they are nominally designed to completely absorb the energy of most particles predicted by the SM, except for muons and neutrinos. An schematic illustration of the ATLAS calorimeter system is shown in Figure 2.7.

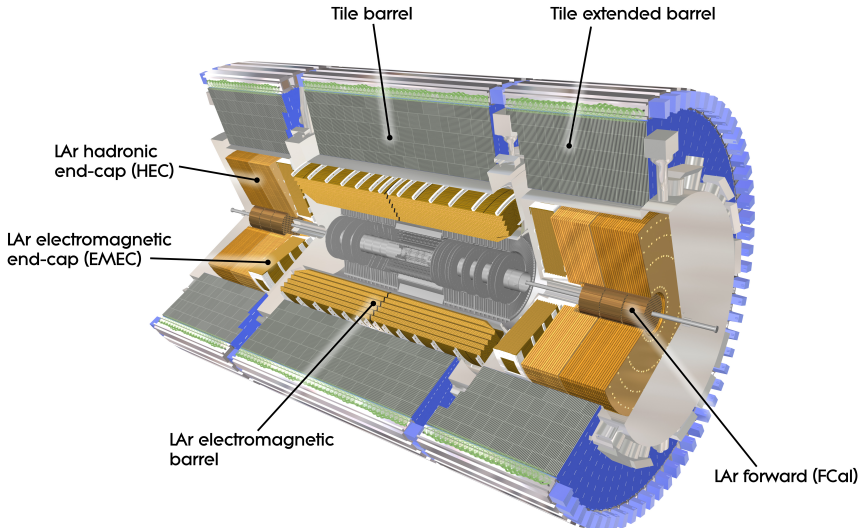


Figure 2.7: Cutaway representation of the ATLAS calorimeter system and its main components [73].

2.2.3.1 LAr electromagnetic calorimeter

The electromagnetic calorimeter (EM calorimeter) in the ATLAS detector is designed to precisely measure the energy of electrons and photons. It is based on a sampling technology that uses liquid argon (LAr) as the active medium and different metals (either tungsten, copper or lead) as the absorber material. This choice combines a high level of granularity with excellent linearity and radiation hardness, crucial for operation in the high-luminosity environment of the LHC.

The EM calorimeter is divided into three main regions: a barrel section covering the pseudorapidity range $|\eta| < 1.475$ (EMB), and two end-cap sections (EMEC) that extend the coverage up to $|\eta| = 3.2$. Each region is segmented longitudinally into three layers (plus a presampler), as can be seen in Figure 2.8, optimizing the reconstruction of electromagnetic showers. The presampler layer is used to correct for energy loss in the material upstream of the calorimeter. The first layer features fine granularity in the η direction ($\Delta\eta = 0.0031$), allowing for precise discrimination between single photons and the two close-by photons resulting from π^0 decays. The second layer collects most of the energy from electromagnetic showers and provides the primary energy measurement. The third layer corrects for energy leakage at high energies.

The LAr calorimeter employs an accordion-shaped geometry in both the barrel and end-cap regions. This design ensures full azimuthal coverage without projective cracks, while maintaining uniform response and mechanical stability. The calorimeter modules are housed in cryostats filled with liquid argon, operating at a temperature of approximately 87 K. The readout cells are segmented into towers of size $\Delta\eta \times \Delta\phi = 0.025 \times 0.025$ in the second layer, which defines the granularity for standard electromagnetic object reconstruction.

The signal is induced by the ionization of the LAr by charged particles in the shower. Ionization electrons drift under a high-voltage electric field, and the resulting current is read out with high precision using fast, low-noise electronics, used to determine the energy deposited by the original particle that hit the detector. The typical energy resolution of the EM calorimeter is described by the expression:

$$\frac{\sigma_E}{E} = \frac{a}{\sqrt{E}} \oplus b \oplus \frac{c}{E}, \quad (2.7)$$

where a represents the stochastic term (about 10%), b the constant term (below 0.7%), and c the noise term. The excellent resolution is essential for precision measurements such as the $H \rightarrow \gamma\gamma$ and $H \rightarrow ZZ^* \rightarrow 4\ell$ channels.

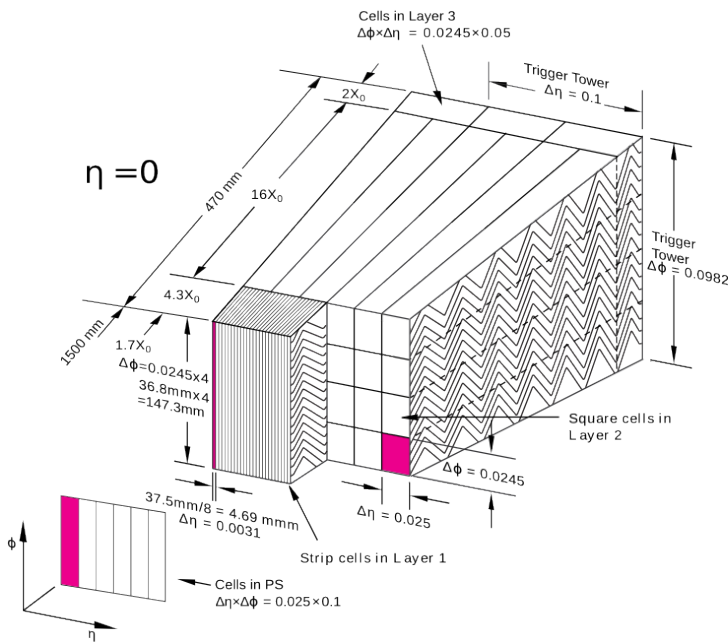


Figure 2.8: Schematic diagram of the cross-section of the LAr EM barrel calorimeter, including the presampler. The different granularity in η and ϕ of the cells of each of the three layers is also shown [79]

2.2.3.2 LAr hadronic calorimeters

The hadronic calorimeter system complements the electromagnetic calorimeter by measuring the energy of hadrons. In the end-cap and forward regions, the hadronic calorimetry is provided by these LAr-based detectors: the Hadronic End-Cap Calorimeter (HEC) and the Forward Calorimeter (FCal). These systems are critical for reconstructing jets, missing transverse energy, and for identifying hadronically decaying τ -leptons in the forward regions.

The HEC is positioned directly behind the EMEC and covers the pseudo-rapidity range $1.5 < |\eta| < 3.2$. It consists of copper plates as absorbers and uses liquid argon as the active medium. The copper-LAr combination ensures a compact structure with good radiation hardness and linearity. The HEC is segmented longitudinally into four layers and provides a depth of about 10 interaction lengths (λ_0) when combined with the electromagnetic calorimeter, enabling efficient hadronic shower containment. Each end-cap consists of two wheels: a front wheel (HEC1) constituted of 24 copper plates, and a rear wheel (HEC2) made of 16 copper plates.

The Forward Calorimeter (FCal) extends the coverage to $|\eta| < 4.9$ and is composed of three longitudinal modules: the first is electromagnetic, featuring copper absorbers, and the second and third are hadronic, and uses tungsten absorbers in order to reduce the lateral spread of the hadronic showers. The high-density design of the FCal is necessary to withstand the high particle flux and radiation levels encountered in the forward region. Due to its crucial role in reconstructing the forward energy flow, the FCal is also essential for pile-up suppression and missing transverse energy reconstruction.

Both HEC and FCal calorimeters operate within the same LAr cryostats as the electromagnetic sections, benefitting from the same stability and fast response.

2.2.3.3 Tile hadronic calorimeter

The Tile Calorimeter (TileCal) is ATLAS's main hadronic calorimeter, constructed as a sampling calorimeter composed of alternating layers of plastic scintillator tiles (active material) and low-carbon steel absorber plates. Positioned around the LAr calorimeter, TileCal provides coverage in the pseudorapidity region $|\eta| < 1.7$ and ensures containment of hadronic showers, limiting punch-through to the muon system with a total thickness of approximately 11 λ_0 at $\eta = 0$.

TileCal consists of a central long barrel (LB) section ($|\eta| < 1.0$, length of 5.8 m) and two extended barrel (EB) sections (EBA and EBC), each covering $0.8 < |\eta| < 1.7$ with a length of 2.6 m. Together with other calorimeters

(HEC, FCal), TileCal achieves coverage up to $|\eta| < 4.9$.

Each barrel segment is divided into 64 modules, featuring alternating 3 mm thick scintillator tiles and 14 mm thick steel absorbers along the beam axis. The scintillator tiles, arranged radially in 11 rows, generate scintillation light upon particle interaction. Wavelength-shifting (WLS) fibers collect and shift this light to longer wavelengths, guiding it to photomultiplier tubes (PMTs) at the module's outer radius, enabling efficient and hermetic readout.

The calorimeter modules are segmented into three longitudinal layers: layers A, BC, and D in the LB (1.5, 4.1, and $1.8 \lambda_0$, respectively) and layers A, B, and D in the EB (1.5, 2.6, and $3.3 \lambda_0$, respectively). Cells in these layers have granularity of $\Delta\eta \times \Delta\phi = 0.1 \times 0.1$ for inner layers and 0.2×0.1 for outer layers.

Additionally, gap scintillator cells (E1-E4) were installed between TileCal and LAr to correct for energy losses and enhance performance. The Minimum-Bias Trigger Scintillators (MBTs), also read out by TileCal electronics, provide coverage in $2.08 < |\eta| < 3.86$ for triggering purposes. Overall, TileCal incorporates 9852 readout channels, covering 5182 cells.

Figure 2.9 shows an schematic view of the readout geometry of all the calorimeter systems in the $r-z$ space, showing the different η ranges covered by them.

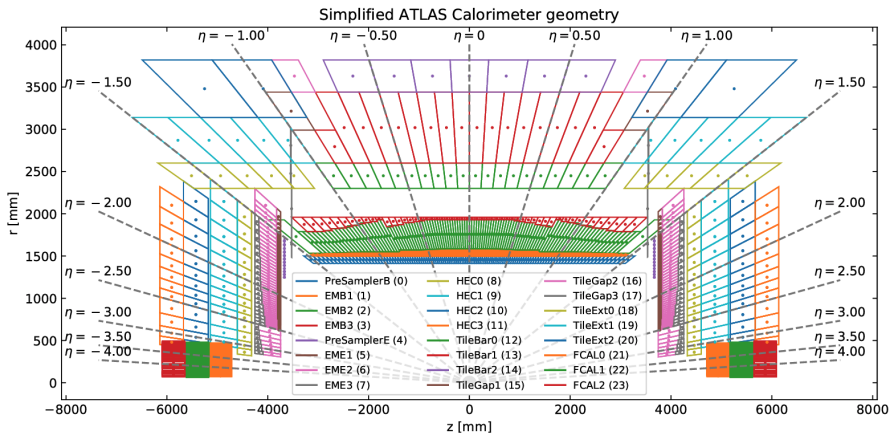


Figure 2.9: Visualization of the ATLAS calorimeter readout geometry. The three subsystems, Tile, Liquid Argon and the Forward calorimeters, are shown [80].

Additional upgrades have also been implemented in the ATLAS calorimeter electronics to meet Run-3 conditions and to prepare for the forthcoming HL-LHC era, mirroring the improvements made to the Inner Detector and ensuring

compatibility with the new trigger architecture. Both the Liquid-Argon and Tile Calorimeters have refurbished their on-detector and off-detector read-out chains; in TileCal specifically, new scintillating cryostat counters and renewed Minimum-Bias Trigger Scintillators have been installed for Run 3, enhancing electron-energy resolution and improving luminosity monitoring.

2.2.4 Muon spectrometer

Figure 2.10 shows the outermost subsystem of ATLAS, known as the Muon Spectrometer (MS) [81]. The MS is responsible for identifying muons, particles capable of traversing the calorimetric system with minimal energy loss. It comprises precision tracking chambers and fast-response trigger detectors embedded in a magnetic field of approximately 0.5 T in the barrel and 1.0 T in the end-cap regions, bending the trajectories of muons and enabling precise momentum measurement.

The MS includes four detector technologies totaling over one million read-out channels. A schematic view of the subsystem is shown in Figure ??, without including the New Small Wheel sector yet, implemented for Run 3. Two separate detector systems facilitate initial trigger decisions. Resistive Plate Chambers (RPCs) are used in the barrel region ($|\eta| < 1.05$), providing measurements with a resolution of about 10 mm in both longitudinal and transverse directions. In the end-cap region ($1.05 < |\eta| < 2.4$), Thin Gap Chambers (TGCs) handle higher background rates with wire separation of 1.8 mm and positional resolution around 5 mm. The RPC and TGC detectors primarily function as triggering components due to their fast response times.

Precision muon tracking relies mainly on Monitored Drift Tubes (MDTs), installed in both barrel and end-cap regions, covering the range $|\eta| < 2.7$ and offering high positional accuracy (approximately 35 μm per chamber). Cathode Strip Chambers (CSCs), multi-wire proportional chambers providing high rate capability and excellent time resolution (4 ns), are employed in the forward region ($2.0 < |\eta| < 2.7$). MDTs and CSCs are critical for accurately reconstructing muon trajectories.

For Run 3, the MS underwent significant upgrades, including the replacement of the forward muon-tracking region (known as the small wheel) with the New Small Wheel (NSW) [82]. The NSW consists of two large 100-tonne detectors located at each end of ATLAS, each 10 metres in diameter and segmented into 16 sectors. The NSW employs advanced detector technologies such as Micromegas (MM) and small-strip Thin Gap Chambers (sTGC), capable of simultaneous precision tracking and triggering. Each wheel contains two layers of MM and sTGC chambers, resulting in four measurement planes for improved tracking accuracy and more than 2 million readout channels. s

Moreover, despite being primarily designed to detect muons, the MS occasionally detects punch-through jets, hadronic jets that are not entirely absorbed by the calorimeters and reach the MS. The upgraded configuration of the MS, particularly with the addition of the NSW, significantly enhances ATLAS' capabilities in terms of tracking precision and trigger efficiency, essential for the high luminosity and challenging conditions expected during Run-3 and beyond.

Furthermore and aiming HL-LHC era, The Muon detectors will install new chambers in the barrel (RPCs and MDTs), replace the TGCs in the gap between the barrel and the end-caps and upgrade the readout electronics for the already installed RPCs, TGCs and MDTs to make them fully compatible with the trigger architecture.

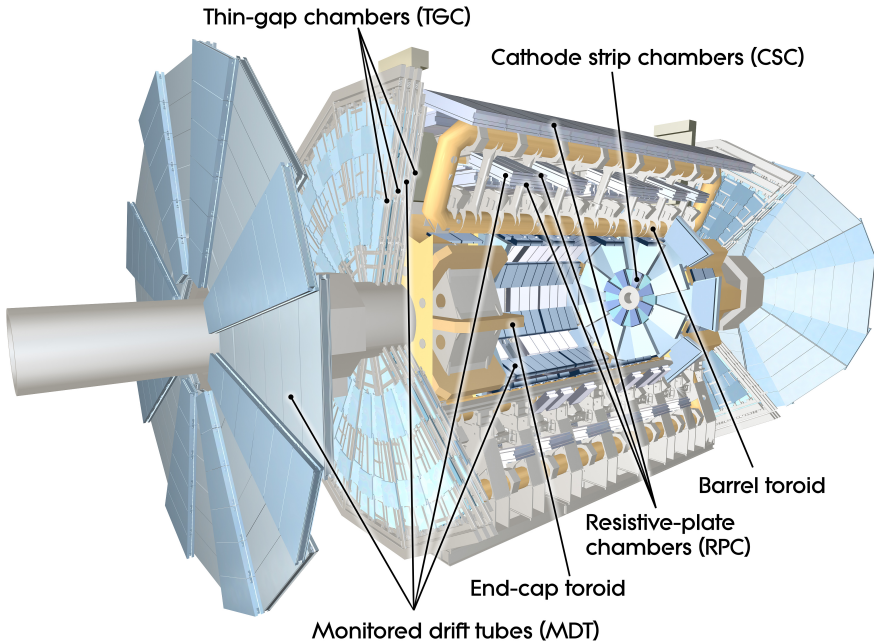


Figure 2.10: Cutaway representation of the ATLAS Muon Spectrometer [69].

2.2.5 Forward detectors

Beyond the main subsystems listed above, ATLAS employs four compact forward subsystems covering the remaining region of the detector ($|\eta| > 5$). LU-CID [83] (LUminosity Cherenkov Integrating Detector), situated ± 17 m from the interaction point, samples inelastic proton–proton interactions at very small angles and provides the experiment's primary online and offline relative-

luminosity measurement. LUCID is calibrated thanks to ALFA [84] (Absolute Luminosity For ATLAS), positioned inside Roman-pot stations ± 240 m from the IP, consists of scintillating-fibre tracking modules that can approach the beam to within ~ 1 mm, enabling precise absolute-luminosity determinations and studies of elastic scattering. The AFP [85] (ATLAS Forward Proton detector) was the last addition, located at 204 and 217 meters from the interaction point of both sides of the detector and aiming to extend the ATLAS physics reach by trying to tag very forward protons and enabling the observation of different processes where one of the two protons remains untouched. Finally, the Zero Degree Calorimeter (ZDC) [86], installed ± 140 m from the IP, is built from alternating tungsten plates and quartz rods. Covering $|\eta| > 8.3$, it detects neutral particles at zero degrees and is crucial for centrality measurements in heavy-ion collisions.

2.2.6 Trigger, Data Acquisition and Detector Control Systems

One of the most demanding challenges for an experiment such as ATLAS at the LHC is to devise an efficient strategy for handling the enormous volume of data recorded in the tiny interval that follows each proton–proton collision. During routine LHC operation, proton bunches cross every 25 ns, yielding a raw collision rate of 40 MHz. Since each interaction produces thousands of particles, together with their consequent showers, a single fully digitised ATLAS event occupies roughly 1.5 MB, which would translate into a data stream of about 60 TB s^{-1} . Practical bandwidth and storage constraints therefore make it impossible to archive every event, and, in any case, the majority are not relevant to the core physics goals of the experiment. To curb this flood while retaining the maximum amount of useful information, ATLAS employs a dedicated trigger system [87]. During Run 2 the trigger chain comprised two levels: a hardware-based Level-1 (L1) trigger, followed by a software-based High-Level Trigger (HLT). A schematic overview of the ATLAS Trigger and Data-Acquisition (TDAQ) system for Run 2 is shown in Figure 2.11.

The Level-1 trigger is a hardware-based system that cuts the raw 40 MHz collision rate down to about 100 kHz, operating with an exceptionally short latency of roughly 2.5 μs thanks to purpose-built custom and commercial electronics. The front-end electronics of every sub-detector store data in on-chip pipeline memories at the full 40 MHz bunch-crossing frequency. These buffers keep the digitised samples for 25 μs , that is the fixed window within which the L1 decision must be issued. That decision relies exclusively on information from the calorimeters and the muon spectrometer.

The L1 Calorimeter (L1Calo) trigger uses coarsened calorimeter read-outs

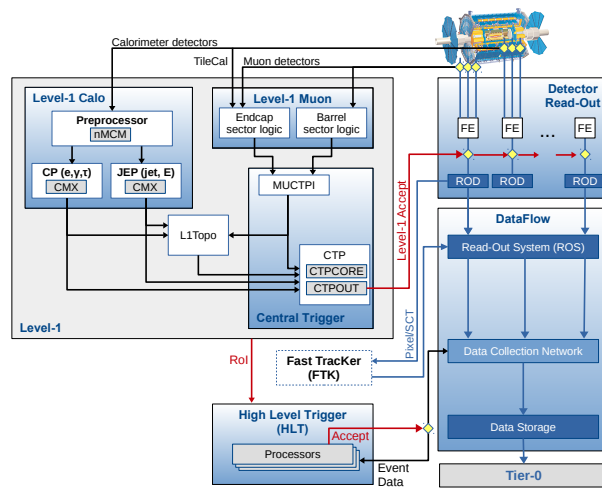


Figure 2.11: Schematic of the ATLAS Trigger and Data Acquisition system in Run 2 with specific focus given to the components of the L1 Trigger system [88].

(trigger towers) to locate regions of high energy deposition, i.e. regions of interest (RoIs). The L1 Muon (L1Muon) trigger exploits hits in the RPCs and TGCs to flag muon candidates, estimate their transverse momentum, and assign them to the correct bunch crossing. Outputs from L1Calo and L1Muon are merged in the Central Trigger Processor (CTP), which delivers the final verdict. If an event is accepted (an L1-Accept, or L1A), a signal is sent back to the front-end electronics so that the complete data corresponding to that bunch crossing can be read out from the pipeline memories. As noted above, the maximum L1A rate in ATLAS is 100 kHz.

The events accepted at Level-1 are first formatted by the sub-detector Read-Out Drivers (RODs) and then forwarded to the software-based High-Level Trigger (HLT). Running on a large computer farm, the HLT performs a rapid, partial reconstruction—tracking, charged-particle and jet identification (including b -jets), and a first estimate of the missing transverse momentum, throttling the event stream from 100 to roughly 1. Events that satisfy these online selections are written to permanent storage and transmitted to CERN’s Tier-0 centre for full offline reconstruction. While awaiting the HLT verdict, the corresponding data fragments remain buffered in the Read-Out System (ROS).

During Long Shutdown 2 (LS2, between Run 2 and Run 3) the Phase-I upgrade preserved the two-level architecture while introducing a suite of crucial improvements. A fully digital L1Calo trigger path now feeds three FPGA-based feature extractors: eFEX for electrons and photons, jFEX for jets and missing transverse energy, and gFEX for global event variables. It uses super-cell granularity as fine as $\Delta\eta \times \Delta\phi = 0.025 \times 0.025$. In the forward region ($1.3 < |\eta| < 2.4$) the newly installed New Small Wheels provide high-resolution muon trigger primitives, tightening transverse-momentum thresholds and cutting fake rates. The refurbished Level-1 Topological Processor exploits the finer calorimeter and muon inputs to impose angular, invariant-mass and transverse-mass selections in hardware. At the second stage, the HLT farm now runs on expanded computing resources, maintaining an output of roughly 3 kHz at an average event size of about 2.1 MB.

The Phase-II TDAQ upgrade, developed for the new conditions that will be delivered by HL-LHC, therefore foresees a two-stage hardware trigger in which an initial Level-0 decision accepts events at roughly 1, followed by a refined Level-1 selection that throttles the rate to about 400. Both stages will exploit full-granularity calorimeter read-outs together with prompt track information from the new ITk. The latency budget will be stretched to $\sim!10$, and a trigger-less streaming DAQ is foreseen, capable of digesting data throughputs in excess of 5. An enlarged processing farm, augmented with hardware accelerators such as FPGAs and GPUs, will then filter the stream down to a sustainable output

of 1015 for permanent storage. Collectively, these upgrades will preserve and probably extend the experiment’s physics reach in the demanding high-pile-up environment of the HL-LHC.

Detector Control Systems

A smooth dialogue between all ATLAS subsystems and the technical infrastructure that steers them is essential for reliable detector operation and data flow. This coordination is handled by the Detector Control System (DCS) [89], which provides a unified interface for operators and continuously monitors voltages, temperatures, gas flows, and countless other parameters. Whenever an abnormal condition is detected, the DCS automatically issues alarms, attempts corrective actions where possible, and guides shifters through any manual interventions required. In addition, the DCS exchanges status flags with the DAQ so that data taking proceeds only when all components are in a safe, ready state, and it brokers communication among subsystems that are controlled independently.

The LHC computer grid

To explain how the events accepted by the trigger are eventually processed, one must introduce The Worldwide LHC Computing Grid (WLCG) [90], which is a global, tiered infrastructure that stores, distributes and processes the multi-petabyte data stream produced by the LHC experiments. Data first reach Tier-0 at CERN, where the raw 40 MHz detector output is buffered, reconstructed and replicated; CERN then distributes this primary dataset to thirteen Tier-1 centres on three continents for large-scale reprocessing and long-term archival. Roughly 170 Tier-2 sites (university and regional clusters) supply the bulk of CPU for user analyses and Monte-Carlo production, while countless local Tier-3 farms serve individual groups. Today the WLCG federates \sim 1.4 million CPU cores and \sim 1.5 EB of disk and tape across 42 countries, sustaining average data-transfer rates above 260 GB s^{-1} and executing in excess of two million grid jobs daily. This distributed model enables more than 12000 physicists to access ATLAS data quasi-real-time, making large-scale analysis feasible without centralised super-computing resources.

Chapter 3

Data and simulated samples

3.1 Proton-Proton event simulation

In the following section, the modeling of proton-proton collisions occurring at the LHC is presented, which comprises several stages [91]. Firstly, the cross-section for the hard scattering introduced previously in Section 1.2.1 is calculated, describing the interactions between the partons that compose the incoming protons. This is followed by parton showering, where gluon emissions and parton splitting are simulated. The next step involves hadronization, where resulting partons combine to form color-neutral hadrons, which subsequently decay along with other unstable particles. Additionally, the modeling of pile-up and underlying events, originating from multiple simultaneous proton interactions beyond the primary scattering within the same bunch crossing, is included. Finally, events undergo detector simulation, digitization, and the same reconstruction algorithms used for real data, ensuring a realistic representation of experimental conditions. Figure 3.1 illustrates the aforementioned steps involved in simulating a proton-proton collision.

Matrix element and parton showers

Given the large momentum transfer involved in the hard scattering processes at the LHC, the partonic cross-sections can be computed using perturbative QCD. In this framework, partons may radiate additional gluons and split into further partons, which in turn can emit yet more radiation both in the initial and final states. Computing the full cross-section therefore requires summing over all possible parton emissions, which can be expressed as the perturbative

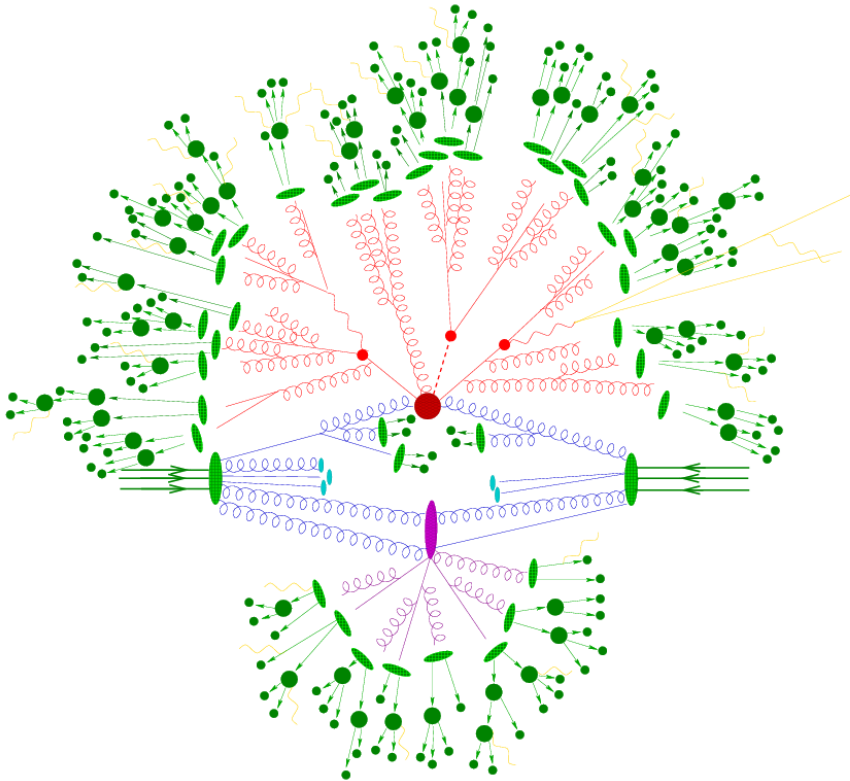


Figure 3.1: Representation of components relevant for simulating a proton-proton collision event containing all the factorised stages, excluding pile-up [92]. The central red blob represents the hard-scattering of incident protons, while in blue it shows the initial partons that contributed. Additional hard QCD radiation, outgoing partons and their decays are also represented in red. In light green ellipses it is represented the hadronization of final state partons, while the decay of the resulting hadrons is represented by dark green regions with arrows. The partons that did not participate in the primary interaction conform the underlying event, in purple. In yellow one can find the photon radiation, that can occur at any stage.

expansion:

$$\hat{\sigma}(ij \rightarrow X) = \sum_{n=0}^{\infty} \int d\Phi_{X+n} \sum_{k=0}^{\infty} |\mathcal{M}_{X+n}^{(k)}|^2, \quad (3.1)$$

being $\mathcal{M}_{X+n}^{(k)}$ the matrix element for the process $ij \rightarrow X + n$, with n the number of additional partons produced in the final state, k the number of included virtual loops, and $d\Phi_{X+n}$ the phase space element for this process. In the leading order calculation (LO), it only includes tree level matrix elements so it would correspond to $n = 0$ and $k = 0$. If it involves the production of N partons in the final state, then in this case the leading order calculation for the process $ij \rightarrow X + N$ will involve $n = N$ and $k = 0$. In the same way, a matrix element calculation with $k + n = m$ is referred to as a calculation at N^m LO, for $ij \rightarrow X$.

This is how the cross-sections are calculated precisely for such scattering processes. However, when too many partons appear in the final state the computation becomes prohibitively expensive, so the matrix elements are evaluated only up to a certain order in the strong coupling constant α_s , and the remainder is approximated via the parton-showering algorithm, where the showering is simulated using approximate matrix elements [93].

Matching and merging schemes prevent double counting between high-multiplicity matrix elements and the parton shower by assigning emissions above a chosen matching scale to fixed-order calculations and relegating softer or collinear radiation to the shower. Widely used approaches—such as the MLM algorithm [94] and CKKW schemes [95], with their NLO extension FxFx [96]—combine tree-level multileg samples of increasing jet multiplicity with parton showers to produce inclusive event samples that smoothly interpolate between hard, wide-angle emissions and soft, collinear radiation.

Hadronization

Below the perturbative cutoff of order 1 GeV, parton showering hands off to non-perturbative hadronization, during which coloured partons—each carrying definite momentum, flavour and colour—are clustered into colour-neutral hadrons. Phenomenological models such as the Lund string model or the cluster model take over here.

In the Lund string model [97] the colour field between a quark and an antiquark is treated as a relativistic string whose potential energy rises with separation; when that energy exceeds the mass of a new $q\bar{q}$ pair the string breaks, repeatedly creating additional pairs until all energy is exhausted, with hadron momenta drawn from an empirical fragmentation function. The cluster model [98] instead splits each final-state gluon into a $q\bar{q}$ pair and groups them

into colour-singlet clusters; those clusters then undergo a cascade of decays, or directly fragment, until only stable hadrons remain.

Pile-up and underlying event

All activity and interactions occurring in a proton–proton collision beyond the primary hard scattering must also be modelled; these are referred to as the underlying event and pile-up backgrounds, as discussed in Section 2.1. In the case of the underlying event, these soft interactions between partons are mainly described using phenomenological models, given their non-perturbative nature. When considering pile-up and non-collision backgrounds, one must simulate the additional proton–proton interactions that occur alongside the hard scattering, arising from nearby bunch crossings or even from protons interacting with beam-pipe or detector components. Backgrounds from the LHC cavern itself, such as proton–residual-gas collisions in the beam pipes, must also be modelled.

Each of these effects is generated separately and then overlaid onto the hard-scattering event before passing the combined event through the full detector simulation.

3.2 Detector response simulation

The raw collision data recorded by ATLAS arise solely from the interactions of final-state particles with the various subdetectors (see Section 2.2). To compare our Monte Carlo predictions with real data, we must therefore propagate each simulated event through a detailed detector model and reconstruct it identically to the collision data. This full detector simulation is performed with the GEANT4 toolkit [99], which tracks particles through the precise geometry of every ATLAS subsystem, simulates their electromagnetic and hadronic interactions, and converts energy deposits and tracks into digitized detector signals.

For maximum accuracy one employs the “Full Simulation” procedure in which GEANT4 processes the complete ATLAS geometry. However, calorimeter showers dominate the CPU cost, consuming nearly 90% of resources. To speed up large-scale productions, the ATLFAST-II fast-simulation simplified framework [100, 101] applies parametrized responses for both the inner detector and calorimeters, reducing computing time by an order of magnitude. Lastly, all simulations incorporate the actual detector conditions in force at the time of production: dead channels, electronic noise, alignment shifts, and calibration constants. Therefore the simulated events can always contain some

mismatch with the real data, since the conditions of the detector change constantly during the data taking.

3.3 Monte Carlo simulation generators

Monte Carlo generators are basically software tools that use pseudorandom numbers to reproduce predicted kinematic distributions and event dynamics according to a theoretical model such as the Standard Model. They fall into two broad classes: general-purpose generators, which reproduce the entire chain of event generation (hard scattering, parton showering, hadronization, etc.), and more specialized codes that excel at specific tasks, for example high-order matrix-element computations or detailed modeling of parton cascades.

To emulate the entire physics process of an event, several MC generators are commonly used. From a more generic approach to a more specialised one, we find PYTHIA [102], which is a general-purpose generator. This software uses LO matrix element calculations for $2 \rightarrow n$ events with up to three final-state partons, incorporating a p_T -order parton shower, based on the Lund model for hadronisation. Although this approach is capable of modelling the soft and hard interactions of the collision, its purely at LO cross-section is often not sufficient for high-precision analyses, so it must often be combined with other higher-order matrix element generators, and is used only as a parton shower generator.

Another generator with similar capabilities but which focuses on an angular-ordered parton shower is HERWIG [103]. It offers only $2 \rightarrow 2$ LO matrix element calculations and takes into account gluon splitting by incorporating all spin correlations, something that PYTHIA does not do. This software can simulate a wide range of processes with NLO accuracy for the matrix element calculation, but results in many events with negative weight which is problematic at certain stages of the physics analysis such as the one presented in this thesis. It is therefore also interfaced with other software that provides matrix element calculation at higher orders, while this one is used for hadronization, employing a cluster model.

SHERPA [104] is another MC generator which uses the CKKW matching procedure to move from Matrix element calculation, at LO and NLO, to parton showering modelling, operating for processes with multiple partons. It uses the cluster model for hadronization, and produces quite accurate simulations especially for processes with multiple jets or electroweak bosons. Si estamos interesados en more precise high-order matrix element calculations entonces el software más comunmente usado es MADGRAPH5_AMC@NLO [105]. Usa el MC@NLO method to interface with parton showers, using MLM and FxFx

matching models. Se suele usar en conjunción con PYTHIA o HERWIG.

Finally, among the most used models, the Powheg-Box [106] framework is also widely employed for high-order matrix element calculations, especially consistent for dealing with QCD corrections in both matrix elements and parton showers.

3.4 Data and MC simulated samples

All studies discussed in this thesis depend critically on comprehensive Monte Carlo simulations of both signal and background processes. These simulated samples provide the expected event yields and model the detector's response, incorporating the latest fixed-order theoretical cross-section calculations, state-of-the-art parton-distribution functions, and full event-generation chains including parton-shower evolution and hadronization. In the Higgs boson analyses presented here, the signal datasets reproduce the dominant production modes, while the background samples cover the Standard Model processes most likely to mimic those signatures.

For the electron-identification performance studies, dedicated simulations are used to model prompt electrons from $Z \rightarrow e^+e^-$ y $J/\Psi \rightarrow e^+e^-$ decays, as well as non-prompt electrons arising from other heavy-flavor decays or misidentified objects. The following sections describe the choice of generators and specific configuration settings employed to simulate each signal and background process in these analyses.

3.4.1 Simulation of electron samples

As mentioned, studies regarding electron identification presented in this thesis use MC simulation selecting electrons from $Z \rightarrow e^+e^-$ and $J/\Psi \rightarrow e^+e^-$ processes. Regarding background samples, we consider both two-to-two QCD processes and $t\bar{t}$ pair decays.

Both this signal and background events are processed through the full ATLAS detector simulation, based on GEANT4 as already mentioned. The Powheg-Box v1 matrix-element generator provides the hard-scattering simulation at NLO accuracy for Z -boson production and decay in the electron channel. Parton showering, hadronisation and underlying-event modelling are handled by PYTHIA 8.186, employing the AZNLO tune. The CT10NLO PDF set is used for the hard scattering, while CTEQ6L1 is adopted for the showering. Final-state-radiation effects are incorporated with PHOTOS++ 3.52 [107, 108]. Bottom- and charm-hadron decays are simulated with EVTGEN1.2.0 [109].

Prompt $J/\psi \rightarrow e^+e^-$ samples are generated with PYTHIA 8.186 using the A14 tune [110] together with the CTEQ6L1 PDF set.

Additional background $2 \rightarrow 2$ QCD processes that mimic the prompt-electron signature are modelled with PYTHIA 8.186 (A14 tune) and the NNPDF2.3LO PDF set. These samples, named under JF17, include multijet production, $qg \rightarrow q\gamma$, $q\bar{q} \rightarrow g\gamma$, electroweak W and Z production, and top-quark processes, and include events which are filtered to include mostly background electrons that mimic the prompt signatures.

Top-quark pairs are modelled with POWHEG-Box v2 at NLO using the NNPDF3.0NLO PDF set, with $h_{\text{damp}} = 1.5 m_{\text{top}}$ ¹. Parton shower, hadronisation and underlying event are provided by PYTHIA 8.230 (A14 tune, NNPDF2.3LO PDFs), while heavy-flavour decays are handled by EVTGEN 1.6.0. At least one W boson from the $t\bar{t}$ decay chain is required to decay leptonically.

Multiple pp interactions in the same or neighbouring bunch crossings are simulated by overlaying each hard-scatter event with minimum-bias interactions produced with PYTHIA 8.186.

3.4.2 Higgs boson and backgrounds simulated samples

Simulation of Higgs boson samples

Apart from electron performance studies, the analysis that will be discussed in this thesis consider the main production modes of the Higgs boson in the LHC, already introduced in Section 1.4.2. These mechanisms consist of the gluon-gluon fusion, vector boson fusion, the associated production of the Higgs boson with a vector boson, and the associated production with a pair of top quarks together with single top quark associated production.

In the case of the leading production mode, ggF, the samples are produced at NNLO in QCD using POWHEG NNLOPS, and scaled to the cross-sections computed at $N^3\text{LO}$ in QCD [112–117], including NLO electroweak corrections [118, 119]. These samples are obtained using the PDF4LHC15NLO PDF set [120] together with the AZNLO tune for {pythia8 for the parton showering and hadronization.

The VBF production mode is sampled at NLO with POWHEG interfaced with PYTHIA 8. The AZNLO tune is also used here for the showering and hadronization and the PDF4LHC15NLO PDF set for the PDFs. Again, the predicted samples are scaled to the cross-section computed at an approximate

¹The h_{damp} parameter is a resummation damping factor that controls the matching of the matrix element calculation with the parton showering (and consequently the amount of high-pT radiation against the $t\bar{t}$ system recoil) [111]

NNLO in QCD [121], including EW corrections as well at NLO level [122]

The Higgs boson production in association with a vector boson is simulated at NLO with one additional parton using POWHEG interfaced with {pythia8}. Once again, AZNLO tune is used for the parton showering and hadronization, and the PDF4LHC15NLO PDF set is used for the PDFs. The gluon-induced production of the Higgs boson in association with a vector boson is generated at LO with the same setup. For the quark-induced production, a normalization to the NNLO computation in QCD is applied, including NLO electroweak corrections, and to the NLO computation in QCD for the gluon-induced production [123–129].

For the $t\bar{t}H$ production mode, core of this thesis, the POWHEG-BOX v2 generator at NLO in QCD [130–133] is used, configured with the NNPDF3.0NLO PDF set [12], interfaced with A14 tune of PYTHIA 8.230 for the parton shower modeling [110]. The simulation of bottom decay is generated using EVTGEN v1.6.0 [109]. In the case of the production associated to a single top quark, it is modeled at NLO using MADGRAPH5_AMC@NLO, interfaced with PYTHIA 8, with the CT10 PDF set and A14 tune. These samples are subsequently normalized to NLO in QCD computed cross-section.

In all these cases, in order to estimate the uncertainties due to the choice of the parton showering and underlying event modeling, an alternative sample is generated using HERWIG7 for the parton showering and hadronization, but keeping the matrix element calculation with POWHEG. Similarly, to estimate the uncertainties due to the choice of the generator for the matrix element calculation, an alternative sample is generated using MADGRAPH5_AMC@NLO interfaced with {pythia8}, and HERWIG7 [134] for the parton showering and hadronization. In Table 3.1 a summary of nominal MC generators employed for each process can be found.

As the last step, the branching ratios for the Higgs boson decays are computed using the HDECAY [135–137] and PROPHECY4F [138–140]. The full normalization of signal samples integrates the branching ratio of the Higgs boson decays to the pair of τ leptons considered in this analysis. In order to compute the calculate the cross-sections and branching ratios, the Higgs boson mass is set to 125.09 GeV.

Everything shown above mainly describes the simulations used for the first round of the Run-2 analysis presented in this thesis. In order to simulate the physics events produced during Run 3, and also covering the second production round of Run-2 simulations (known as R.22 Run-2), the combinations of MC generators, PDF sets and tunes generally remain the same as those detailed in Table 3.1, except for some changes.

For this new simulation campaign POWHEG is still used together with

PYTHIA for the matrix-element calculation and parton-shower description, but with more up-to-date versions (v6 and later releases of PYTHIA 8), also for Higgs production in association with a single top quark, encompassing both ($tH + \bar{t}H$) and ($tWH + \bar{t}WH$). Regarding the tune sets for the PDFs, this new round employs A14 together with NNPDF2.3LO for all of them, whereas in the first Run-2 round CTEQ6L1 and AZNLO tunes were also used for hadronization and showering.

Simulation of background samples

The QCD V +jets background is modelled with SHERPA v2.2.1 at NLO for up to two extra partons, using the NNPDF3.0NNLO PDF set. Matrix elements with up to four additional partons are generated at LO via the COMIX [141] and OPENLOOPS [142–144] libraries, and merged with the parton shower using the MEPS@NLO scheme of SHERPA. The yields are normalized to NNLO cross-section predictions. Electroweak V +jets samples are produced with the same setup (Sherpa v2.2.1 + NNPDF3.0NNLO + MEPS@NLO).

$t\bar{t}$ events are generated at NLO with POWHEG v2 + NNPDF3.0NLO, interfaced to {pythia82.30 (A14 tune)}. The h_{damp} parameter is set to $1.5 m_t$ [145], and b - and c -hadron decays are handled by EVTGEN v1.6.0. To assess parton-shower uncertainties, an alternative sample uses the same hard process but with HERWIG 7.04. An alternative matrix-element uncertainty sample is produced with MADGRAPH5_AMC@NLO + NNPDF3.0nlo, showered with {pythia8 (A14 + NNPDF2.3lo)}.

Single-top s - and t -channel processes are generated at NLO in QCD with POWHEG v2 using NNPDF3.0NLO, in the five- and four-flavour schemes respectively, and parton showers modeled with {pythia8 2.30 (A14 + NNPDF2.3lo)}. Cross-sections are normalized to NLO predictions from HATHOR 2.1 [146].

Diboson (WW , WZ , ZZ) samples are simulated with SHERPA v2.2.1–2.2.2, with NLO matrix elements for up to one extra parton and LO for up to four. Gluon-induced $gg \rightarrow VV$ is included at LO (up to one extra parton). Merging is performed via MEPS@NLO, using the NNPDF3.0NNLO set, and virtual QCD corrections are provided by OPENLOOPS. All diboson samples are normalized to NLO cross-sections.

Now regarding what have been done to simulate these processes in the new round of the analysis, only the generator versions, merging multiplicities and normalizations have been updated: SHERPA for V +jets is now v2.2.14 with NLO up to two and LO up to five extra partons under an improved CKKW–MEPS@NLO merge; $t\bar{t}$ and single-top remain generated with POWHEG-Box v2 but are showered with PYTHIA8.308 (A14, NNPDF2.3,LO) and use

EVTGEN2.1.1, with normalization to the NNLO+NNLL cross-section from TOP++,2.0/PDF4LHC21; dibosons are produced with SHERPA 2.2.14 (NLO up to one, LO up to three extra partons, including $gg \rightarrow VV$ at LO) merged via CKKW-MEPS@NLO and normalized as before.

Table 3.1: Summary of the Monte Carlo generators employed for the primary signal and background samples. Normalization indicates the perturbative order used in the cross-section calculations for each sample.

Process	Generator		PDF set		Tune	Normalization
	ME	PS	ME	PS		
Higgs boson						
ggF	PowHEG-Box v2	PYTHIA 8	PDF4LHC15NNLO	CTEQQ6L1	AZNLO	N ³ LO QCD + NLO EW
VBF	POWHEG-BOX v2	PYTHIA 8	PDF4LHC15NNLO	CTEQQ6L1	AZNLO	NNLO QCD + NLO EW
WH	POWHEG-BOX v2	PYTHIA 8	PDF4LHC15NNLO	CTEQQ6L1	AZNLO	NNLO QCD + NLO EW
tH	PowHEG-Box v2	PYTHIA 8	NNPDF3.0NLO	NNPDF2.3LO	A14	NLO QCD + NLO EW
tH	MadGraph5_aMC@NLO	PYTHIA 8	CT10	NNPDF2.3LO	A14	NLO
bH	PowHEG-Box v2	PYTHIA 8	NNPDF3.0NNLO	NNPDF2.3LO	A14	NLO
Background						
V+jets	SHERPA v2.2.1	SHERPA	NNPDF3.0NNLO	NNPDF3.0NNLO	SHERPA	NNLO (QCD), LO (EW)
t	POWHEG-BOX v2	PYTHIA 8	NNPDF3.0NLO	NNPDF2.3LO	A14	NNLO + NNLL
Single top	POWHEG-BOX v2	PYTHIA 8	NNPDF3.0NLO	NNPDF2.3LO	A14	NLO
Diboson	SHERPA v2.2.1	SHERPA	NNPDF3.0NNLO	NNPDF3.0NNLO	SHERPA	NLO

Chapter 4

Physics objects reconstruction

Once the High-Level Trigger accepts an event, the recorded data are processed offline to reconstruct the particles emerging from the proton–proton collision. Signals in the ID, calorimeters and MS are combined by dedicated algorithms to form the physics objects used throughout this thesis: charged-particle tracks and collision vertices, muons, electrons and photons, jets, including heavy-flavor tagging, hadronically decaying τ -leptons, and missing transverse momentum. Figure 4.1 shows a schematic description of different fundamental particles interacting with the detector. To accommodate diverse analysis requirements, each reconstruction algorithm offers multiple working points (WPs), trading off identification efficiency against background rejection. This chapter describes the algorithms used to reconstruct the different physics objects, emphasizing those most relevant to the measurements described in this thesis.

4.1 Tracks, vertices and energy clusters

As mentioned before, tracks, vertices and calorimeter energy clusters, as well as matching requirements among themselves, are the essential inputs to the reconstruction and identification of physics objects which are going to be discussed in this chapter

The first step in the reconstruction of an event is the identification of the trajectories defined by charged particles in the ID, which are called tracks. Charged particles traversing the ID leave spatially precise hits in the Pixel and SCT layers. Under the solenoidal 2 T magnetic field, their paths bend

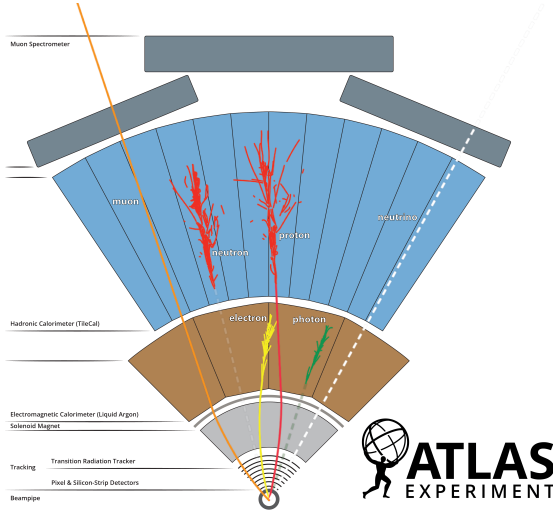


Figure 4.1: Schematic representation in the $x-y$ plane of fundamental particles interacting with the different ATLAS sub-systems [69]

into helices, with curvature inversely related to transverse momentum. Each reconstructed track is described by five parameters: transverse momentum p_T , polar angle θ , azimuth angle ϕ , the impact parameter in the transverse plane with respect to the interaction point d_0 , and longitudinal impact parameter, in the longitudinal plane z_0 . Figure 4.2 shows a representation of those parameters.

The reconstruction proceeds in several stages [147]. First, nearby hits or sensor measurements above a threshold are clustered and triplets of clusters form track seeds. Next, a combinatorial Kalman filter [148] extends each seed outward, adding compatible clusters layer by layer and updating the track parameters at each step (i.e. the momentum or its position). Multiple overlapping candidates are pruned by an ambiguity solver, which scores each track using fit χ^2 , p_T , the number of associated clusters, and the count of “holes” (expected but missing hits), to favor well-measured and high- p_T trajectories.

Finally, surviving candidates undergo a global fit, incorporating all valid clusters to refine the five helicoidal parameters. The chosen tracks are required to have at least 7 clusters between the Pixel and the SCT detectors, less than 2 holes in the Pixel and a maximum of 2 holes in the SCT sub-detector, a $p_T > 500$ MeV and a $|\eta| > 2.5$. In addition, the track is required to satisfy $|d_0| < 2$ mm and $|z_0 \sin \theta| < 3$ mm, and then it is reatined for downstream object reconstruction.

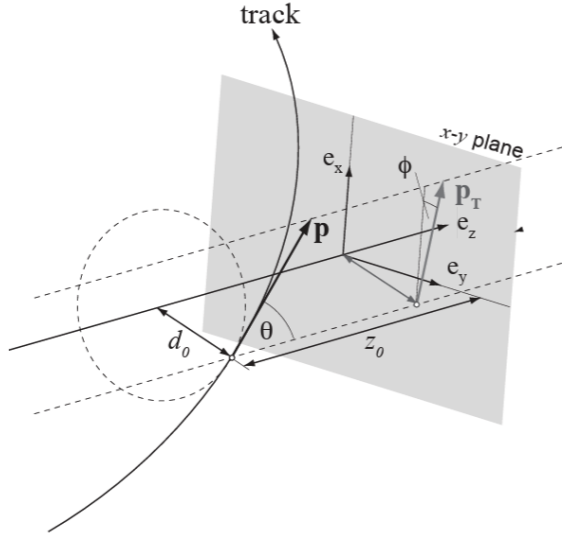


Figure 4.2: Schematic representation in the $x-y$ plane of fundamental particles interacting with the different ATLAS sub-systems [69]

Subsequently, the tracks are used to reconstruct vertices, which correspond to the locations where particle interactions occur. Vertices are identified by extrapolating tracks backward to their point of closest approach. We are primarily interested in those vertices occurring near the proton–proton interaction region. The primary vertex of an event is defined as the interaction point where the colliding protons met, while all other reconstructed vertices are treated as pile-up or secondary vertices, which are also crucial for b-tagging and identifying other displaced objects. For a detailed description of primary-vertex reconstruction in ATLAS see refs. [149–151].

Generally, vertex reconstruction proceeds in two phases: finding and fitting. First, vertex finding groups tracks into vertex candidates. An initial seed position is chosen, and then an iterative fit adjusts both the vertex position and individual track weights, which quantify how well a track originates from that vertex. Tracks whose weights fall below a threshold at the final iteration are excluded and reserved for forming additional vertices. This cycle repeats on the remaining unassigned tracks until no further vertices emerge. Next, vertex fitting refines the 3D location of each candidate using its assigned tracks. The event’s primary vertex is defined here as the one whose tracks have the largest $\sum p_T^2$, although alternative primary-vertex definitions exist.

The missing ingredient was the energy clusters. Particles leave energy deposits in individual cells of ATLAS calorimeters, which are clustered together forming 3D topological cell clusters, called topo-clusters [152].

Topo-clusters are constructed by first identifying seed cells whose measured signal exceeds the expected electronics noise by a significant amount. From each seed, adjacent cells are added iteratively whenever their signal-to-noise ratio passes a predefined threshold, and this expansion ceases once no further cells meet the criterion. Cells with low significance are excluded, naturally filtering out noise. Because hadronic showers spread more broadly than electromagnetic ones, a single topo-cluster may capture an entire shower, only part of it, or even combine energy deposits from multiple particles.

Since the ATLAS calorimeters are non-compensating, which means that their response to hadrons is lower than to electrons or photons of the same energy, all signals are initially recorded on the electromagnetic energy scale. To account for the differing responses and energy losses in inactive materials, topo-clusters undergo dedicated calibrations. After calibration, each cluster can be treated as a massless pseudo-particle, described uniquely by its calibrated energy and position in the $\eta - \phi$ space.

4.2 Muons

Muons are reconstructed and identified using combined information from the Inner Detector (ID) and the Muon Spectrometer (MS). These minimum-ionizing particles with long penetration length through the calorimeters leave very small energy deposits in the subdetectors.

Reconstruction

Track candidates are first found independently in the ID and in the MS. In the ID, the tracks are reconstructed exactly as explained in Section 4.1.

In the Muon System, track fragments are formed by combining hits that lie close together along the expected trajectory of a muon and that are consistent with having originated from the proton–proton collision interaction point (i.e., they point back to the IP) [153]. In order to create seeds, segments from the middle station of the MS are first used, and these seeds are then extended into the inner and outer detector layers. A track candidate requires at least two such segments, and a given segment may contribute to multiple candidates. Ambiguities are resolved and the candidate is accepted or rejected by performing a χ^2 -fit to the hits associated with each track candidate, together with additional track quality requirements.

Once we have both trajectories reconstructed in ID and MS, various muon reconstruction categories are defined based on the detector information they exploit. “Combined” muons result from a joint fit of Inner Detector and Muon

Spectrometer tracks, typically using an outside-in strategy that projects MS tracks back into the ID; an inside-out approach, seeding from the ID and extending into the MS, is also employed. “Extrapolated” muons rely uniquely on MS tracks extrapolated to the beamline, ensuring compatibility with the primary vertex, and extend coverage into the forward region $2.5|\eta|2.7$ beyond the ID acceptance. “Segment-tagged” muons begin with an ID track that is matched to at least one precision chamber segment in the MS, recovering muons that traverse only a single spectrometer layer. Finally, “calorimeter-tagged” muons are identified by isolated, minimum-ionizing energy deposits in the calorimeter aligned with an ID track, filling in gaps where MS coverage is incomplete.

Identification

On top of Reconstruction, the muon identification in ATLAS applies additional selection criteria to the reconstructed muons in order to reduce contribution from most likely background sources like charged hadron decays, in-flight decays... Seeking for a balance between identification efficiency and background rejection, different working points are defined encapsulating these selection requirements. The main ones are Loose, Medium and Tight working points, plus two additional ones devoted to low- p_T and high- p_T target muons.

The Loose WP accepts all reconstructed muon types (Combined, Inside–Out, Segment-Tagged, and Calorimeter-Tagged) with minimal kinematic cuts (e.g. $p_T > 4,\text{GeV}$), achieving maximal efficiency at the cost of higher fake rates, particularly in the reduced-coverage region $|\eta| < 0.1$. The Medium WP restricts to Combined and Inside–Out muons within $|\eta| < 2.47$, requires at least three precision-chamber hits spanning two muon-spectrometer layers (one layer suffices for $|\eta| < 0.1$), and imposes a compatibility cut on the charge-over-momentum difference between the Inner Detector and Muon Spectrometer measurements of less than seven standard deviations. Finally, the Tight WP further tightens these requirements by demanding a three-hit segment in two distinct spectrometer stations and stronger cuts on the q/p significance and inter-subdetector momentum consistency, all optimized in (p_T, η) bins to suppress residual backgrounds.

In simulated $t\bar{t}$ and $Z \rightarrow \mu\mu$ samples, the Medium WP achieves prompt-muon efficiencies up to 97% [153], while retaining background muons (e.g. from hadron decays) at the per-mille level. Discrepancies between data and simulation are corrected via η – ϕ –binned scale factors—typically within a few percent of unity—to account for local detector non-uniformities such as support-structure regions.

Isolation

Since prompt muons are typically produced well isolated from other activity, muon isolation is applied to reject non-prompt candidates. Here, isolation quantifies additional detector activity around the muon, while the decay of high-momentum objects, whose products are often collimated, including muons, can naturally appear isolated. Two isolation variables are used. Track-based isolation is defined as the scalar sum of the transverse momenta of all tracks with $p_T > 1$ GeV within a cone around the muon (excluding the muon itself), where the cone size shrinks with increasing muon momentum, p_T^μ , as $\Delta R = \min(0.3, 10\text{GeV}/p_T^\mu)$. Calorimeter-based isolation is computed by summing the energy deposits of topo-clusters within a fixed cone of $\Delta R = 0.3$ around the muon (again excluding the muon's own deposit) and applying pile-up corrections. Each isolation criterion is then expressed as a ratio of the isolation sum to the muon's transverse momentum. Several working points are defined: Loose, Gradient, and FCTight (“fixed-cut tight”) all use both track- and calorimeter-based isolation; FCTO (“fixed-cut track-only”) applies only the track-based requirement.

4.3 Jets and flavour tagging

As explained in Section 1.2.1, in the proton-proton collisions the quarks and gluons produced at the partonic level undergo hadronisation, resulted in collimated jets measured by the ATLAS detector via the tracks registered in the ID and energy deposits in the calorimeter system.

Jet reconstruction in ATLAS is fundamentally based on sequential recombination algorithms, the most widely used being the anti- κ_t algorithm [154]. This algorithm is designed to be stable in the presence of soft and collinear emissions from partons, operating by defining a distance measure between any two objects i and j (which may be tracks or topo-clusters) as follows:

$$d_{i,j} = \min(p_{T,i}^{2p}, p_{T,j}^{2p}) \frac{\Delta_{ij}^2, R^2}{,} \quad (4.1)$$

being $\Delta_{ij}^2 = (\eta_i - \eta_j)^2 + (\phi_i - \phi_j)^2$ the distance in the η - ϕ plane and R the radial parameter that defines the jet size. Setting the exponent p to 1 ensures that objects with higher transverse momenta dominate the clustering procedure. The beam distance is also computed for each object as:

$$d_{iB} = p_{T,i}^{2p}, \quad (4.2)$$

so the smaller of the two distance measures is chosen at each iteration. If d_{ij} is smaller, objects i and j are merged into a new object. If d_{iB} is smaller, then

object i is identified as a jet and removed from the list of objects to process, and the procedure continues until no objects remain. The parameter R sets the jet radius and the extent of the η - ϕ space used for clustering. It typically takes values of $R = 0.4$ for small-radius jets or $R = 1.0$ for large-radius ones [155].

Once jets are reconstructed, several energy calibrations are applied in order to correct detector effects y conseguir un matching accurate con la energía del jet at particle-level [156]. The first stage of jet calibration addresses pile-up effects arising from additional proton–proton interactions. An event-by-event correction is computed using the jet area and the transverse momentum density of the event, followed by residual corrections that depend on the number of reconstructed primary vertices and the average pile-up multiplicity.

Next, the Jet Energy Scale (JES) calibration adjusts each jet’s reconstructed energy and pseudorapidity so that, on average, it matches the true particle-level jet energy. This is achieved via p_T - and η -dependent scale factors derived from full detector simulation, accounting for the differing calorimetric response to electromagnetic versus hadronic showers. After JES, a Global Sequential Calibration (GSC) applies multiplicative corrections based on the jet’s internal properties, such as width, track–vertex association, and flavor-sensitive observables, in order to reduce residual biases between quark- and gluon-initiated jets and to compensate for variations in fragmentation.

An in-situ calibration then removes any remaining mismodeling by comparing the balance between jets and well-measured reference objects (like isolated photons) in data; these data-driven correction factors, supplemented by multijet balance methods, are applied only to data jets to align their response with simulation. The Jet Energy Resolution (JER) [157] is subsequently measured using dijet balance and random-cone techniques, yielding a p_T - and η -dependent resolution function. Simulation jets are smeared to reproduce the observed resolution in data.

Finally, to suppress pile-up jets, the Jet Vertex Tagger (JVT) [158] exploits track-based variables, particularly the fraction of jet tracks originating from the primary vertex, together with event-level pile-up information, to discriminate hard-scatter jets within $|\eta| < 2.4$. For the forward region ($2.4 < |\eta| << 4.5$), the forward JVT (fJVT) extends this technique, ensuring consistent pile-up rejection across the full calorimeter acceptance.

***b*-jets tagging**

Identifying jets originating from b -quarks (b -jets) is vital for many LHC analyses, especially those involving top quarks or Higgs bosons. b -hadrons travel a few millimeters before decaying, creating displaced secondary (and sometimes

tertiary) vertices and tracks with large impact parameters relative to the primary collision point. Simple b -taggers, like IP2D and IP3D, exploit these features by measuring the significance of transverse and longitudinal impact parameters and creating discriminants that recognizes tracks associated to non-primary vertex [159, 160], while secondary-vertex algorithms reconstruct displaced vertices and use features like invariant mass of tracks associated to the secondary vertex, vertex flight distance, and track multiplicity to distinguish b -jets from light-flavor or gluon jets.

Modern high-level b -taggers combine these low-level discriminants via machine-learning techniques in order to improve the overall performance, also being able to tag intermediate c -hadrons and involved tertiary vertices. The DL1r algorithm, used for the first round of Run-2 data [161], for example, feeds IP2D, IP3D, and secondary-vertex outputs into a deep neural network, along with additional variables, such as those from a jet-vertex finder, for improved c -jet rejection and an RNN to capture track correlations. DL1r produces three scores, corresponding to the probabilities that a jet originates from a b -, c -, or light quark, achieving superior separation compared to individual taggers.

The performance of b -tagging algorithms is characterized by the efficiency to identify b -jets and the rejection factors achieved against c -jets and light-flavor jets. Standard working points are defined at approximately 60%, 70%, 77%, and 85% b -jet efficiency, trading off signal efficiency against background suppression. To correct for residual differences between simulation and data, per-jet scale factors are measured in control regions with well-known flavor content (e.g. $t\bar{t}$ events) and applied to all Monte Carlo samples so that the simulated tagging efficiencies reproduce those observed in collision data.

For Run-3 and R.22 Run-2 data processings, the ATLAS b -tagging algorithm has evolved from the DL1r-based DNN to the enhanced GN2 network [162], which integrates Graph Neural Network techniques to better capture the relational information among tracks and secondary vertices. GN2 demonstrates improved separation power between b , c , and light-flavour jets, particularly at high pile-up, yielding a 10% gain in light-jet rejection at the 70% b -jet efficiency WP compared to DL1r.

4.4 Hadronic tau-leptons

Electrons and muons, usually referred to as light leptons, interact with the detector material and leave clear signatures. In contrast, τ -leptons, due to their greater mass, decay rapidly after approximately 1 μm , without reaching any detector layer. Therefore, they are typically reconstructed and identified from their decay products. τ -leptons can decay leptonically, to electrons or

muons plus neutrinos (manifesting as missing transverse energy, E_T^{miss}), so no specialized reconstruction is performed in those cases. In fact, a key feature distinguishing these leptons from prompt leptons produced directly in the hard scattering is that the τ -decay vertex is slightly displaced from the pp primary vertex, due to the finite lifetime of the τ , resulting in an impact-parameter distribution for the final-state leptons that differs from that of prompt leptons. On the other hand, for hadronically decaying τ -leptons ($\tau_{\text{had-vis}}$ from now on), which account for a total branching ratio of 65%, a dedicated reconstruction and identification procedure exists, since these decays yield jets composed primarily of charged and neutral pions [8].

The reconstruction of $\tau_{\text{had-vis}}$ candidates begins with jets as seeds, clustered using the anti- k_t algorithm with a radius parameter $R = 0.4$. Candidates are required to satisfy $p_T > 10 \text{ GeV}$ and $|\eta| < 2.5$. The τ -lepton energy is initially estimated by summing the energies of topo-clusters within a cone of $\Delta R = 0.2$ around the seed jet axis. Within the same cone, the transverse momenta of all associated tracks are summed to reconstruct the τ -decay vertex. The vertex with the highest summed p_T is chosen, and only tracks with $p_T > 1 \text{ GeV}$, at least two pixel hits, and at least seven hits in the SCT and TRT are retained. Impact-parameter requirements relative to the τ -vertex are $|d_0| < 1.0 \text{ mm}$ and $|z_0 \sin \theta| < 1.5 \text{ mm}$. The n -prong $\tau_{\text{had-vis}}$ decay can consist of n charged hadrons (mostly pions, occasionally kaons), so candidates are categorized as 1-prong or 3-prong. In the first Run-2 production, a dedicated Boosted Decision Tree (BDT) was trained to classify these track patterns; for the R.22 Run-2 and Run-3 samples, this was replaced by a Recurrent Neural Network (RNN) for τ -track classification [163].

After reconstructing the $\tau_{\text{had-vis}}$ candidate, distinguishing it from quark- and gluon-initiated jets that can mimic its signature is achieved using separate RNNs for 1-prong and 3-prong $\tau_{\text{had-vis}}$ decays. These networks are trained to be robust across the full p_T spectrum of the $\tau_{\text{had-vis}}$ and under varying pile-up conditions, exploiting features of the τ -lepton—namely its weak decay, which produces narrower jets with lower track multiplicities than QCD jets. The RNN output defines four working points (Tight, Medium, Loose, VeryLoose), with 1-prong efficiencies of 60%, 75%, 85% and 95%, and 3-prong efficiencies of 45%, 60%, 75% and 95%, respectively, balancing signal retention against background rejection. For the R.22 Run-2 and Run-3 samples, this RNN has been superseded by a Graph Neural Network (similar to that used for b -tagging [162]), yielding significantly improved fake- $\tau_{\text{had-vis}}$ rejection and reducing this background by up to 40% in our analysis.

Finally, during the first Run-2 production, an additional BDT, known as the electron-veto BDT (eBDT), was trained to reject background from electrons that can mimic 1-prong $\tau_{\text{had-vis}}$ decays. The eBDT uses high-level in-

puts such as calorimeter cell deposits and track features, with TRT information playing a crucial role in distinguishing electrons from hadrons. It achieved over 95% efficiency for genuine $\tau_{\text{had-vis}}$. For the R.22 Run-2 and Run-3 datasets, this task is now performed by a dedicated RNN [163].

4.5 Missing transverse momentum

Energy-momentum conservation guarantees that the total four-momentum of the initial state equals that of the final state. In pp collisions, the longitudinal momentum cannot be determined because the colliding partons carry unknown fractions of the proton momentum. However, since the incident protons travel and collide along the longitudinal axis, the total momentum in the transverse plane must be zero.

Thus, the missing transverse momentum (E_T^{miss}) quantifies the transverse energy carried away by invisible particles in the collision, as seen by the ATLAS detector. These invisible particles may be neutrinos or other weakly interacting species such as dark matter candidates. It is computed as the negative vector sum of all reconstructed and calibrated objects in ATLAS:

$$E_T^{\text{miss}} = - \underbrace{\sum_{\text{electrons}} p_T^e + \sum_{\text{muons}} p_T^\mu + \sum_{\text{photons}} p_T^\gamma + \sum_{\text{taus}} p_T^\tau + \sum_{\text{jets}} p_T^j}_{\text{hard term}} - \underbrace{\sum_{\text{unused tracks}} p_T^{\text{tracks}}}_{\text{soft term}}, \quad (4.3)$$

The missing transverse momentum has two contributions: the hard term, made up of calibrated electrons, photons, hadronically decaying τ -leptons, jets, and muons, and the soft term, which comprises energy not clustered into these objects. In ATLAS, the soft term is typically formed from tracks associated with the primary vertex, making it less sensitive to pile-up.

In simulations, the performance of E_T^{miss} is validated by comparing MC and data in processes such as $Z \rightarrow \mu^+ \mu^- + \text{jets}$, where the true E_T^{miss} is near zero. Discrepancies can expose detector effects, jet miscalibration, or residual pile-up.

Chapter 5

Statistical methods

Statistical techniques play a central role in high-energy physics, as they provide the tools needed to interpret, quantify, and extract meaningful information from the experimental results obtained at the LHC. This chapter outlines the different statistical methods employed throughout this thesis. A frequentist approach is adopted, in which the concept of probability refers to the relative frequency of an outcome in a repeatable experiment.

First, the statistical modelling of experimental data is introduced, including the construction of the likelihood function for binned data and the treatment of systematic uncertainties through nuisance parameters. This modelling stage provides the essential ingredients subsequently used for the statistical inference, which allow us to extract physics results from the data, including parameter estimation and hypothesis testing. The framework used for building and implementing these statistical models is `TRExFITTER` [164], which relies on the `HISTFACTORY` [165] format and the `ROOFIT` [166] and `ROOSTATS` [167] environments for model definition and statistical interpretation.

Finally, the use of multivariate techniques is discussed to perform classification and improve signal-to-background separation. In particular, an introduction to supervised learning and the machine learning algorithms used in this work is provided, with a focus on deep neural networks (DNNs) and boosted decision trees (BDTs). The increasing relevance and application of such techniques in particle physics reflects their ability to model complex correlations between observables, offering substantial improvements in classification and analysis optimisation tasks.

5.1 Statistical Modelling

5.2 Statistical Inference

5.3 Machine Learning Techniques

This section provides a general overview of the two most relevant algorithms used and developed throughout this thesis: DNNs and BDTs. Usually encompassed under the term multivariate techniques, these are machine learning algorithms that offer excellent performance in the tasks to which they have been applied. Most of concepts here presented are taken from reference [168]

In general terms, a machine learning algorithm can be defined as one that is capable of learning to perform a specific task based on input data, which typically consists of a multidimensional set of features. This thesis focuses specifically on supervised machine learning algorithms, which are trained using a set of n input data elements, $X = \{\vec{x}_0, \vec{x}_1, \dots, \vec{x}_n\}$, where each element encapsulates m features, as previously mentioned, $\vec{x}_i = (x_{i,0}, x_{i,1}, \dots, x_{i,m})$. The term "supervised" is used because each data point is associated with a known true label y_i , and the goal is to infer this label for new, unseen data using the input provided during training.

Datasets preparation

When training a supervised machine learning model, the so-called training dataset is used to optimize the model parameters. However, in order to properly evaluate the model's performance and select its best version, one must rely on data that has not been seen during the training process. If the same training dataset were used for evaluation, the model could learn overly specific features or fluctuations from this subset that are not present in real experimental data. This would ultimately lead to degraded performance when applied to unseen data. This issue is known as overtraining or overfitting.

To mitigate this problem and improve generalization, a validation dataset is used. The model's performance is monitored on this separate dataset during training in order to guide the optimization process and prevent overfitting. The version of the model that performs best on the validation data is typically chosen as the final one.

For a final, unbiased evaluation of the model's performance, a third dataset, called test dataset, is employed. Since both the training and validation datasets have already influenced the model, they cannot be used to assess its final quality. Typically, the three datasets (training, validation, and test) are obtained from the same original input sample by randomly splitting its data points.

Another widely used approach to maximize the use of available data is the

k-fold cross-validation technique [169]. In this method, the original dataset is split into k equal parts (or "folds"). The model is then trained k times, each time using $k-1$ folds for training and the remaining one for validation. This allows every data point to be used for both training and validation at different stages, providing a more robust performance estimate and making efficient use of limited datasets.

Type of prediction

A ML algorithm can be designed to perform various tasks, even multiple ones simultaneously. These include data synthesis and sampling, anomaly detection, and others. Many of these tasks are also employed in the context of high energy particle physics. In this thesis, we focus specifically on classification, the most fundamental task besides regression.

Classification problems generally involve that the learning algorithm is asked to determine which of k predefined categories a given input belongs to. Formally, this is often expressed as finding a function $f : \mathbb{R}^n \rightarrow \{1, \dots, k\}$, where a vector of input features \vec{x} is assigned a class label $y = f(\vec{x})$. In many practical implementations, especially in physics applications, the model does not directly return a class label, but instead provides a probability distribution over all possible classes. The final classification decision can then be made by selecting the class with the highest predicted probability.

If $k = 2$, the task is referred to as binary classification, and the model typically outputs a single value representing the probability that the input belongs to one of the two classes (e.g., signal vs background in our domain). The probability of the alternative class is simply $1 - f(\vec{x})$. If $k > 2$, the task is referred to as multinomial classification and in such cases, one probability is returned for each class and the outputs can be combined into a single discriminant using a likelihood ratio as prescribed by the Neyman-Pearson lemma [170]:

$$\frac{p_0}{\sum_{i=1}^k f_i p_i}, \quad (5.1)$$

where p_i is the predicted probability for class i and f_i is a configurable weight that adjusts the importance of each class in the denominator. By tuning the f_i , the classifier's sensitivity to specific backgrounds or categories can be adjusted to fit the needs of a particular analysis.

Loss function

To quantify the optimization of a supervised machine learning model during its training, it is necessary to measure how well it is performing. For this purpose,

a loss (or cost) function is defined, which is the function to be minimized during the training of the model. The loss function of a dataset is computed by evaluating the loss value on each data point and averaging over all points:

$$\mathcal{L}(\hat{\vec{y}}, \vec{y}) = \frac{1}{N} \sum_{i=1}^N \mathcal{L}(\hat{y}_i, y_i), \quad (5.2)$$

where the $\hat{\vec{y}}$ are the set of predictions made by our model, and \vec{y} are the corresponding true labels, N is the number of data points in our dataset. \mathcal{L} is our loss function, and the choice we make for it will depend on the problem we are dealing with, leading to more or less efficient solutions. When we talk about a regression problem, the simplest one, like a linear fit of a straight line, the Mean Absolute Error (MAE) is commonly used, $\mathcal{L}(\hat{y}, y) = |\hat{y} - y|$. For binary classification, the most commonly used loss function is the so-called binary cross-entropy, $\mathcal{L}(\hat{y}, y) = -y \log(\hat{y}) + (1-y) \log(1-\hat{y})$. Its generalization to the case of multinomial classification is obtained through the categorical cross-entropy, defined as:

$$\mathcal{L}(\hat{y}, y) = - \sum_c y_c \log(\hat{y}_c), \quad (5.3)$$

being c each of the classes considered in the problem.

Performance measurements

As mentioned earlier, the final performance of the trained model must be tested on a totally unseen test dataset. The loss function primarily serves to guide the optimization process during training, although a low final value often indicates the goodness of our model. Specific metrics or figures of merit, depending on the problem at hand, are usually employed to gain a deeper understanding of the efficiency of our ML models.

In the case of classification problems, as in our work, the most commonly used figure of merit is the Receiver Operating Characteristic (ROC) curve, which provides a clear visualisation of the performance of a binary classifier in terms of signal and background identification efficiency, which is precisely the core issue we aim to address.

We aim to optimise both quantities, and to obtain the ROC curve we compute them for different values of the discriminant output of our algorithm. The signal identification efficiency is calculated as the number of candidates with a discriminant value above the threshold, divided by the total number of signal candidates. Instead of background efficiency, we typically use its inverse: the background rejection. Plotting background rejection against signal efficiency

allows us to identify the model that offers the best performance, as illustrated in the example in Figure 5.1. The optimal model will be the one that reaches values closest to the upper right corner.

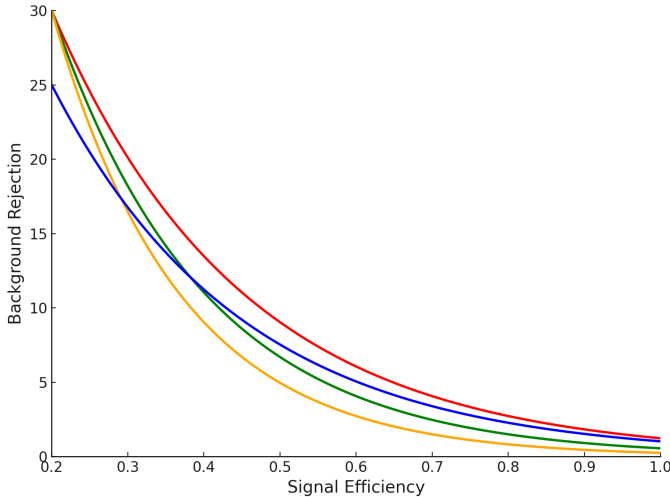


Figure 5.1: Example of ROC curves evaluated for different models in terms of signal efficiency and background rejection.

5.3.1 Deep Neural Networks

One of the most widely used and well-known ML algorithms are Neural Networks (NNs). There exists a broad variety of architectures, but the most basic ones are the Deep Neural Networks (DNNs), generally referring to any NN with multiple hidden layers. In this thesis, we implicitly refer to Feed-Forward DNNs, where information flows in one direction, from input to output, without any feedback or recurrence.

In general terms, the simplest form of a NN is a linear layer, which applies an affine transformation to the input data and can be described as:

$$\vec{x}_{out} = W\vec{x}_{in} + b, \quad (5.4)$$

where W is a weight matrix associated with each node, b is a bias vector, and $\vec{x}_{in,out}$ are the input and output feature vectors. Both the weights and the biases are parameters learned and optimized by the NN during training.

In the end, to build a DNN, depending on the complexity of the problem, the architecture is constructed by stacking multiple layers, which are applied sequentially, as illustrated in Figure 5.2.

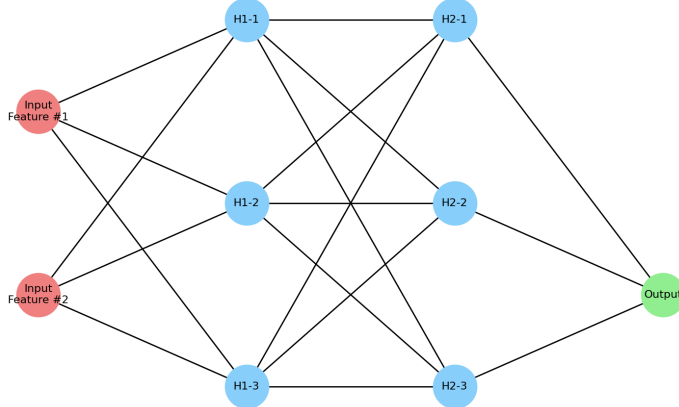


Figure 5.2: Diagram of Neural Network architecture with two input features, two hidden layers with three nodes each and one output.

It is important to note that the real dependencies and correlations among the input features are very likely to be non-linear and follow more complex patterns. However, since a single layer applies an affine transformation, the output will ultimately remain affine. To enable the algorithm to learn and handle non-linearities, activation functions are used.

5.3.1.1 Activation functions

Non-linearity is achieved by passing the output of a linear layer through an activation function. One of the most commonly used activation functions is the Rectified Linear Unit (ReLU), which is simply defined as follows

$$f(x) = \begin{cases} x, & \text{if } x \geq 0 \\ 0 & \text{if } x < 0 \end{cases}. \quad (5.5)$$

This simple action of setting the unit for positive inputs and zeroing the function otherwise introduces a non-linearity, and its derivative is straightforward to compute, which is beneficial for optimization.

There are other options that, in certain cases, can improve the performance of the NN output, such as the Leaky Rectified Linear Unit (Leaky ReLU), which modifies the negative part to have a small slope [171], meaning that negative values are not discarded but scaled by a certain factor. Another example is the Gaussian Error Linear Unit (GELU) [172]. As an illustration, a representation of these activation functions and their derivatives is shown in Figure 5.3.

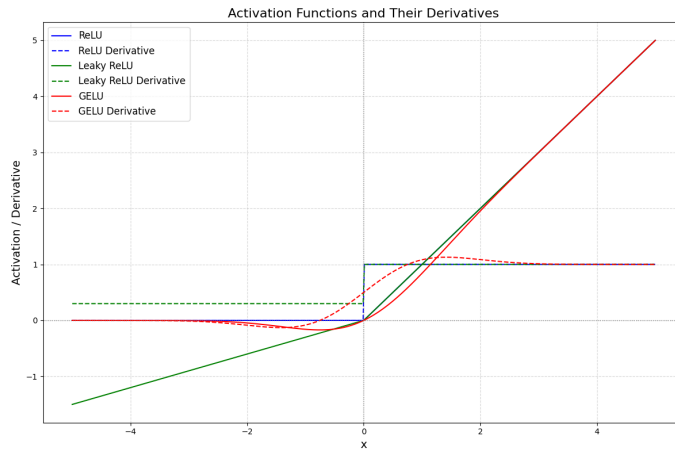


Figure 5.3: Some activation functions and their derivatives: ReLU (blue), leaky ReLU (green, slope of 0.3), GELU (red).

Another commonly used function is the sigmoid function, which is bounded between 0 and 1, given by

$$f(x) = \frac{1}{(1 + \exp(-x))}, \quad (5.6)$$

which is mainly used in the output layer of neural networks built for binary classification, so that the output can be directly interpreted as a probability. The generalisation of this function, called the softmax function, is used when the classification is multinomial and multiple outputs are present. It is defined as:

$$f(x_i) = \frac{\exp(x_i)}{\sum_j \exp(x_j)}, \quad (5.7)$$

ensuring that the sum of the outputs corresponding to all classes equals 1, and that individual outputs can also be interpreted as the probability of belonging to each class.

5.3.1.2 Regularization

Although regularisation techniques such as L2 regularisation, dropout, or normalisation layers are often employed to mitigate overfitting in neural networks, they are not explicitly used in the training strategy followed in this thesis. Nevertheless, the underlying principle remains the same: to increase the generalisation power of the model and avoid learning noise or fluctuations specific to the training dataset.

In this thesis, batch normalisation [173] is applied as the only regularisation-related technique. Batch normalisation acts by normalising the inputs of each layer to have zero mean and unit variance within a given batch of training data. This standardisation is done feature-wise, helping to stabilise and accelerate the training process. Moreover, it allows the use of higher learning rates and reduces sensitivity to initialisation. Unlike layer normalisation, which computes statistics over all features in a layer for each point separately, batch normalisation computes statistics across the entire batch, making it particularly effective in deep networks trained with mini-batches.

5.3.1.3 Optimization and Training

As previously discussed, the loss function guides the learning process of our neural networks. The optimisable parameters of our algorithm are updated using an optimiser. A wide range of optimisers exists, many of which are based on Stochastic Gradient Descent (SGD), which essentially computes the gradient of the loss function with respect to these parameters.

Aiming to minimise the loss function, the parameters are updated at each step in the negative gradient direction as follows (for a single parameter):

$$\theta_{i+1} = \theta_i - \eta \Delta_\theta \mathcal{L}_\theta(\hat{\vec{y}}, \vec{y}), \quad (5.8)$$

where θ_i is the learnable parameter at step i , and η is the learning rate (LR), which defines the step size. In this thesis, an extension of the SGD optimiser called *Adam* [174] is used.

Since analytical computation of the gradients is infeasible, the backpropagation algorithm [175] is employed. It efficiently computes these gradients by propagating the computation backwards from the output layer to the input.

Finally, it is during the training itself that the learnable parameters are optimised based on the input data. Information is passed to the algorithm in small subsets of data, called *batches*. The value of the loss function is computed on each batch and used to update the network's parameters, aiming to reduce the loss function as described.

This process is repeated for all the batches into which the original dataset has been divided, completing what is known as one *epoch*. After each epoch, the performance of the neural network is evaluated on the validation dataset. We repeat this for all the agreed number of epochs and finally retain the model that performs best in terms of validation loss.

Regarding the implementation of the architecture and its optimisation, there are many software libraries available for machine learning, with TensorFlow [176] and PyTorch [177] being among the most widely used. The neural

network model used in this thesis was implemented using TensorFlow version 2 (various minor releases). Since these frameworks are not natively compatible with the ATLAS software environment, the `lwttn` [178, 179] package was originally developed to facilitate the integration of neural networks into the ATLAS software.

5.3.1.4 Preprocessing

5.3.1.5 Input Data and Preprocessing

A common issue when directly feeding a DNN with the collected training input dataset is that the algorithm might learn specific features that are either irrelevant or not fully representative of what is expected in real data. This can lead to a degradation in performance. To mitigate such effects, a data preprocessing step is introduced before passing the input to the algorithm.

Applying scaling or certain transformations to the input data is generally beneficial in most cases. In general, DNNs tend to perform better when input features are of order one. This significantly improves the stability of the training process, its speed and efficiency, and ultimately the final performance of the algorithm.

A simple way to illustrate this is to consider a neural network with two inputs, $x_1 = 1$ and $x_2 = 100$. In the first hidden layer, each node combines these inputs as $w_1x_1 + w_2x_2$, where w_1 and w_2 are the weights. These typically start with similar values during optimisation, so due to the large difference in the input values, x_1 contributes very little to the DNN. The optimisation process may fail to balance both contributions effectively.

Transformations or scalings such as those implemented in the `scikit-learn` package [180] can address this issue. Among them are the `StandardScaler` and `RobustScaler`, which apply affine transformations to standardise the input features. In this thesis, however, only the `QuantileTransformer` is used. This method performs a monotonic, non-linear transformation that maps the input distribution of each variable to a uniform distribution between zero and one, based on empirical quantiles. This approach effectively handles outliers and compresses extreme values but may introduce distortions in the correlations between input variables.

It also happens that in some cases, certain input variables play a critical role in defining the phase space of the problem or guiding the algorithm's learning process, but they should not directly influence the classification decision. A clear example in this thesis involves the pseudorapidity (η) and transverse momentum (p_T) of electron candidates. The features of signal and background electrons vary significantly with respect to these two variables, which can cause

the model to favour certain regions of η or p_T , introducing an unwanted bias.

To prevent this, two main strategies are adopted. The first consists in the targeted removal of candidates from overrepresented regions of specific classes, ensuring a more balanced distribution in η and p_T . The second strategy applies reweighting factors to the distributions of the other input variables so that the η and p_T shapes match across all classes. These two methods can be combined to achieve better balancing.

Another frequent source of bias occurs when the training dataset is dominated by a particular class. In such cases, the model tends to assign higher classification scores to this class by default, even when the discriminating features are weak. This imbalance can significantly compromise performance, especially in multiclass classification. The same strategies described above can be extended to address this issue and ensure a more balanced training.

5.3.2 Boosted Decision Trees

Boosted Decision Trees (BDTs) [181] are among the most widely used machine learning algorithms in high energy physics. They are based on a structured set of decision trees that use the boosting technique to enhance classification performance. Instead of relying on a single decision tree, which tends to overfit and lacks generalisation, BDTs combine the output of many weak classifiers to form a more powerful model.

Each decision tree consists of a sequence of binary splits that partition the input phase space according to a given set of input variables. At each node of the tree, a discriminating variable and an optimal threshold are selected to best separate the events of two classes, for the case of binomial BDTs. The metric most commonly used to determine the optimal split is the *Gini*-index, defined as:

$$G = \sum_i p_i(1 - p_i), \quad (5.9)$$

where p_i represents the purity of class i in a given node. The Gini index quantifies the degree of mixing between different classes: lower values indicate purer nodes and thus more efficient separations. The tree continues splitting recursively until a predefined stopping criterion is met, such as a minimum number of events per node or a maximum depth. The result is a decision tree that divides the input space into regions classified as signal- or background-like.

However, a single tree has limited power and is prone to fluctuations in the training data. To improve the generalisation, the boosting technique is

applied. In this approach, multiple trees are trained sequentially, each focusing on the events that were misclassified by the previous ones. The so-called boosting process assigns higher weights to those events which are difficult to classify in subsequent trees. In this work, the XGBoost [182] algorithm is used, a widely adopted implementation of gradient boosting that is both efficient and flexible.

XGBoost introduces regularisation techniques and optimised algorithms for training large ensembles of trees. Its performance is controlled through several hyperparameters, such as the learning rate, maximum tree depth, or the number of trees. However, in analyses with limited statistics, like the one in this thesis, there is little gain from an extensive optimisation of these hyperparameters. In such situations, the training is more sensitive to statistical fluctuations than to the fine-tuning of the model configuration.

While the original formulation of BDTs is focused on binary classification, the present work employs the multiclass extension of the method [169]. In this case, the algorithm assigns to each input a set of scores corresponding to each of the target classes, and the final classification is obtained by selecting the class with the highest score. This approach enables a single training to distinguish between multiple physics processes simultaneously, offering a powerful tool for complex analyses.

Chapter 6

Electron Reconstruction, Identification and Efficiency Measurements

subcaption booktabs tabularx

Electrons play a crucial role in the ATLAS physics programme, appearing in key final states from precision electroweak measurements to Higgs boson studies and BSM searches. For this reason, accurate reconstruction, identification, calibration and isolation are critical to achieving the ATLAS experiment’s scientific goals in most analyses.

Although the basic workflow for assembling electron candidates mirrors the one already explained for other physics objects in Chapter 4, the performance demands on electrons are particularly stringent, from the precision with which tracks and energy clusters are reconstructed to achieving the best possible agreement between recorded data and the Monte Carlo simulations used in performance and analysis studies.

In the following chapter we delve into how electrons are treated, defined and calibrated in ATLAS, especially because part of the work in this thesis has focused on the study and refinement of a Deep Neural Network (DNN) for electron identification and classification against other objects that can mimic their signature. The architecture of this Machine Learning (ML) algorithm is going to be shown, as well as the electron features that are used as inputs, its performance, and how its output is handled.

This DNN is introduced as an improved method intended to replace the likelihood approach employed since the beginning of Run-2, which is also discussed here. Finally, we compare efficiency measurements for prompt electrons

obtained with both techniques and derive scale factors to correct any mismatches between performance in data and in MC simulation. These efficiencies are measured in data using tag-and-probe techniques on a pure and unbiased sample of electrons, typically drawn from well-known physics processes rich in prompt electrons such as the decay $Z \rightarrow e^+e^-$, shown in Figure 6.1.

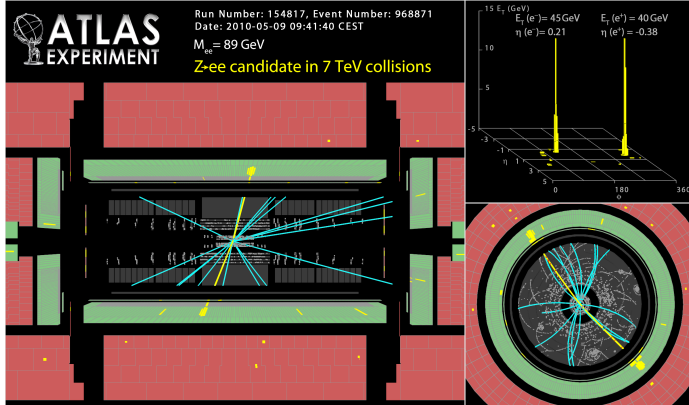


Figure 6.1: ATLAS reconstructed event display of a candidate for a $Z \rightarrow e^+e^-$ decay, collected on 9 May 2010. The two electrons are well isolated and represented with yellow lines. Further event properties: $p_T(e^+) = 40 \text{ GeV}$, $p_T(e^-) = 45 \text{ GeV}$, $\eta(e^+) = -0.38$, $\eta(e^-) = 0.21$, $m_{e^+e^-} = 89 \text{ GeV}$ [183].

The remainder of this chapter therefore covers: the reconstruction inputs and calibration steps that define ATLAS electrons; the architecture and training of the new DNN ID; the tag-and-probe procedures used to extract data-driven efficiencies; and finally, a direct comparison of DNN ID performance against the Run-2 likelihood benchmark. Together, these studies quantify the gains in signal efficiency and background rejection achieved by the neural-network approach and lay the groundwork for its deployment in Run-3 analyses.

6.1 Electron Reconstruction

In the ATLAS detector, an electron can be reconstructed when its electromagnetic energy deposits in the calorimeter system can be matched to a charged-particle track in the Inner Detector. Figure 6.2 illustrates the typical journey of an electron traversing the various layers of ATLAS, from the interaction point outward.

One can say that there are three stages in reconstructing an electron: although it first traverses the various pixel and silicon layers of the ID plus the

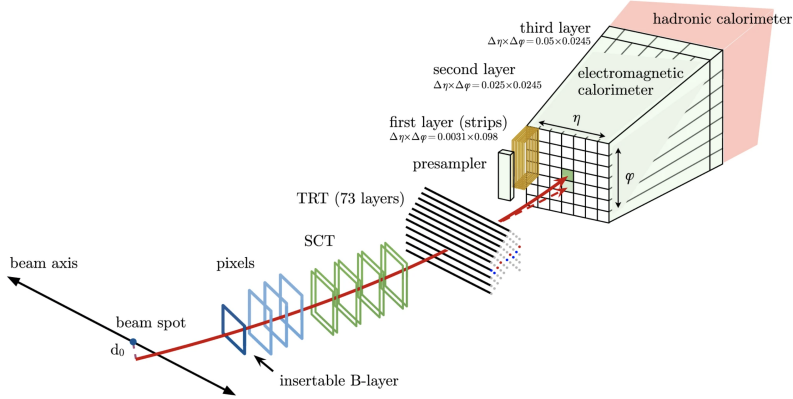


Figure 6.2: Schematic illustration of the typical journey of an electron passing through the ATLAS detector. In red it is represented its expected path, first going through the tracking system comprising the pixel and silicon-strip subdetectors, and finally the TRT. Afterwards it leaves mostly all its energy in the electromagnetic calorimeter. It can be also found the possible path (dashed red trajectory) of photon radiated by bremsstrahlung when the electron interacts with the material [184].

network of TRT straw tubes before depositing nearly all of its energy in the electromagnetic calorimeter through bremsstrahlung radiation and subsequent photon conversions into electron–positron pairs, the reconstruction of an electron candidate actually begins with the identification of clusters of calorimeter cells containing electromagnetic energy. After this clustering, the tracks in the Inner Detector are reconstructed and classified, as detailed in Section 4.1. The final step is to efficiently match these tracks to the electromagnetic clusters to form electron candidates, being able to distinguish them from other objects such as charged pions.

6.1.1 Cluster Building

Electron reconstruction begins with the formation of a collection of dynamically-sized clusters of cells from the electromagnetic and hadronic calorimeters. This dynamic algorithm for defining variable-size clusters was implemented in Run-2 [185], yielding performance that far surpasses the fixed-size algorithm used in the previous data-taking period [186].

These dynamically sized clusters, known as topological clusters (topoclusters), grow around a seed cell according to an algorithm detailed in Ref. [186]. A seed must satisfy a cell significance of $\epsilon_{\text{cell}}^{\text{EM}} \geq 4$ and cannot be located in the presampler or the first layer of the electromagnetic calorimeter. This

significance is defined as

$$\epsilon_{\text{cell}}^{\text{EM}} = \frac{E_{\text{cell}}^{\text{EM}}}{\sigma_{\text{noise},\text{cell}}^{\text{EM}}}, \quad (6.1)$$

being $E_{\text{cell}}^{\text{EM}}$ the energy of the given cell and $\sigma_{\text{noise},\text{cell}}^{\text{EM}}$ its expected noise.

The significance of all cells neighboring the seed cell is then evaluated, and any cell with $\epsilon_{\text{cell}}^{\text{EM}} \geq 2$ is added to the cluster. This procedure iterates, treating each newly added cell as the seed for the next step, forming a growing protocluster. Protoclusters sharing a cell are merged, and once no further high-significance cells can be included, a final growth step adds all adjacent cells regardless of their significance. If the resulting topocluster contains more than one local maximum, it is split into separate clusters, each centered on one maximum cell. A local maximum is defined as a cell with $E_{\text{cell}}^{\text{EM}} > 500$ MeV that has at least four neighbors of lower energy.

For electron reconstruction, only the energy deposited in the electromagnetic calorimeter is used, excluding any energy in the transition region $1.37 < |\eta| < 1.52$.

Contributions from the presampler and the first EM layer are also added when computing the cluster's electromagnetic energy. The electromagnetic fraction, f_{EM} , is defined as the ratio of this EM energy to the cluster's total energy. To suppress clusters from pile-up or hadronic activity, only those with $f_{\text{EM}} > 0.5$, $E_{\text{EM}} > 400$ MeV, and at least half of their energy in the ECAL are retained as electron candidates.

6.1.2 Track-to-Cluster Matching

For electron candidates, the standard tracking algorithm explained in Section 4.1 is extended to account for electrons losing energy via bremsstrahlung as they traverse the ID detector materials.

Initially, tracks are fitted under a pion hypothesis assuming an ideal helical trajectory [147]. If this fit fails for a given track seed within the region of interest defined by the EM topocluster (i.e., small pseudorapidity separation between track and cluster), the fit is retried with a modified pattern-recognition algorithm based on the Kalman filter formalism [187], which allows for energy losses at each material intersection due to photon radiation and thus deviations from a perfect helix.

This formalism, called Gaussian Sum Filter (GSF), represents the track state as a weighted sum of Gaussian components, each propagated in parallel via a Kalman filter, modelling the sudden curvature changes induced by discrete photon emissions. After GSF refitting, the tracks are extrapolated to the ECAL and matched to EM topoclusters using asymmetric ϕ windows

(wider on the side corresponding to expected energy loss) and tight η proximity. When multiple tracks match a single cluster, candidates are ranked first by fit quality and then by distance to the cluster barycentre in the second EM layer; the highest-ranked track is chosen to define the electron kinematics.

6.1.3 Superclusters and calibration

In order to capture the full energy deposited by bremsstrahlung photons from the electron candidate, adjacent EM topoclusters are merged into superclusters, which gather all significant energy deposits along the electron's radiative path, as represented in Figure 6.3. Reconstruction of an electron superclus-

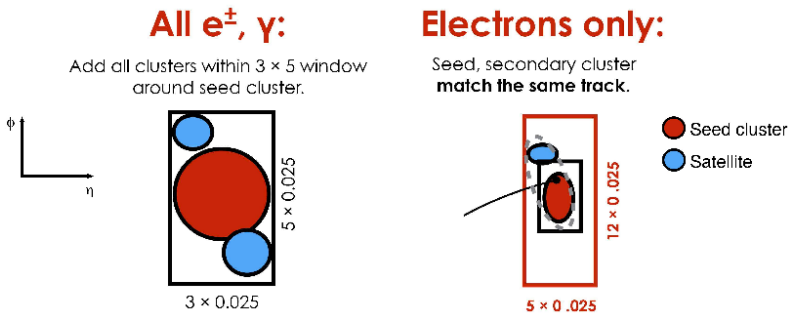


Figure 6.3: Schematic overview of the formation of superclusters during electron reconstruction [188].

ter begins by ordering all electromagnetic topological clusters by their transverse energy and selecting the highest- E_T cluster as the seed. This seed must not already be assigned to another supercluster, and the reconstructed track matched to it must carry at least four hits in either the Pixel detector or the SCT [188]. Once a valid seed is identified, additional “satellite” topoclusters are incorporated within a sliding window of 3×5 or 5×12 calorimeter cells (corresponding to $\Delta\eta \times \Delta\phi = 0.075 \times 0.125$ and 0.125×0.300 , respectively) centered on the seed's energy-weighted barycenter. The smaller window captures nearby secondary electromagnetic showers, while the larger one recovers energy radiated via bremsstrahlung. Finally, the assembled supercluster is matched to its track using the same η - ϕ proximity criteria described before, yielding the fully reconstructed electron object used in subsequent physics analyses.

However, this reconstruction procedure is based on the raw energy measurements of both electrons and photons, derived from the sum of cell energies. To achieve the highest possible precision, these energy measurements must be calibrated and are therefore firstly optimized via a BDT regression trained on

Monte Carlo simulation, which combines the energy deposits across the three longitudinal calorimeter layers. Subsequently, the response of each individual layer is calibrated separately to correct for its E_T -dependent behavior, and the same corrections are applied identically to both data and simulation samples.

After layer-by-layer corrections, residual discrepancies between data and simulation, arising from effects such as azimuthal non-uniformities in the calorimeter’s granularity, are removed by applying additional region-dependent corrections to the data. Finally, the absolute energy scale and resolution are tuned using large samples of $Z \rightarrow e^+e^-$ decays, ensuring that the reconstructed Z peak in data aligns with the simulation. Any remaining resolution differences are corrected by smearing the simulated energies, and the overall procedure is validated and its uncertainties quantified using $J/\psi \rightarrow e^+e^-$ events.

6.2 Electron Identification

As already mentioned, there are other types of physical objects that can mimic the characteristic signature left by electrons in the ATLAS detector, and can therefore end up being reconstructed as electron candidates.

In the physics analyses carried out within the collaboration, the background coming from these objects needs to be reduced as much as possible. Moreover, not all real electrons are to be considered as signal in many cases. Only prompt isolated electrons originating from the decay of heavy bosons such as the W, Z, and Higgs bosons are of interest, while those coming from the decay of charged quarks or photon conversions are also considered as background.

Therefore, in order to efficiently classify the electron candidates of interest, a set of selections must be applied to the candidates after the reconstruction step, which is what is known as identification. To identify the types of electrons, discriminants are typically defined based on observables or features of the physical objects that allow for a discrimination between prompt and background electrons, for instance, since it is a generic procedure adopted for other types of physical objects as well, both in ATLAS and in other experiments such as CMS.

These discriminants can be defined in various ways, and the following describes the Likelihood-based approach, used since the beginning of the Run 2 period, and a novel identification algorithm based on Deep Neural Networks, which is a focus of this thesis and will therefore be discussed in more detail.

Finally, the identification process is completed by using the output of that discriminant, on which certain thresholds are optimised targeting specific values of signal identification efficiency and background rejection. Since the be-

haviour of electrons generally varies as a function of their energy and of the detector region under consideration, related to how they interact with the detector material, these thresholds are typically defined in bins of the electron's p_T and η , and are encapsulated in what are known as identification Working Points (WPs). These WPs generally also include other requirements on additional variables, as will be seen later, and finally different working points obtained from the same discriminant or approach are grouped into identification menus, which are ultimately what is provided from the Combined Performance (CP) groups to the physics analysis groups.

6.2.1 Likelihood-based identification

So far, electron identification in ATLAS has been based on the Likelihood (LH) approach [184, 188], which relies on a wide range of information from different detector subsystems. This algorithm uses high-level input variables defined from the properties of electrons and the information they leave as they pass through the detector. These variables will be detailed later, since they are largely shared with those used in the training of the DNN, and further information can be found in Ref. [184].

A central aspect in the construction of the LH discriminant is the definition of one-dimensional Probability Density Functions (PDFs) for each input variable, separately for signal and background electrons, based either on real data or on the simulations previously described. The discriminant is then constructed from these PDFs, which reveals one of the limitations of this method: the correlations between variables are lost when creating these density functions, which are obtained by applying a Kernel Density Estimator (KDE) to histograms of the variables, using the TMVA toolkit [169].

Therefore, the likelihood of an electron candidate being signal (L_S) or background (L_B) is given by:

$$L_{S(B)}(\mathbf{x}) = \prod_i P_{S(B),i}(x_i), \quad (6.2)$$

where $P_{S(B),i}(x_i)$ are the signal (background) PDFs, and x_i is simply the value of the i -th input variable, so the likelihood is just the product of all PDFs. Then, the likelihood discriminant, d_L , is simply obtained as:

$$d_L = \frac{L_S}{L_S + L_B}, \quad (6.3)$$

which achieves the goal of clearly separating the signal and background distributions, as can be seen in the example in Figure 6.4.

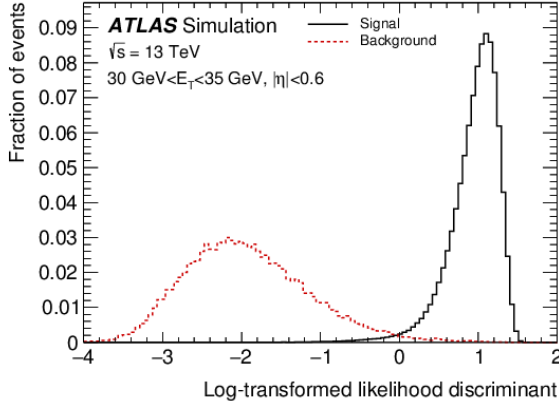


Figure 6.4: Likelihood discriminant distributions obtained in a particular p_T and η bin, for signal and background computed for simulated electrons corresponding to R.21 Run 2 period [184]. An additional monotonic transformation is applied to the discriminants which does not change its classification power.

As previously mentioned, the PDFs of the variables are parametrised in different bins of p_T and η , and the same applies when building the discriminant and defining the thresholds that form the Working Points (WPs).

The requirements associated with these cuts on the discriminant, and applied to determine whether an electron candidate passes a given WP, include a certain number of hits in different parts of the tracking detectors and also requirements on the ambiguity type. This ambiguity type is a kind of flag assigned to the candidate during reconstruction, providing information on whether the topocluster associated with the electron was also reconstructed as a photon. Each WP encapsulates different requirements, and in this thesis we use *LHLoose*, *LHMedium*, and *LHTight*, ordered from highest to lowest in signal identification efficiency, and the reverse in terms of background rejection. They are subsets of each other, meaning that if an electron passes the *LHTight* WP, it also passes the other two.

Regarding the LH menu used in subsequent calculations, the PDFs were obtained from data for the signal in order to ensure the best possible performance when applied to real data, and also for the background PDFs, as these result in distributions that are even less signal-like than those derived from Monte Carlo simulations. This is precisely what is desired for the method to work effectively. The selection used to obtain the purest possible sample of candidates for both types is fully detailed in Ref. [189].

In summary, in order to construct the Probability Density Functions (PDFs) a tag-and-probe method is applied. Signal electrons are selected from $Z \rightarrow$

e^+e^- or $J/\psi \rightarrow e^+e^-$ decays. Events with $p_T > 15$ GeV are taken from Z decays, while lower- p_T electrons ($p_T \leq 15$ GeV) come from J/ψ decays. A tightly identified and isolated “tag” electron is required, and a “probe” electron is selected if the invariant mass of the pair matches the Z or J/ψ boson mass. No ID or isolation is applied to the probe, ensuring unbiased signal distributions.

Background PDFs are obtained from multi-jet events. Due to their large cross-section, loose selection of reconstructed electrons yields mostly background. To improve purity, $Z \rightarrow e^+e^-$ and $W \rightarrow e\nu$ decays are vetoed. The Z veto removes events with a second electron forming a mass near the Z boson. The W veto applies a cut on the transverse mass:

$$m_T = \sqrt{2p_T^\ell E_T^{\text{miss}}(1 - \cos \Delta\phi)},$$

with $\Delta\phi$ being the azimuthal angle between the lepton and the missing transverse momentum. This also removes electrons from top-quark decays.

6.2.2 Deep neural network for electron identification

Until now, electron identification in ATLAS has not relied on any ML technique. During the Run 1 period, a cut-based selection was used, applying rectangular cuts directly optimised on characteristic observables of the electron candidates. Later, during Run 2, the strategy evolved into the LH approach, described in the previous section. This method uses PDFs derived from the distributions of variables that are very similar to those used in the former cut-based method.

While the LH method has proven effective selecting signal electrons with high efficiency and background rejection, recent advances in ML have introduced new possibilities for improving classification performance and signal-to-background discrimination in high-energy physics. In particular, deep neural networks (DNNs) have demonstrated a strong ability to model complex correlations among input variables, overcoming one of the main limitations of the LH model.

This section presents an alternative algorithm based on a DNN, developed as an improved replacement for the LH discriminant using a similar set of high-level input variables.

A detailed technical description of the implemented algorithm can be found in Ref. [190], initially developed and validated for Run 2 Release 21. More general information on the statistical principles and methodology of neural networks is provided in Section 5.3.

Here, the focus is placed on the specific application to electron identification, training and optimising the DNN using simulated samples to distinguish prompt isolated electrons from various background sources. The following describes the selection of samples and the definition of training classes, the choice and preprocessing of input variables, the training procedure and performance, and finally, the definition of the working points derived from the DNN output.

6.2.2.1 Samples and electrons selection

The first step to prepare the DNN for electron identification is to define the training, validation, and test datasets that will feed the algorithm. As previously mentioned, simulated electron candidates are used for this purpose, extracted from different processes generated as described in Section 3.4.1, corresponding to the Run 2 R.22 period.

Signal electrons are selected from $Z \rightarrow e^+e^-$ decays, complemented with $J/\psi \rightarrow e^+e^-$ resonances to increase statistics in the low- p_T region. As sources of the main background classes that mimic electron-like signatures, we use the *JF17* sample, complemented with a sample of simulated $t\bar{t}$ events, from which only events containing at least one lepton in the final state are considered.

These samples are processed through the TAGANDPROBE analysis software, a GITLAB [191] project maintained by the Combined Performance e/γ group, focused on the treatment and performance measurements of electrons and photons in ATLAS. This framework provides a convenient format for storing the electron candidates of each type, allowing for the application of certain quality prerequisites.

In our case, this preselection is minimal and consists of requiring all reconstructed electrons to have a transverse momentum of at least 4.5 GeV, a minimum of two hits in the pixel subdetector, and at least eight hits in the silicon detector systems. Additionally, only electrons within the region $|\eta| < 2.47$ are considered. The electron candidates are corrected for energy scale and resolution using the TAGANDPROBE framework, and further selection criteria are applied to reject candidates associated with problematic detector regions or poorly reconstructed calorimeter clusters.

Finally, it is important to note that, from Z boson decays, only electron candidates with $p_T > 15$ GeV are used, since lower-energy regions suffer from an increased population of background electrons. For p_T below this threshold, electrons from J/ψ decays are used instead. Further requirements on the origin of the electrons are applied to ensure that different types of candidates are selected from each sample, resulting in six distinct classes, which will be defined in the following.

6.2.2.2 Classes

One of the most important steps when training a supervised classifier like a deep neural network is the definition of the target classes. In our case, this translates into deciding which electron candidates are to be considered signal, and which ones are background. It is also important to note that similarities to prompt electrons are inherently different between different types of background electrons, so any identification approach will have different separation power depending on the type of fake object.

This classification is far from trivial, since borderline or grey cases naturally arise in many physics contexts, and a good classification scheme should be general enough to work for a wide range of analyses. The class labels used in this study are based on a truth classification, which uses information such as the origin and type of the electron, as well as those of its mother particles. This is information that can be uniquely accessed in our produced MC simulations.

We define the following six mutually exclusive classes:

Class	Description	Label	Sample
Prompt electrons	Electrons from prompt decays such as $Z \rightarrow ee$, $W \rightarrow e\nu$, or $J/\psi \rightarrow ee$, including FSR or bremsstrahlung if the origin is a prompt electron. Reconstructed charge must match truth one.	E1	$Z \rightarrow ee, J/\psi \rightarrow ee$
Charge-flips	Prompt electrons with misreconstructed charge, mostly due to tracking ambiguities. For bremsstrahlung, it is considered as truth charge the one of the original prompt electron.	CF	$Z \rightarrow ee, J/\psi \rightarrow ee$
Photon conversions	Electrons from conversions of prompt photons into e^+e^- . Prompt photons misreconstructed as electrons are also included here.	PC	$JF17, t\bar{t}$
Heavy-flavour electrons	Electrons from semileptonic b - or c -hadron decays. Typically non-isolated and slightly displaced.	HF	$JF17, t\bar{t}$
Light-flavour e/γ	Electrons or photons from light-quark hadron decays, including intermediate conversions like $\pi^0 \rightarrow \gamma\gamma$ with subsequent $\gamma \rightarrow ee$.	LFEg	$JF17$
Light-flavour hadrons	Hadrons misidentified as electrons due to anomalous energy deposits in the EM calorimeter.	LFH	$JF17$

Table 6.1: Definition of the six different classes of electron candidates used to train the DNN and throughout this thesis. Each class is defined based on truth information, which is known precisely from the simulated samples. The table has been adapted from Ref. [190].

The previous table includes the definition of each class, as well as the corresponding simulated samples from which candidates are selected. The two signal-like classes, namely E1 (prompt electrons) and CF (charge-flip electrons), are extracted from $Z \rightarrow ee$ and $J/\psi \rightarrow ee$ events.

The remaining four background-like classes are primarily obtained from the *JF17* sample. As explained, the $t\bar{t}$ sample is used to increase the statistics for electrons originating from Heavy-Flavour decays and photon conversion electrons.

Prompt electrons are consistently treated as signal throughout this work. Conversely, electrons from photon conversions, Heavy-Flavour decays, Light-Flavour hadron decays, as well as hadrons misidentified as electrons, are always considered background. However, the classification of charge-flip electrons is less straightforward, since even if they originate from prompt processes, their charge is incorrectly reconstructed. Therefore, whether they are considered as signal or background depends on the specific physics analysis. In single-lepton analyses, the reconstructed charge is typically irrelevant, allowing charge-flip electrons to be included as signal to increase statistics. Even in charge-sensitive analyses their impact is often negligible due to the low misidentification rate. However, in final states with two same-sign leptons, charge-flip electrons are treated as background, as they can mimic the signal while originating from more common SM processes.

Given the significantly different rejection power across background classes, Receiver Operating Characteristic (ROC) curves are presented both individually for each background class and inclusively for all backgrounds combined. Due to their special status, charge-flip electrons are excluded from both signal and background definitions in the main performance evaluation.

It is interesting to dedicate a few more words to the ambiguity in the definition of electron classes. As discussed at the beginning of this section, not all electrons can be assigned to signal or background categories in a straightforward way. For example, in analyses targeting $H \rightarrow \tau^+\tau^-$ decays, electrons originating from τ -lepton decays, although slightly displaced, are still prompt and exhibit shower shapes nearly identical to those from $Z \rightarrow ee$, except for impact parameter-related variables, as can be seen in Figure 6.5. Relying too heavily on displacement for classification could thus reduce the efficiency for τ_e electrons. A similar situation arises with electrons from Heavy-Flavour decays: although generally treated as background for training purposes, some analyses may require keeping them or applying dedicated rejection techniques such as PLIT. In this context, the class definitions used in this work are optimised for the training of the DNN, but they may need to be reinterpreted depending on the specific analysis requirements.

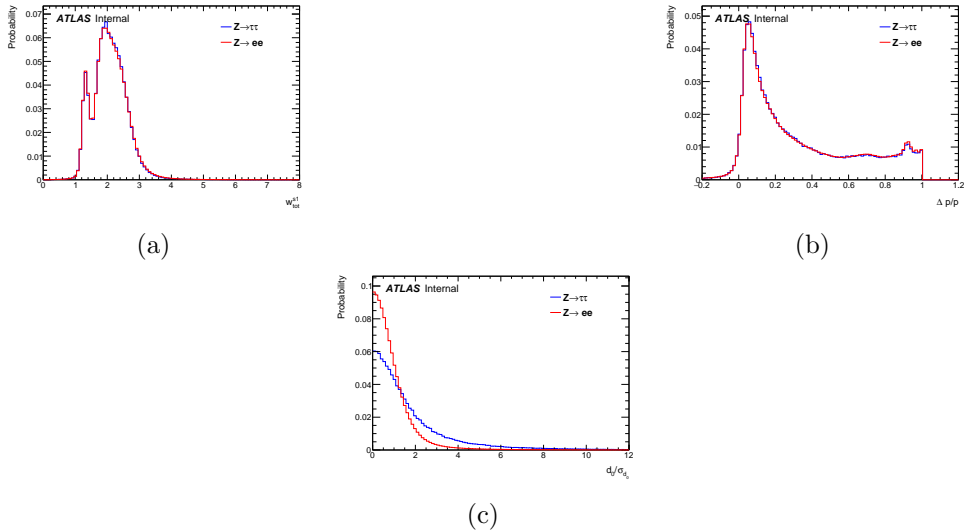


Figure 6.5: Comparison of distribution for two shower-shape related variables (a) and (b), and an impact parameter related one (c), between prompt electrons coming from $Z \rightarrow ee$ decay and τ_e electrons from $Z \rightarrow \tau\tau$. The definition of these variables is detailed below.

6.2.2.3 Inputs and preprocessing

In order to feed our DNN with the features of the different classes of electron candidates, information left by these particles in almost all ATLAS subdetectors (except the MS) is used, as well as matching information between the tracking systems and energy deposits in the calorimeter.

In Table 6.2, all the variables used as input are listed, along with a brief definition for each of them, extracted by combining all the information recorded by the detector.

As specified, there are some variables that are not used as input features for training the DNN, but are instead applied as simple rectangular cuts afterwards, in the optimisation step that will be detailed in the next section, since in some specific cases they could provide additional discrimination power. There are also other variables that, in addition to being used for training, are also employed for these rectangular cuts, such as n_{Si} and n_{Pixel} .

Type	Description	Name	Usage
Hadronic leakage	Ratio of E_T in the first layer of the HCAL to E_T of the EM cluster.	R_{had1}	DNN
	Ratio of E_T in the HCAL to E_T of the EM cluster.	R_{had}	DNN

Third layer of EM calorimeter	Ratio of the energy in the third layer to the total energy in the ECAL.	f_3	DNN
First layer of EM calorimeter	Lateral shower width in the second layer of the ECAL.	$w_{\eta 2}$	DNN
	Ratio of the energy in 3×3 cells in the second layer of the ECAL over the energy in 7×7 cells centered at the electron cluster position.	R_η	DNN
	Ratio of the energy in 3×7 cells in the second layer of the ECAL over the energy in 7×7 cells centered at the electron cluster position.	R_ϕ	DNN
	Shower width in the first layer of the ECAL.	w_{stot}	DNN
	Ratio of the energy difference between the maximum energy deposit and the energy deposit in a secondary maximum in the cluster to the sum of these energies in the first layer of the ECAL.	E_{ratio}	DNN
	Ratio of the energy in the first layer to the total energy in the ECAL.	f_1	DNN
Track conditions	Number of hits in the innermost Pixel layer.	$n_{Innermost}$	DNN
	Number of hits in the Pixel detector.	n_{Pixel}	DNN + C
	Number of hits in the SCT detectors.	n_{SCT}	DNN
	Extra hit required in the insertable BLayer.	$BLayer$	C
	Total number of hits in the Pixel and SCT detectors.	n_{Si}	DNN + C
	Charged transverse impact parameter relative to the beam-line.	d_0	DNN
	Electron weighted average charge over all associated SCT tracks.	$SCTWeightedCharge$	DNN
	Significance of transverse impact parameter defined as the ratio of d_0 to its uncertainty.	$ d_0/\sigma(d_0) $	DNN
	Momentum lost by the track between the perigee and the last measurement point divided by the momentum at perigee.	$\Delta p/p$	DNN
TRT	Likelihood probability based on transition radiation in the TRT.	TRT PID	DNN
Track-cluster matching	$\Delta\eta$ between the cluster position in the first layer and the extrapolated track.	$\Delta\eta_1$	DNN
	$\Delta\phi$ between the cluster position in the second layer of the ECAL and the momentum-rescaled track.	$\Delta\phi_{res}$	DNN
	Ratio of the cluster energy to the track momentum.	E/p	DNN
	Transverse energy of the electron measured by the calorimeter system.	E_T	DNN
	Absolute value of the pseudorapidity of the electron.	$ \eta $	DNN
Reconstruction	Output of an ambiguity resolution algorithm to distinguish objects reconstructed as both electrons and photons.	Amb type	C

Table 6.2: Description, name, and usage of the input variables used for the electron identification DNN. For those variables in which it is specified "C" in usage, it means that they are used to perform rectangular cuts as additional requirements when defining the DNN working points. When defining the variables constructed using the second layer of the calorimeter, 3×3 , 3×5 , 3×7 , and 7×7 refer to areas of $\Delta\eta \times \Delta\phi$ space in units of 0.025×0.0245 . Description based on [190].

As previously mentioned, the choice of input variables is not exactly the same as the one used to construct the LH discriminant [184]. First of all, the E_T and η of the electron candidates appear indirectly in the LH construction, since the PDFs are provided in different bins of these variables in order to account for the differences in the kinematic features of the candidates across the various regions of the phase space. Since replicating this binning strategy for the DNN would be too costly, we instead include these variables as inputs to provide the model with information about the phase space, although, as we will see, they are treated with special care.

Moreover, the number of hits in the main track of our electron candidates is not only used for rectangular cuts, as done in the LH approach, but also as input variables in the training, as already specified, together with other variables like E/p and w_{stot} .

Finally, and most advantageously, we are able to include highly correlated variables, such as R_{had1} and R_{had} , which capture—at different levels—the fraction of energy from the EM cluster that leaks into the hadronic calorimeter system. In the LH construction, by definition, only one of these variables can be used, depending on the detector geometry region. In contrast, machine learning algorithms such as DNNs can greatly benefit from input feature correlations, especially in classification tasks where these correlations differ across the various classes.

It is also important to highlight that two variables included in the list are not used in the LH approach nor in the previous version of this DNN [190].

The first of these variables is the so-called *SCTWeightedCharge*, which is obtained as:

$$\text{SCT-weighted-charge} = q^e \sum_{trk} (q^{trk} N_{SCT}^{trk}) / \sum_{trk} N_{SCT}^{trk} \quad (6.4)$$

where q^e is the charge of the electron (as given by its primary track), N_{SCT}^{trk} is the number of hits in the SCT for a given track associated to the electron, and q^{trk} is the charge associated to that track. This variable can be interpreted

as the electron charge weighted over all tracks associated with the electron, beyond the primary one. By construction, it takes a value of one if the electron has only one associated track. However, in cases where multiple tracks are associated to the same electron candidate, the value may differ from one, which is typically more likely when the candidate corresponds to a charge-flip electron, i.e., an electron whose charge has been misidentified.

The second variable is the so-called charged impact parameter, $q \times d_0$, which replaces the d_0 variable used previously.

The main interest of these two variables lies in their discriminating power for rejecting charge-flip electrons against prompt electrons [192], i.e., prompt electron candidates with correctly identified charge. This provides the DNN with an additional potential to identify this specific class of background (or signal, depending on the analysis) electrons. This feature will be discussed in more detail in a later section.

Shower-shape variables corrections

It is worth starting by defining what a shower-shape variable is in this context. As the name suggests, these are the variables already described in Table 6.2 that characterise the shape of the electromagnetic shower left by the electron candidates in the calorimeter system.

The main issue that arises here is that, in order to train our DNN and ensure that it performs well when applied to real data, we ideally want the distributions of the input variables for simulated electrons to closely resemble those of real electrons coming from data. However, due to imperfections in the detector modelling, the disagreement between MC simulations and data can be too large, especially for those variables involving calorimeter signal readouts (such as energy leakage due to undesired connections between LAr cells, commonly referred to as *cross-talk*).

Corrections are therefore derived for these shower-shape variables in cases where the differences between data and MC are too significant. These corrections are based on individual affine transformations, applied in bins of E_T and η , such that the mean of the distribution and/or its width is shifted, depending on the severity of the discrepancy.

The corrections are derived by comparing the distributions evaluated for electron candidates extracted from data and MC simulations using a simple tag-and-probe technique. The transformation parameters are obtained by minimising the χ^2 between the two distributions. More details can be found in Ref. [184], but an example of the application of these corrections can be seen in Figure 6.6 for the variables f_3 and R_{had} .

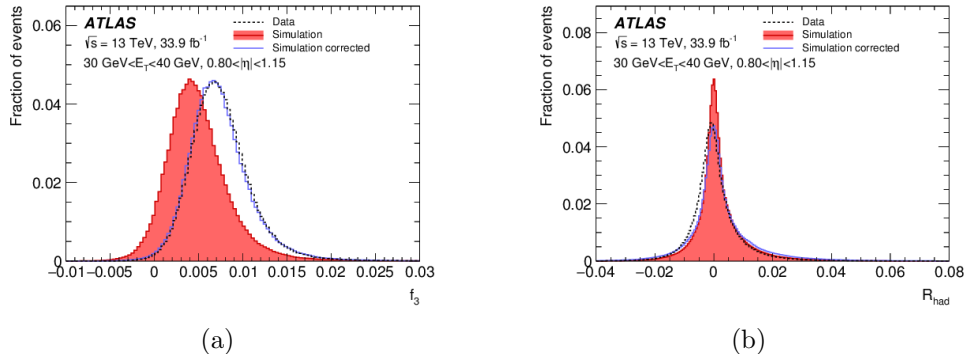


Figure 6.6: Comparison of (a) f_3 and (b) R_{had} shower-shape distributions for data and simulated electrons with and without corrections applied, within certain E_T and η bins: $30\text{GeV} < E_T < 40\text{GeV}$ and $0.8 < |\eta| < 1.15$. Source in Ref. [184]

It can be observed that, in the case of f_3 , the simulated values of this variable are centred around a mean value that is slightly shifted with respect to the real data distribution. Therefore, in this case, a small shift in the mean of the distribution would be sufficient. For R_{had} , however, it is also evident that in order to match the data values, it is necessary not only to shift the distribution but also to broaden it slightly around the mean value, applying a correction to the width as well.

This correction method, often referred to as *fudging* in this context, is known as the *Shift & Stretch* approach. Other strategies exist to address discrepancies between data and MC simulations, such as the *Gaussian Smearing* approach, which assumes that the noise-like imperfections introduced by the calorimeter can be incorporated into MC simulations through Gaussian approximations [193].

This smearing approach was used to correct the PDFs employed in the construction of the LH discriminant using reprocessed Run-2 data. However, it cannot be applied to the DNN input variables. The reason is that these Gaussian corrections introduce artificial correlations in the input distributions, which ultimately degrade the performance of the DNN. Unlike the LH method, which is designed to be robust against such effects, DNNs rely on the preservation of meaningful correlations between features.

The *Shift & Stretch* method, on the other hand, applies simple affine transformations that better preserve these correlations. This can be seen in Figure 6.7, where the correlation matrices between input variables are shown for MC simulations before and after each correction approach, as well as for real

data.

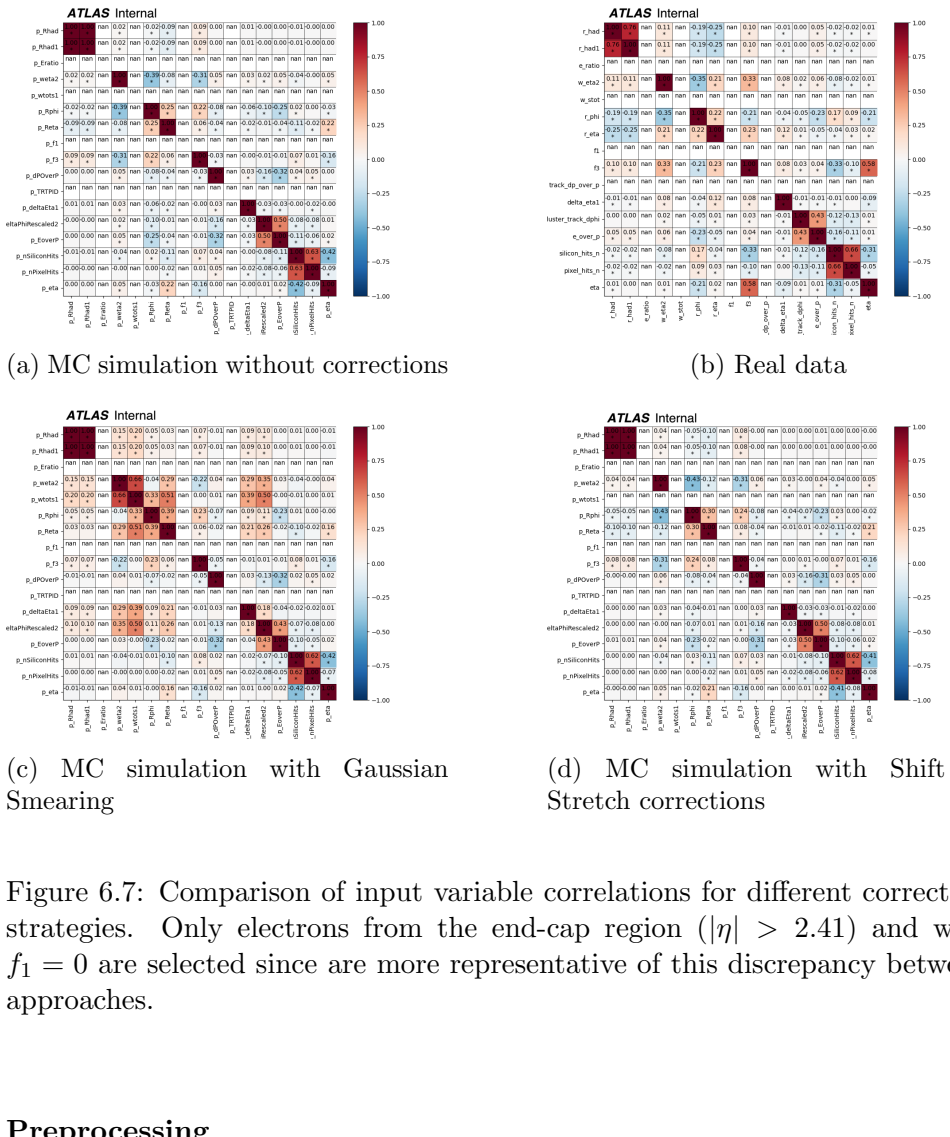


Figure 6.7: Comparison of input variable correlations for different correction strategies. Only electrons from the end-cap region ($|\eta| > 2.41$) and with $f_1 = 0$ are selected since are more representative of this discrepancy between approaches.

Preprocessing

Before proceeding to the training of our DNN, it is important to consider that different physical processes have been used to populate the various electron candidate classes we defined. Consequently, the transverse energy (E_T) distribution can vary significantly among classes. For instance, most prompt electrons from $Z \rightarrow e^+e^-$ decays will have $E_T \approx 45$ GeV, corresponding to half of the Z boson mass. This could introduce significant biases and degrade the DNN's performance, as discussed in Section 5.3.1.5. To prevent the network

from distinguishing classes based solely on E_T and η , these input distributions need to be harmonised across all six classes. This is achieved through a combination of downsampling and reweighting.

First, to limit the statistical imbalance, the prompt electron sample is downsampled. Prompt candidates are randomly removed in E_T bins so that, within each bin, their number does not exceed five times the number of background candidates. This effectively reduces the prominent peak at 45 GeV, as illustrated in Figure 6.8c. Due to limited statistics, no downsampling is applied to the charge-flip class, even though a similar peak is present.

Once downsampling is applied, weights are derived to reweight the E_T and η distributions independently for each class. These weights are then combined by multiplying the two, assuming no strong correlation between E_T and η . After reweighting, all distributions are normalised so that the total weight per class remains constant. The resulting harmonised distributions for E_T and η are shown in Figures 6.8d and 6.8e.

The $|\eta|$ reweighting aims for a flat distribution, while for E_T , a shape resembling the Light-Flavour hadron class from the $t\bar{t}$ sample is targeted, featuring a flat region up to 15 GeV followed by a falling slope. This approach reduces the bias efficiently while preserving classification performance. Some residual discrepancies may remain due to slight correlations between E_T and η , especially for the charge-flip class. While a 2D reweighting could mitigate this, it is avoided due to limited statistics at high E_T .

Finally, to equalise the total statistical weight across classes, an additional scaling factor is applied per class after reweighting. This factor ensures that all classes contribute equally in terms of weight, while keeping the global sum of weights unchanged. An example of this normalization is shown in the case of the E_T distribution in Figure 6.8.

The distributions of all input variables after the application of these modifications can be found in Figure 6.9. However, there is still one last step before passing all the inputs distributions through the DNN, which is the transformation of all of them to uniform distributions between zero and one, using empirical quantiles as explained in Section 5.3.1.5. This action facilitates the training of the neural network and speeds up the different steps in the optimization. Figure 6.10 illustrates the impact of this transformation on the R_{had} variable, taken from Ref. [190]. The plot displays the full distribution together with the individual contributions from prompt electrons and Light-Flavour hadrons. After applying the transformation, the overall distribution becomes uniform within the $[0, 1]$ interval.

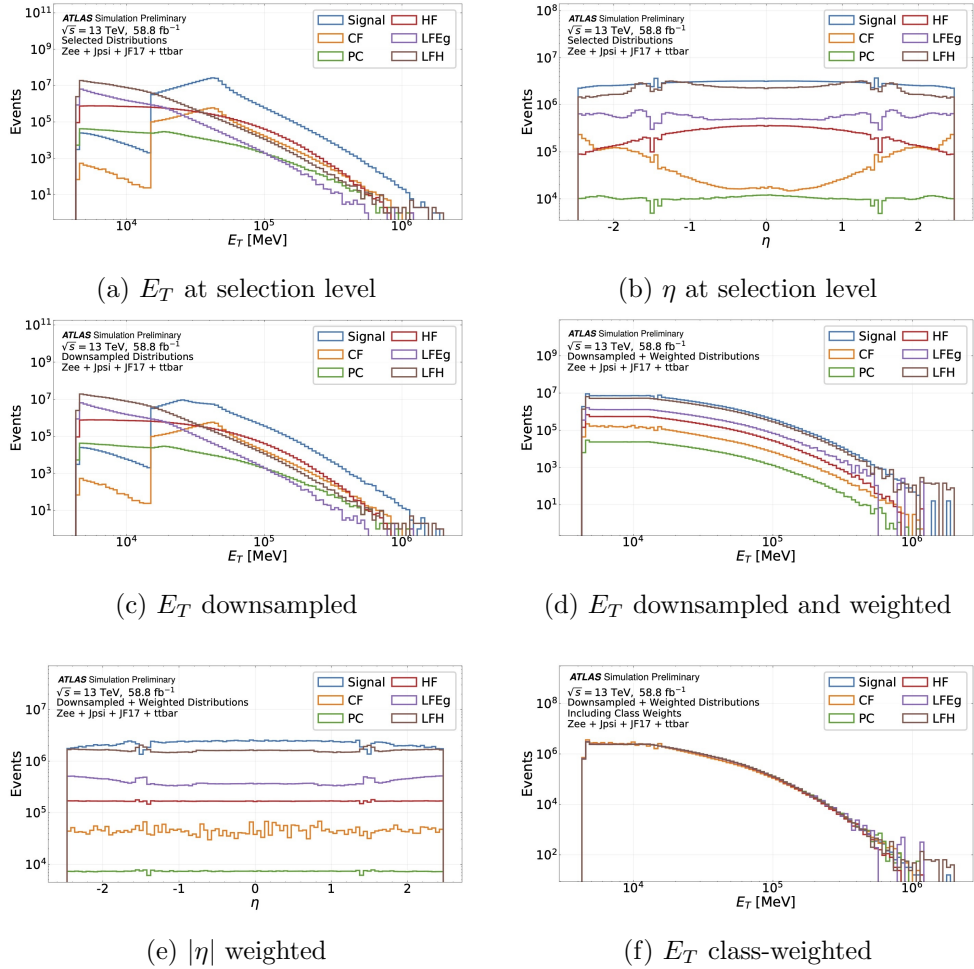


Figure 6.8: Distributions of E_T and $|\eta|$ at electrons' selection level, (a) and (b), E_T after applying downsampling (c) and kinematic reweighting (d), η after flattening reweighting (e), and finally E_T after applying also weights making all the classes equiprobable (f).

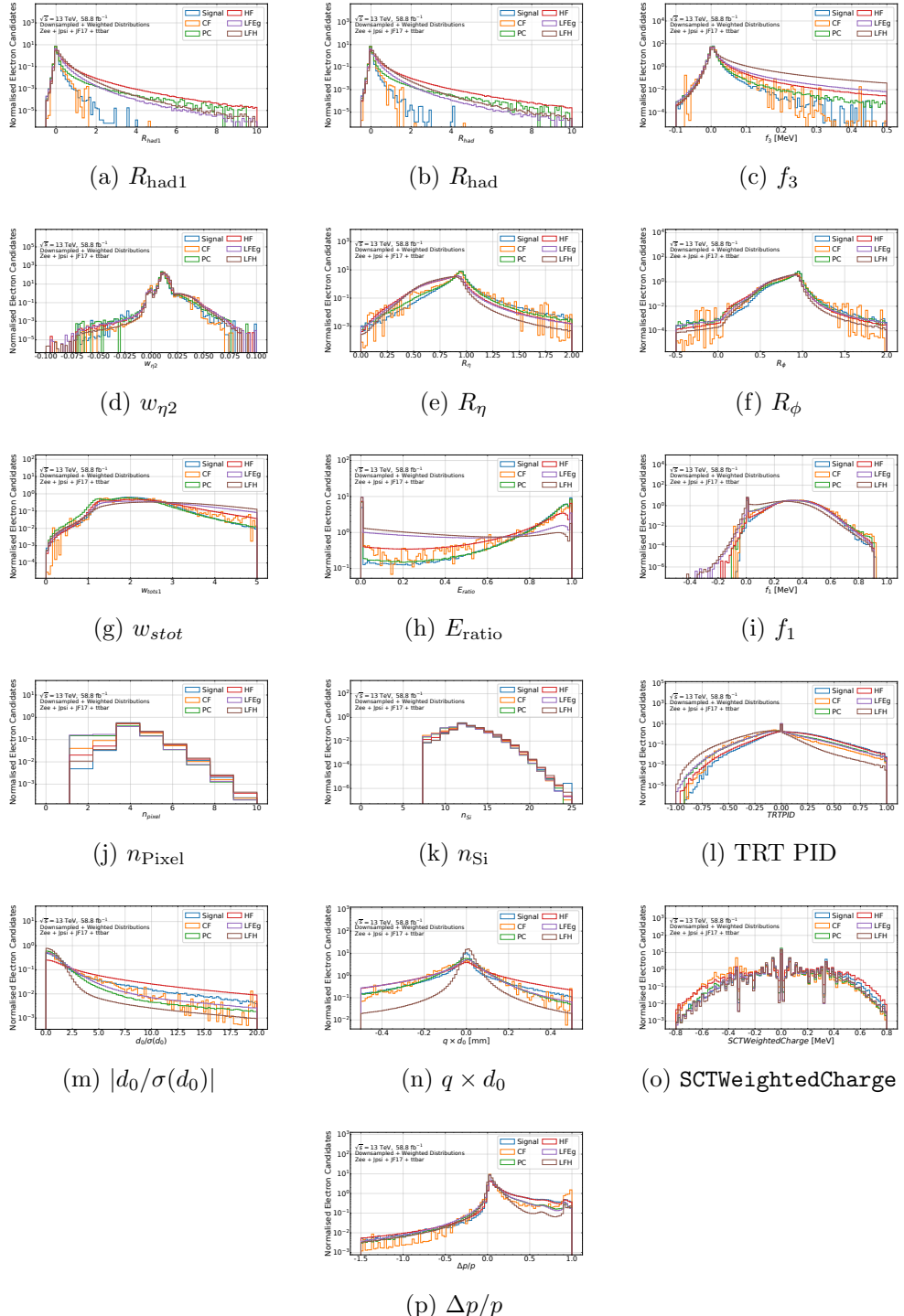


Figure 6.9: Distributions of all the input variables used for DNN training, after preprocessing and reweighting procedures. Only the training subset of the simulated electrons is used to produce these plots.

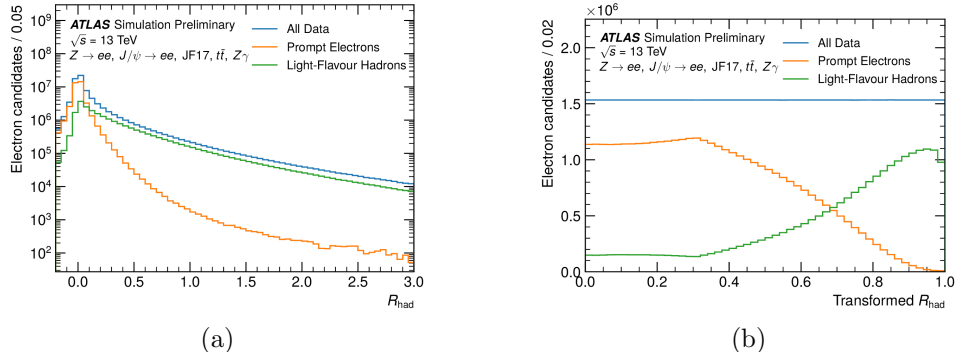


Figure 6.10: Distribution of R_{had} for all candidates, prompt electrons, and Light-Flavour hadrons, shown (a) before and (b) after applying the Quantile-Transformer. Distributions include downsampling and reweighting and only two classes are displayed for clarity. In these studies presented in Ref. [190], an additional $Z\gamma$ input was used.

6.2.2.4 Training procedure

In our specific case, we employed a Deep Neural Network with a total of five hidden layers, each containing 256 nodes. In these hidden layers, the Leaky ReLU activation function is applied to introduce non-linearity, as detailed in Sec. 5.3.1, and batch normalization is also implemented. This algorithm performs a multinomial classification, producing as output a total of six scores, one for prompt electrons and five for each of the background classes. In the final output layer, the Softmax activation function is applied. A schematic diagram of our DNN architecture is shown in Figure 6.11.

This algorithm was implemented and trained using the `TensorFlow` library [176], version 2.4. As previously mentioned, the *Adam* optimizer was used in the training procedure. Regarding the remaining hyperparameters of the neural network, different configurations were tested, and the one showing the best performance was selected. The final training is performed over a total of 100 epochs, retaining as the final result the iteration that yields the lowest loss on the validation dataset.

6.2.2.5 Electron classification

The decision to employ a multinomial classification as the output of our DNN stems from the fact that we distinguish between the different background classes that typically populate our real collision data. There are not only kinematic differences among these classes of electron candidates, but also the

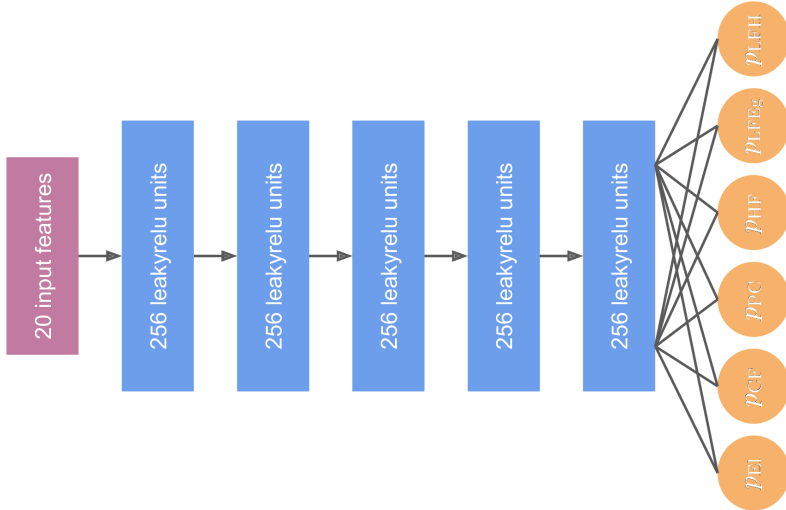


Figure 6.11: Overview diagram of the architecture of the electron identification DNN. It is shown the optimised number of layers and nodes used in the final version. Taken from Ref. [190].

chosen input variables are potentially different for each of them. This is due, for example, to the distinct characteristics of the calorimeter showers they produce in the detector. As an illustration, electron candidates originating from b - or c -hadrons tend to deposit more energy in the innermost layers than prompt electrons, as can be seen in Figure 6.9b.

Nevertheless, for the purpose of identifying signal electrons over the rest of the background candidates, a binomial discrimination must ultimately be performed when defining our working points as a function of efficiencies. For this, the following binomial discriminant is defined, simply combining the output given by the DNN:

$$\mathcal{D}_{el} = \frac{f_{El}p_{El} + (1 - f_{El})p_{CF}}{f_{PPC}p_{PPC} + f_{HFP_{HF}}p_{HF} + f_{LFEg}p_{LFEg} + (1 - f_{PPC} - f_{HF} - f_{LFEg})p_{LFHF}} \quad (6.5)$$

where p_X are the scores provided by the DNN for each class, and f_X are tunable weights or parameters, referred to as *fractions*, which control the relative importance of the different classes in the discriminant. This discriminant separates electron candidates considered as signal, in a generic electron identification problem, which in this case are prompt and Charge-Flip electrons (therefore placed in the numerator), from the remaining background electrons in the denominator.

As mentioned, the fractions f_X are tunable, and to simplify the procedure

it is imposed that their sum equals unity in both numerator and denominator. Depending on the physics analysis under study and the composition of its final states, one background class may be more relevant than another, and this is fully configurable here.

Ideally, the determination of these fractions would be performed directly from real data, just as is done for the LH during training. However, obtaining sufficiently pure and unbiased control regions from data is a highly challenging task, and mixing real data for some classes with MC simulations for others can be risky in a neural network, as the algorithm may directly learn from such mismodellings.

For this reason, in our generic electron identification studies, the fractions are tuned and the performance of the DNN is evaluated using the test dataset obtained from the simulated input samples. As previously explained, the test dataset is a fraction of the initial dataset unseen by the neural network during training, containing electron candidates from all predefined classes and originating from the four physics processes initially presented. This ensures a representative collection of candidates covering the full energy spectrum and all detector regions, which will resemble as closely as possible what will later be encountered in real data.

Moreover, since it would not be meaningful to apply any reweighting or downsampling here, as is done for the training and validation datasets, the tuning of the fractions, the evaluation of the algorithm's performance, and the subsequent derivation of working points are performed in bins of $|\eta|$ and/or E_T . As a figure of merit for estimating the performance of our algorithm and comparing it to the LH, we use ROC curves, already described in Sec. 5.3. Before constructing the discriminant, we must first determine the fractions to be used.

The calculation of the f_X is performed in different $|\eta|$ bins to account for variations in the spectra of the different electron candidate classes. The same fractions are applied across the full E_T range to obtain a smooth and continuous discriminant over the entire energy spectrum.

The optimal f_X values are determined by maximising the Area Under the Curve (AUC) of the ROC between 70% and 95% signal efficiency, which essentially covers the typical range used in most working points for electron identification. The $|\eta|$ bins employed here are broader than those used later when defining the DNN working points, which apply cuts on the discriminant as explained in Sec. 6.2.2.7. Table 6.3 lists the $|\eta|$ and E_T bin boundaries used in each case.

As mentioned, the f_X values obtained in these bins from our test sample are optimal for our studies. However, in other analyses the dataset composition

Use	Edges
Discriminant cuts	0.0, 0.1, 0.6, 0.8, 1.15, 1.37, 1.52, 1.81, 2.01, 2.37, 2.47
f_X optimisation	0.0, 0.8, 1.37, 1.52, 2.01, 2.47

Use	Edges
Discriminant cuts	4, 7, 10, 15, 20, 25, 30, 35, 40, 45, ∞

Table 6.3: Bin edges used for the discriminant cuts and for the f_X optimisation.

will very likely differ, and these values can therefore be adjusted accordingly.

With the \mathcal{D}_{el} discriminant now defined, Figure ?? shows its distribution evaluated for the different electron candidate classes, for a specific $|\eta|$ and E_T bin. The relative composition of each background electron class in the test sample used can be found in Table ??, both inclusively and for the specific kinematic bin under study ($E_T, |\eta|$).

(a) Inclusive			(b) $15 < E_T \leq 20$ GeV, $0.0 < \eta \leq 0.8$		
Class	Fraction [%]	Stat. error	Class	Fraction [%]	Stat. error
Photon Conversions	0.325 \pm 0.000		Photon Conversions	0.611 \pm 0.004	
Heavy-Flavour	7.444 \pm 0.002		Heavy-Flavour	19.658 \pm 0.024	
Light-Flavour e/ γ	17.731 \pm 0.003		Light-Flavour e/ γ	11.946 \pm 0.019	
Light-Flavour Hadrons	71.796 \pm 0.007		Light-Flavour Hadrons	66.630 \pm 0.045	

Table 6.4: Fractions and statistical errors for all candidates and for the selected kinematic bin.

In Figure 6.12, it can be observed that both signal electron classes, prompt and Charge-Flip, reach higher discriminant values, showing a more or less pronounced peak compared to the other background classes. Prompt electrons present a more distinctive distribution than Charge-Flip electrons, although in both cases there is a considerable population of Heavy-Flavour and Photon-Conversion background candidates toward the higher end of the range. However, these background distributions also tend to peak at lower discriminant values, which is equally important for achieving high identification efficiencies when defining thresholds.

It is worth noting that Heavy-Flavour electrons tend to populate a wide range of discriminant values compared to signal electrons, and in some cases

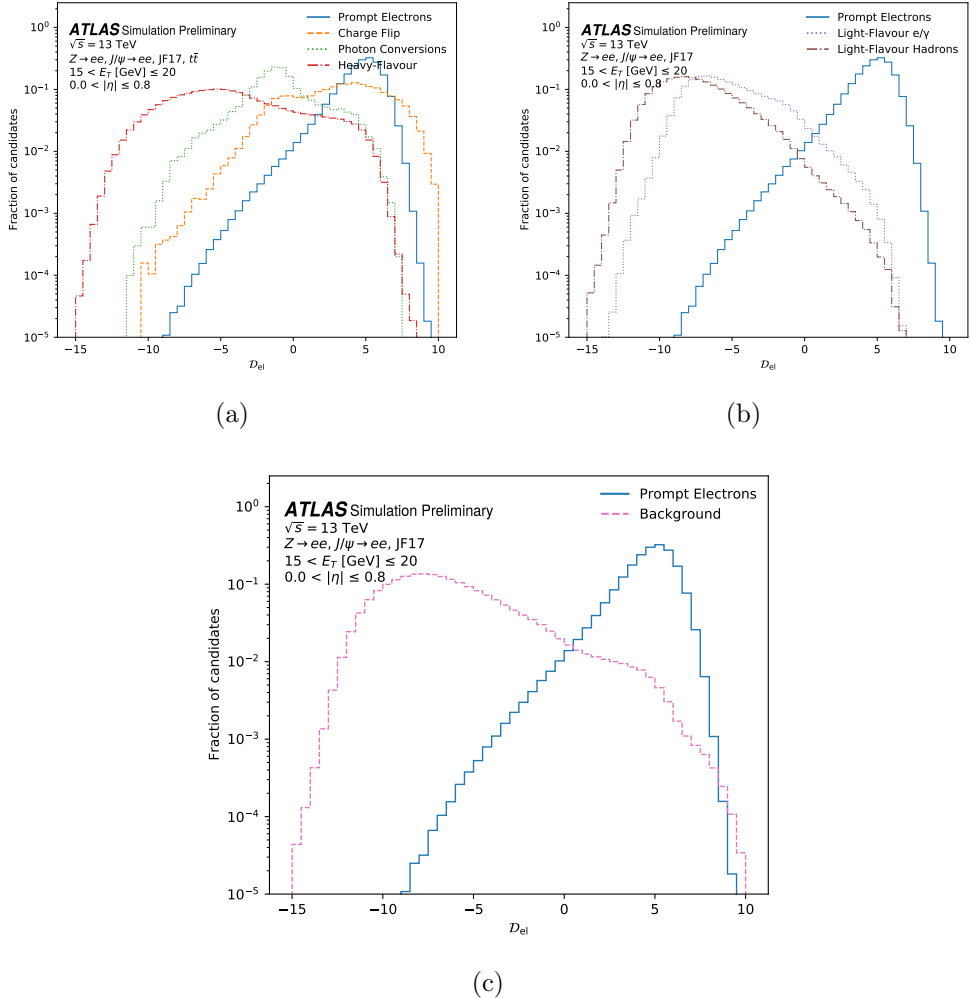


Figure 6.12: Signal discriminant D_{el} of the DNN shown for (a) prompt electrons, Charge-Flip electrons, photon conversions, and electrons from Heavy-Flavour decays; (b) prompt electrons, e/γ objects from Light-Flavour decays, and Light-Flavour hadrons; and (c) prompt electrons versus the combined background (all classes except prompt and Charge-Flip). Candidates satisfy $15 < E_T \leq 20$ GeV and $0.0 < |\eta| \leq 0.8$.

even overlap with Photon-Conversion electrons. This can be explained by the fact that they originate from the decay of heavy quarks ($b-$ and c -hadrons). If these hadrons had a shorter lifetime, their signatures and detector energy deposits would be more similar to those of prompt electrons, or even electrons from converted photons, which themselves can also be prompt. Part of this overlap is in fact reduced by the application of the rectangular cuts discussed previously.

In contrast, as seen in Figure 6.12b, the distributions of the Light-Flavour classes differ clearly from those of prompt electrons, which is highly advantageous and demonstrates the potential of our algorithm to reject these classes.

6.2.2.6 Identification Performance

As mentioned earlier, our performance evaluation is based on the ROC curves of the DNN model. Figure 6.13 shows the ROC curves for prompt electrons against the combined background and each background class individually. The signal definition always includes only prompt electrons, while the LH working points (Loose, Medium, Tight) are represented by single points, located at progressively lower signal efficiencies: Loose around $\varepsilon_{\text{sig}} \sim 0.85$, Medium around 0.75, and Tight around 0.65.

Unlike the LH, the DNN curves shown here do not include the additional *rectangular cuts* listed in Table 6.5, and therefore correspond to a slightly more relaxed selection. The only requirements applied to the DNN candidates are the minimum numbers of silicon detector hits and pixel hits (7 and 1, respectively), which are the same conditions used to define the training, validation, and testing datasets.

Quantitatively, at the LH Loose WP ($\varepsilon_{\text{sig}} \approx 0.85$), the DNN achieves a background rejection about 2 times higher than LH when considering all background classes combined. For Heavy-Flavour decays, the improvement at this efficiency is more evident, with a factor close to 2.2, whereas for Light-Flavour e/γ and undecayed hadrons the rejection also increases, by factors of about 4 and 5, respectively. Photon conversions show a moderate enhancement, with the DNN reaching a rejection about 2 times larger than LH. For Charge-Flip electrons, the improvement is striking, with the DNN achieving a rejection almost 8 times higher than LH in this η region.

Figure 6.14 includes the ROC curve calculated for the rejection of Charge-Flip versus prompt electrons, shown here merely to illustrate the capability of the DNN to separate both signal electron classes. In this case, a modified discriminant is used, where the Charge-Flip term is moved to the denominator. In any case, it is important to note that, since the number of prompt

electrons largely exceeds that of Charge-Flip electrons in any realistic selection, including Charge-Flip candidates within the signal definition would have a negligible impact on the overall signal efficiency.

The overall improvement is clearly visible, with the most notable gains obtained for Light-Flavour hadrons, Light-Flavour e/γ , and Charge-Flip electrons, the latter benefiting greatly from the new variables added to the DNN, providing a significantly enhanced rejection across the full efficiency range. For Heavy-Flavour electrons, the smaller improvement reflects their closer resemblance to prompt electrons, especially in tracking-related observables. Photon conversions also benefit moderately from the DNN, as their rejection is already relatively high with LH.

In summary, the DNN consistently outperforms the LH in all background categories, with the most substantial benefits in rejecting backgrounds that exhibit distinctive calorimeter and tracking signatures, and smaller but still relevant gains for more signal-like sources such as Heavy-Flavour decays.

6.2.2.7 Tuning and working points definition

As a final step, we build the identification menu based on the DNN decision. This menu encapsulates the set of thresholds on the DNN discriminant previously studied, together with the additional rectangular cuts associated with each defined working point.

In our specific case, we combine two discriminants: \mathcal{D}_{el} , defined in Eq. 6.5, and \mathcal{D}_{CF} , defined as the simple ratio $\mathcal{D}_{CF} = p_{el}/p_{CF}$. The first discriminant is used, as already discussed, to separate both signal-electron classes from the main background sources for the most common physics-analysis scenarios. For analyses sensitive to the electron charge in the final state, this can be complemented with the additional discriminant \mathcal{D}_{CF} , which exhibits strong separation power, as illustrated in Figure 6.15, even though the selected $|\eta|$ bin is not the most populated with these candidates. Charge-Flip electrons are expected at higher $|\eta|$, where the material budget and, for instance, bremsstrahlung effects are more severe.

To obtain the identification menus, we first determine thresholds on the \mathcal{D}_{el} discriminant, targeting specific signal-identification efficiencies. These efficiencies are the same as those used to tune the LH discriminant, so we expect a similar signal-identification performance. The procedure is carried out in the previously defined η and E_T bins, setting the discriminant threshold such that the fraction of signal electrons to the right of the cut matches the desired target efficiency.

Subsequently, for the resulting signal-electron sample, the same procedure

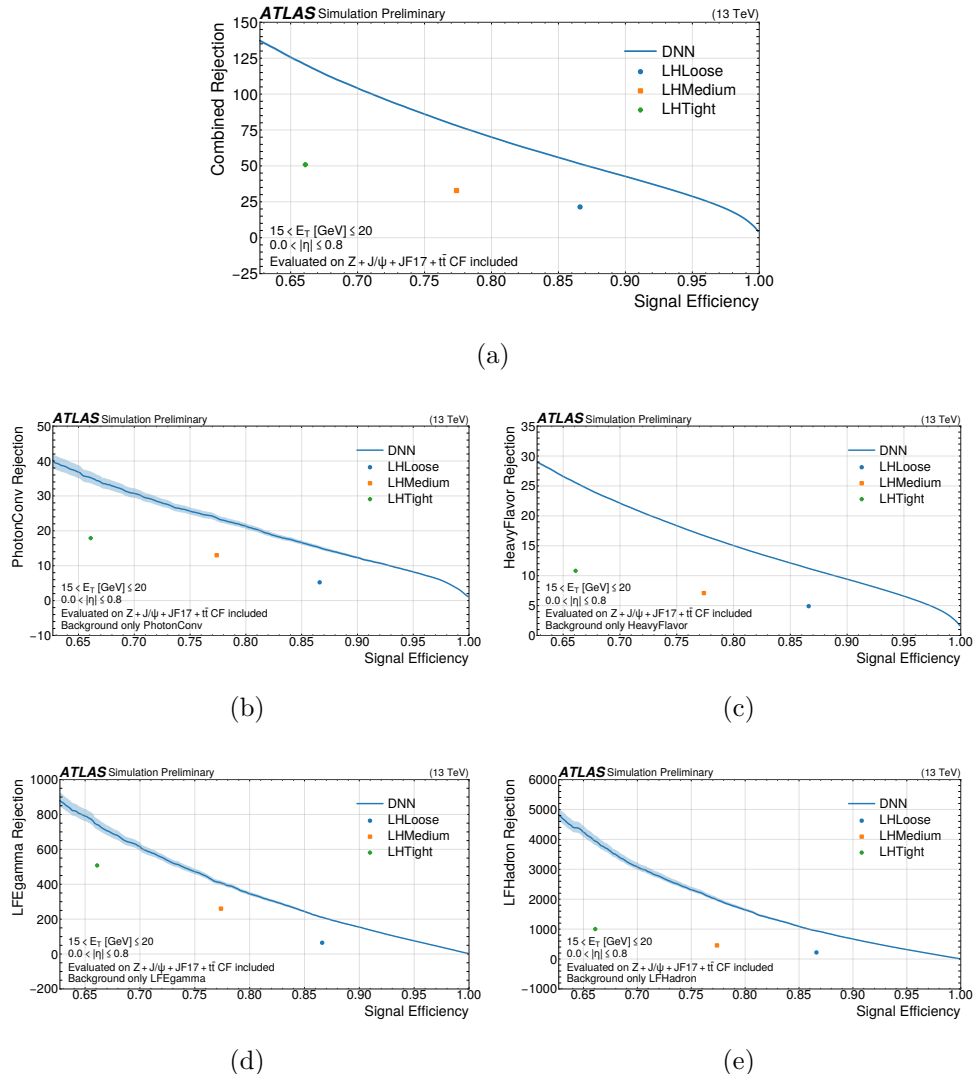


Figure 6.13: Background rejection versus signal efficiency (ROC curves) for prompt electrons against: (a) all background classes combined, (b) electrons from Heavy-Flavour decays, (c) e/γ from Light-Flavour decays, (d) Light-Flavour hadrons, and (e) photon conversions. Curves are shown for a representative ($E_T, |\eta|$) bin, and the statistical uncertainties of the each background rejection are shown as bands.

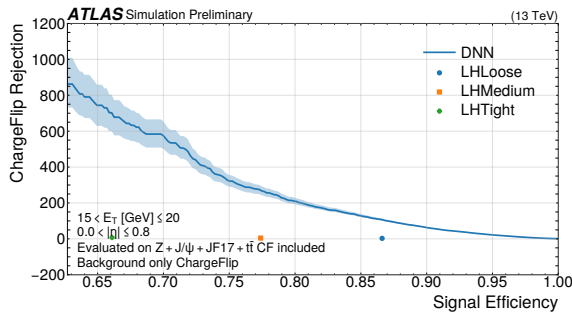


Figure 6.14: Background rejection versus signal efficiency (ROC curve) for prompt electrons against Charge-Flip electrons in a representative ($E_T, |\eta|$) bin, and the statistical uncertainties of the each background rejection are shown as bands

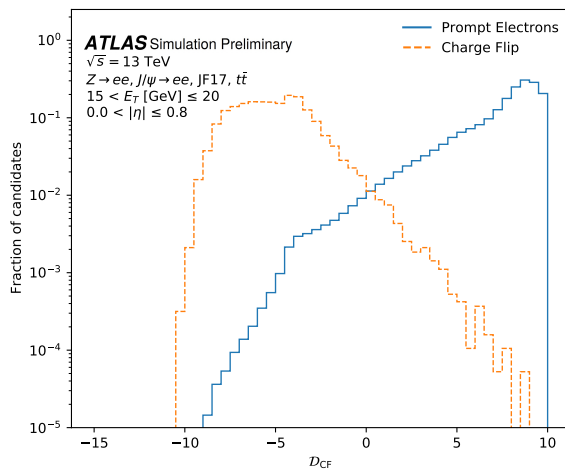


Figure 6.15: Charge-Flip discriminant D_{CF} of the DNN shown for prompt electrons and Charge-Flip electrons. Candidates satisfy $15 < E_T \leq 20 \text{ GeV}$ and $0.0 < |\eta| \leq 0.8$.

is applied to the \mathcal{D}_{CF} discriminant. In this case, the target efficiencies correspond to those obtained with the Charge-Flip Electron Identifier (ECID) [184], a complementary algorithm to LH used for this task. One of the advantages of the DNN is that it naturally incorporates both functionalities into a single output, and is potentially extendable to other definitions of electron candidates.

In addition, for the test-electron dataset where these thresholds are defined, further requirements, parallel to those applied in LH, are imposed depending on the working point. These rectangular cuts are listed in Table 6.5.

WP	$n_{\text{Innermost}}$	Amb bit	n_{pixel}	n_{silicon}
Loose	0	63	≥ 1	≥ 8
Medium	1	63	≥ 2	≥ 8
Tight	1	35	≥ 2	≥ 8

Table 6.5: Additional selection on top of the discriminant for the different WPs, including requirements on the number of pixel and silicon hits.

where the ambiguity bitmask is used to reject electron candidates with specific ambiguity types, ensuring that only candidates with reliable track–cluster associations are retained, and $n_{\text{Innermost}}$ essentially enforces the requirement of an additional hit in the insertable BLayer. In this way, the final menu is represented by two bidimensional matrices in terms of η and E_T , together with the corresponding additional cuts.

6.3 Electron Isolation

After the electron identification stage, it is common to apply additional isolation requirements in order to suppress objects other than signal electrons. In processes such as $Z \rightarrow ee$, signal electrons are typically isolated, meaning that no significant activity is observed around them. In contrast, electrons originating from the decay of heavy-flavour hadrons, such as b -hadrons, may be accompanied by additional activity both in the calorimeter and in the tracking system. To reduce such contamination, isolation *working points* (WPs) are defined, based on thresholds applied to calorimeter and track isolation variables.

For track isolation, two main types of variables are used: $p_T^{\text{cone}XX}$ and $p_T^{\text{varcone}XX}$, where XX can take values such as 20, 30, or 40. Both variables sum the total transverse momentum of all tracks surrounding the electron that are not associated with it. In the case of $p_T^{\text{cone}XX}$, all tracks within a fixed-radius cone of $\Delta R = 0.XX$ are considered. For $p_T^{\text{varcone}XX}$, the cone size is defined as $\Delta R = \min(10/p_T, 0.XX)$. For example, $p_T^{\text{cone}20}$ sums the p_T of all

tracks within a cone of $\Delta R = 0.2$. For isolation WPs, tracks must satisfy a vertex-association requirement and have p_T greater than 1 GeV or 0.5 GeV, with 1 GeV being the minimum used for the isolation WPs considered here.

Similarly, calorimeter isolation is defined through the variable $E_T^{\text{topocone}XX}$, which corresponds to the sum of the transverse energy of *topo-clusters* within a cone of radius $\Delta R = 0.XX$ around the electron. In this case, corrections are applied to account for energy leakage and pile-up effects.

Variable	Cone radius	Summed object	Description
$p_T^{\text{cone}XX}$	Fixed, $\Delta R = 0.XX$	Tracks	Sums the p_T of all tracks not associated with the electron within a fixed-radius cone.
$p_T^{\text{varcone}XX}$	Variable, $\Delta R = \min(10/p_T, 0.XX)$	Tracks	Same as $p_T^{\text{cone}XX}$ but with a cone size that decreases for high- p_T electrons.
$E_T^{\text{topocone}XX}$	Fixed, $\Delta R = 0.XX$	Topo-clusters	Sums the transverse energy of <i>topo-clusters</i> within the cone.

Table 6.6: Summary of the variables used in the definition of electron isolation in ATLAS. The cone radius, summed object, and whether the cone size is fixed or variable are indicated.

6.4 Electron efficiency measurements

Ultimately, the true performance of any electron identification method must be evaluated on real data, especially in the context of specific physics analyses, where it is essential to determine with the highest possible precision the efficiency with which final-state electrons satisfy the chosen identification criteria.

It is not only important to measure the identification efficiency in real data, but also to evaluate it on MC simulated samples. In the end, we must provide an efficiency value for the reconstruction and identification of simulated electrons as well, ensuring that these objects are identified in a manner and with an efficiency as close as possible to that observed in data. As already discussed, certain mismodellings and mismatches exist between simulations and real data. For this reason, the determination of the so-called *Scale Factors* (SFs) is of crucial importance. These are simply defined as the ratio between the identification efficiency measured in data and that obtained in MC events.

In general, the total efficiency for selecting a true electron can be expressed as the product of the efficiencies associated with each selection step applied

to the electron candidate:

$$\epsilon_{\text{tot}} = \epsilon_{\text{reco}} \times \epsilon_{\text{ID}} \times \epsilon_{\text{iso}} \times \epsilon_{\text{trig}}, \quad (6.6)$$

where the first factor, ϵ_{reco} , is computed independently of the others, as it quantifies the reconstruction efficiency, that is, the probability of correctly associating a reconstructed topological energy cluster to a true electron. The remaining efficiencies are measured with respect to the previous step. This is the case for the identification efficiency, which is the only one considered in this section for the DNN algorithm. It is defined as:

$$\epsilon_{\text{ID}} = \frac{N_{\text{ID}}^{\text{WP}}}{N_{\text{reco}}}, \quad (6.7)$$

where $N_{\text{ID}}^{\text{WP}}$ is the number of reconstructed electron candidates passing the identification working point under study, in our case defined using the DNN output, and N_{reco} is the total number of electrons correctly reconstructed in the previous step.

Depending on the requirements imposed by the identification working point, the number of accepted electrons, and therefore the efficiency, will vary. Efficiencies are thus measured as a function of the different working points, and also in bins of E_T and η , since the thresholds are parameterised in these variables. This approach provides a significant advantage: although, as will be shown in the following, efficiency measurements and SFs are derived using a specific physics process, their parametrisation makes them largely analysis-independent and suitable for use in any study involving electrons.

6.4.1 Identification efficiency computation

To determine the identification efficiency of the different WPs in data, an appropriate selection and treatment of the electron candidates is required in order to correctly handle the backgrounds present. The methods employed for this purpose are described in detail in Ref. [194], while here they will be introduced briefly.

To obtain the purest possible dataset of signal electrons from collision data, it is essential to have the best possible control over the background. Since MC simulations are not fully accurate in modelling this contribution, we focus on the extraction of background templates from dedicated control regions, defined as regions of the phase space where specific selections enhance the background electron population. In our case, we concentrate on the measurement of SFs and signal identification efficiencies for electrons with $E_T > 15$ GeV. Two methods are used to obtain a pure dataset of signal electrons and to model the background templates: the Z_{mass} and Z_{iso} methods.

Both approaches are based on events from the $Z \rightarrow e^+e^-$ resonance, initially selected through the Tag-and-Probe technique, already introduced earlier, to obtain an unbiased set of electrons satisfying the ID WP. In the Z_{mass} method, background templates are obtained from the invariant mass distribution of the di-electron pair, while in the Z_{iso} method they are derived from the distribution of a calorimeter isolation variable, as described in Sec. 6.3.

The Z_{iso} method will not be further discussed here, as it is not used in this thesis. However, it is worth noting that the official ATLAS efficiency and SF results provided for other physics analyses are obtained by statistically combining both methods, leading to more robust results in terms of uncertainties. In the low- E_{T} region, below 15 GeV, electron identification efficiencies are measured using $J/\psi \rightarrow e^+e^-$ decays, which provide a clean source of low-energy electrons. Backgrounds from non-prompt J/ψ production, mainly originating from heavy-flavour hadron decays, are suppressed with invariant mass selections around the J/ψ peak and isolation requirements, and their residual contribution is estimated using either template fits to the invariant mass and pseudo-proper lifetime distributions or cut-based methods that enhance the prompt fraction. Although not used in this thesis, the J/ψ method is widely employed in ATLAS to extend the efficiency measurements to this low- E_{T} regime, and is then combined with the Z_{mass} and Z_{iso} results.

The binning used for these measurements is the same as that employed in the tuning of the DNN output, presented in Table 6.3, excluding the low-energy region. The next section will describe in more detail how efficiencies are measured with the Z_{mass} method and the selection applied.

6.4.1.1 Z_{mass} efficiency method

The Z_{mass} method for measuring identification efficiencies in data also requires Monte Carlo simulations. Unless otherwise stated, the results presented here use only Run-2 data from 2018, reprocessed with release R.22, together with a single simulated $Z \rightarrow e^+e^-$ sample as described in Sec. 3.4.1. An identical baseline selection is applied to both collision data and simulations, and consistently used for both the LH and DNN identification menus.

Events are required to pass at least one of the single-electron triggers listed in Table 6.7. For the T&P pair, the tag electron must have transverse energy $E_{\text{T}}^{\text{miss}} > 27$ GeV, lie within the ID acceptance $|\eta| < 2.47$, and be outside the calorimeter crack region ($1.37 < |\eta| < 1.52$). Additional quality requirements are applied, including cuts on impact-parameter-related variables to suppress backgrounds and ensure the tag is a genuine electron. The tag must also satisfy the Tight WP of the corresponding algorithm (DNN or LH) and an isolation requirement $p_{\text{T}}^{\text{topocone}20}/p_{\text{T}} < 0.1$ to ensure track isolation. Finally,

the tag is required to match the object that fired the trigger.

Year	Electron triggers
2018	HLT_e26_lhtight_nod0_ivarloose
	HLT_e60_lhmedium_nod0
	HLT_e140_lhloose_nod0
	HLT_e300_etcut

Table 6.7: Single-electron high-level triggers used in 2018 for this analysis.

The probe electron is initially required to fulfil the same object-quality requirements, but no impact-parameter cuts are applied. A jet veto is imposed to ensure the electron candidate is isolated from any anti- κ_t jet within a given cone. Minimum track-quality requirements are enforced ($n_{\text{Si}} \geq 8$ and $n_{\text{Pixel}} \geq 1$), together with $E_{\text{T}}^{\text{miss}} > 15$ GeV. This *preselected probe* is then tested against the identification working point (DNN or LH) under study.

For the tag-and-probe pair, both electrons must have opposite charge and an invariant mass within $75 < M_{e^+e^-} < 105$ GeV. If multiple valid pairs are found in an event (e.g. interchanging tag and probe), all are considered. Variations in the tag definition or in the invariant-mass window are treated as systematic uncertainties. Each variation is applied individually, and the efficiency difference with respect to the nominal choice is taken as the systematic variation. For example, the nominal isolation requirement $p_{\text{T}}^{\text{topocone20}}/p_{\text{T}} < 0.1$ is varied up and down to < 0.14 and < 0.06 , respectively.

Recalling the definition of the identification efficiency in Eq. 6.8, the denominator is composed of the preselected probes, while the numerator is the subset passing the identification menu under consideration. In practice, even when both electrons from the Z resonance pass the ID requirements, non-negligible background can be present near the mass peak. Therefore, the signal identification efficiency is computed as:

$$\epsilon_{\text{ID}}^{\text{WP}} = \frac{N_{\text{ID}}^{\text{WP}} - N_{\text{bkg},\text{ID}}}{N_{\text{reco}} - N_{\text{bkg,preselected probes}}}, \quad (6.8)$$

where the background contribution in the signal region is estimated and subtracted prior to the calculation. This is precisely where the Z_{mass} method plays its role.

In this method, the invariant mass $m_{e^+e^-}$ in the decay $Z \rightarrow e^+e^-$ is used as a discriminant between signal and background. The nominal mass range $75 < m_{e^+e^-} < 105$ GeV defines the signal region, while broader intervals are used to model and normalise the background. The method relies on template fits to separate the signal contribution from backgrounds, with templates for signal derived from simulated $Z \rightarrow e^+e^-$ events and templates for background obtained from dedicated data control regions.

In earlier implementations, background estimation under the Z peak was performed by normalising the background template in the $m_{e^+e^-}$ sidebands. This approach was limited by biases from asymmetries between the low- and high-mass sidebands and by its strong dependence on simulation. The improved procedure adopted here, schematically shown in Fig. 6.16, reduces the dependence on MC and optimises the subtraction of signal contamination from the background template. The method proceeds iteratively through the following main steps, separately for each (E_T, η) bin:

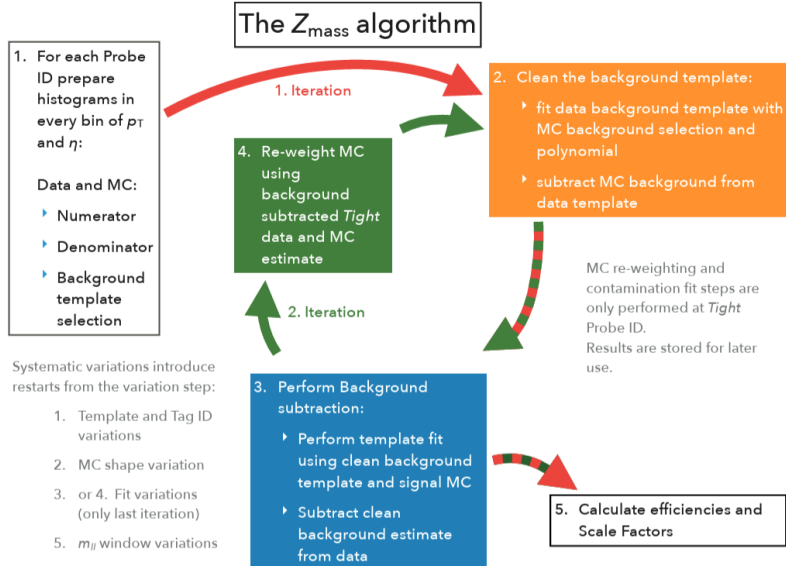


Figure 6.16: Schematic view of the Z_{mass} method for electron identification efficiency calculation. The five steps in which it consists are represented, where after the reweighting step, the second, third and fifth steps are repeated iteratively. Taken from Ref. [195].

- Background control region definition:** a background-enriched sample is selected by requiring the probe to fail a relaxed version of the Loose ID WP (either LH or DNN) and to satisfy a mild calorimeter isolation cut ($E_{\text{T}}^{\text{cone}30}/E_{\text{T}} > 0.12$). Signal templates are built from MC events fulfilling either numerator or denominator requirements, while background templates are taken from this control region in data, with MC providing the estimate of residual signal contamination.
- Background template cleaning:** the residual signal present in the background control region is modelled as a sum of a polynomial background and an MC signal template in the $70 < m_{e^+e^-} < 115$ GeV

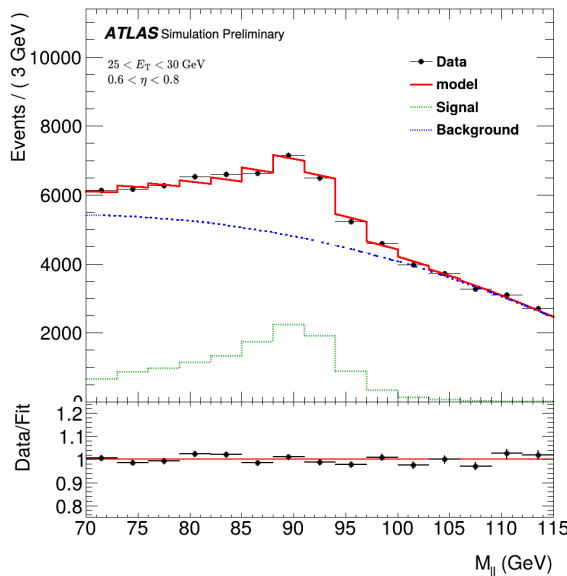


Figure 6.17: Background cleaning procedure in the Z_{mass} method for a representative (E_T , $|\eta|$) bin. The data in the background-enriched control region is fitted with a polynomial function (red curve) describing the background component, together with a MC signal template representing the residual signal contamination. The cleaned background template, obtained after subtracting the signal contribution, is shown in blue.

range. The fitted signal component is subtracted from the data-driven background template to yield a “clean” background shape. Figure 6.17 shows this fit to data, with the background represented as a polynomial plus the signal template derived from MC in the mentioned mass range, yielding in blue the cleaned background template when removing the green (signal) contribution.

3. **Background subtraction in the signal region:** the cleaned background template is normalised to the data in the signal region, in combination with the MC signal template, to extract the background yield. This yield is then subtracted from the total number of events to obtain the signal counts.
4. **MC re-weighting:** before computing the efficiency, a re-weighting procedure is applied to correct for differences in the Z line shape between data and simulation, which may arise from effects such as additional bremsstrahlung in the detector material.
5. **Efficiency and scale factor extraction:** the identification efficiency in data is computed as in Eq. 6.8, replacing N_{bkg} by the background yields from the fit. MC efficiencies are evaluated as the simple ratio of identified probes to all preselected probes. Scale factors are then obtained from the ratio of data to MC efficiencies for each (E_T, η) bin.

As already mentioned, each step of the method introduces potential systematic uncertainties, evaluated by varying key aspects of the procedure, such as the background control region definition, the $m_{e^+e^-}$ fit range, the polynomial order in the signal contamination fit, or the tag electron isolation requirement. This is the procedure applied to measure the identification efficiencies in collision data. For the MC efficiency, Eq. 6.8 reduces to the simple initial ratio, since no background subtraction is required and the measurement can be performed using signal-only events.

The plots in Figure 6.18 show examples of the signal-plus-background template fits obtained with the Z_{mass} method, in the invariant mass distribution of the di-electron pairs. The left panel corresponds to the reconstructed probes, which form the denominator in the efficiency calculation, while the right panel shows the fits for the numerator probes passing the Medium DNN identification working point. These results are extracted from the case of the DNN identification menu, where the two discriminants defined in the previous sections are combined to build the selection. In both cases, the orange line represents the MC signal template, the blue line the estimated background, and the red line the sum of both contributions. The background level is significantly reduced when moving from the inclusive probe selection to the numerator

probes passing the Medium ID, illustrating the increased purity of the sample as the identification requirements become stricter. The lower panels display the Data-to-Expectation ratio, highlighting the good agreement between data and the fitted templates in the mass range considered for the efficiency extraction. A slight degradation of the agreement is observed at very high invariant masses due to the limited statistics in that region, and a small percent-level discrepancy is also visible for the denominator case around the Z peak. The latter is precisely the type of effect that the calculation of scale factors aims to correct.

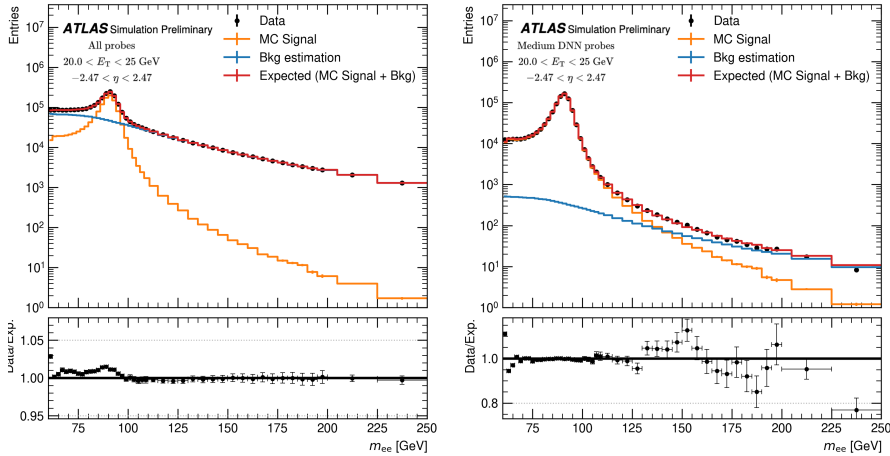


Figure 6.18: Signal and background template fits to the invariant mass $m_{e^+e^-}$ of the di-electron pairs for the Z_{mass} method, shown for the reconstructed probes (left), which constitute the denominator in the efficiency calculation, and for the numerator probes passing the Medium DNN identification (right). The orange line shows the MC signal template, the blue line the estimated background, and the red line the sum of both contributions. The lower panels display the Data-to-Expectation ratio.

There is also the case in which we aim to test the background rejection power of the DNN identification menu in collision data. For this purpose, we employ the same method as before, but the event selection in this case starts from those events that have fired one of the prescaled triggers listed in Table ???. In this case, none of these trigger strings include associated identification requirements, unlike in the signal case, in order to avoid introducing a selection bias.

In this way, we obtain a set fully composed of background electrons, allowing the treatment to follow the same approach as for the MC signal efficiency measurements, without the need to derive templates or subtract signal contam-

Year	Electron triggers (prescaled, <i>etcuts</i>)
2018	HLT_e4_etcut, HLT_e5_etcut, HLT_e9_etcut HLT_e10_etcut_L1EM7, HLT_e14_etcut, HLT_e15_etcut HLT_e15_etcut_L1EM7, HLT_e17_etcut, HLT_e20_etcut_L1EM7 HLT_e20_etcut_L1EM15, HLT_e25_etcut_L1EM15, HLT_e30_etcut_L1EM15 HLT_e40_etcut_L1EM15, HLT_e40_etcut_L1EM9, HLT_e50_etcut HLT_e60_etcut, HLT_e80_etcut, HLT_e100_etcut HLT_e120_etcut, HLT_e140_etcut, HLT_e160_etcut HLT_e180_etcut, HLT_e200_etcut, HLT_e250_etcut HLT_e300_etcut

Table 6.8: Prescaled *etcuts* single-electron triggers used for background-electron selection in 2018, including Level-1 seeds where applicable.

ination. Therefore, in this case, to further reduce potential signal contamination, no tag electron is required, so that the only remaining signal comes from $W \rightarrow e\nu$ decays, which is negligible compared to the large QCD background faking electrons. For the probes, we apply exactly the same requirements as in the previous case, varying only the identification WP. Since no tag electron is required and the invariant mass loses its purpose, the electron counting for estimating the efficiency (or, in this case, the rejection $1/\epsilon$) is performed directly in (E_T, η) bins.

6.4.2 Identification efficiency measurements: DNN versus LH

The results presented in this section summarise the measured identification efficiencies and scale factors (SFs) for the DNN identification menu, as well as comparisons with the LH-based algorithm. Unless otherwise stated, all efficiencies are evaluated for $E_T > 15$ GeV and are shown for the three working points defined for the DNN, both in data and MC simulation. It is also worth noting that all MC efficiency measurements include the previously discussed shower-shape corrections.

Figure 6.19 displays the inclusive signal identification efficiency in data and MC, together with the corresponding SFs, for the three DNN working points without applying the charge-flip discriminant. The same selection is repeated using the LH identification menu, enabling a direct performance comparison in the case of the Medium WP. This comparison is shown separately in selected (E_T, η) bins in order to highlight differences in specific kinematic regions.

As illustrated in Figure 6.19a, the efficiency is typically reduced in the central barrel region ($|\eta| \sim 0$) and in the transition region between barrel and end-cap ($1.37 < |\eta| < 1.52$). A general decrease in efficiency is also observed towards the end-cap, at large $|\eta|$ values. When studied as a function of E_T , the identification efficiency is lower at small transverse energies. This behaviour

originates from a larger background contamination in this regime, where the estimation of efficiencies with the Z_{mass} method becomes more challenging, unlike at higher energies.

Concerning the SFs, the values for the three DNN working points remain close to unity, as expected given the corrections applied to the MC samples. The largest deviations are found for the Tight WP, which is reasonable since the stricter thresholds applied on the discriminant amplify potential mismodellings with respect to data and therefore affect the efficiency calculation more strongly. In general, the SFs tend to be closer to unity in the barrel region. A small asymmetry is also observed as a function of η , affecting all three WPs. Since the same feature is present in the LH measurements shown in Figures ??, it cannot be attributed to the DNN algorithm itself.

A direct comparison of the signal identification efficiency between both algorithms is shown in Figure ?? as a function of η for $25 < E_T < 30$ GeV, and in Figure ?? as a function of E_T for $0.1 < \eta < 0.6$. In both cases, the obtained values are very similar, which is expected since both menus were tuned to match the same target identification efficiencies, as described in Section 6.2.2.7.

In addition, Figure 6.20 presents the efficiency as a function of the average number of interactions per bunch crossing, μ , for all three DNN working points, along with a direct comparison between DNN and LH for the Medium and Loose ones. For the three DNN working points, a decreasing trend is observed as pile-up increases, with the Tight WP being the most sensitive to these variations. Nevertheless, the comparison with LH in Figures ?? shows a similar trend, with the LH algorithm exhibiting slightly more stability. This behaviour can be explained by the fact that the LH menu applies explicit pile-up dependent corrections, whereas the DNN, by construction, has no direct notion of pile-up.

It is not only necessary to draw conclusions from the performance on signal electrons, which are used for the tuning, but the background rejection power must also be investigated. Figure ?? shows the background acceptance, simply defined as the number of background electrons passing each working point. This performance is compared between the combined DNN ID+CF menu and the LH+ECIDs, evaluated on the JF17 MC background sample, which contains a mixture of QCD jet flavours as described in Section 3.4.1.

The results are shown as a function of η in two E_T bins, one at lower energies and one at higher energies, illustrating the performance across part of the kinematic range. A clear improvement of the DNN algorithm over the LH is observed across the full η range, as it allows significantly fewer background electrons to pass. This is also evident in the lower pads where the ratio between both methods is displayed. At higher E_T , the performance of

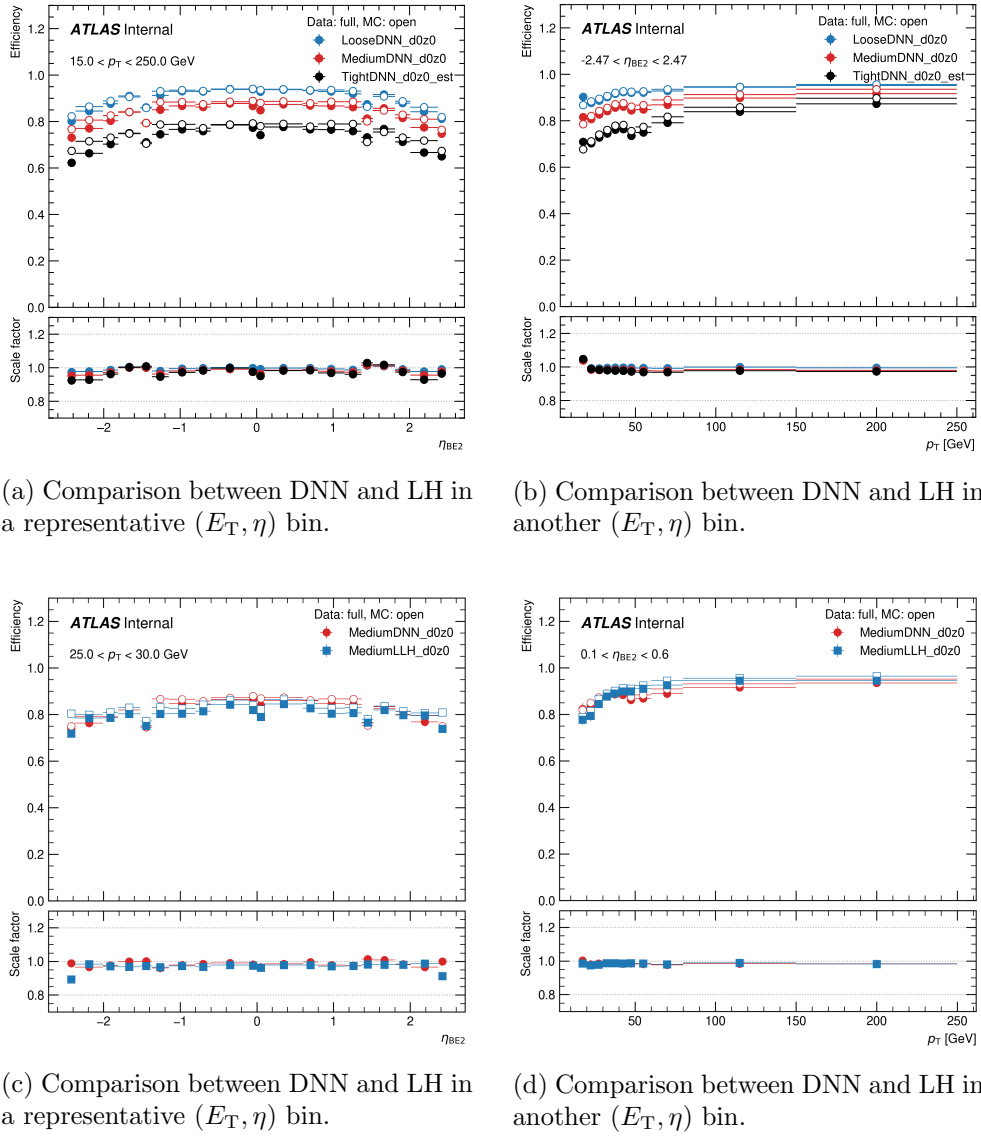
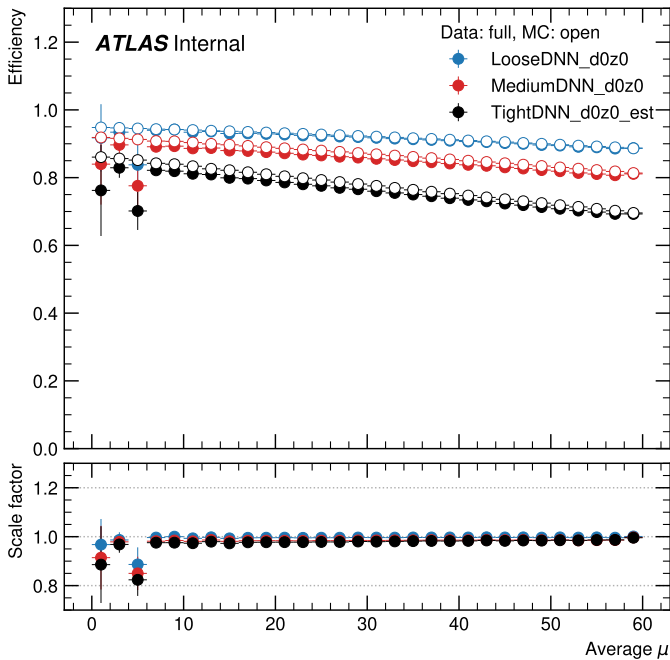
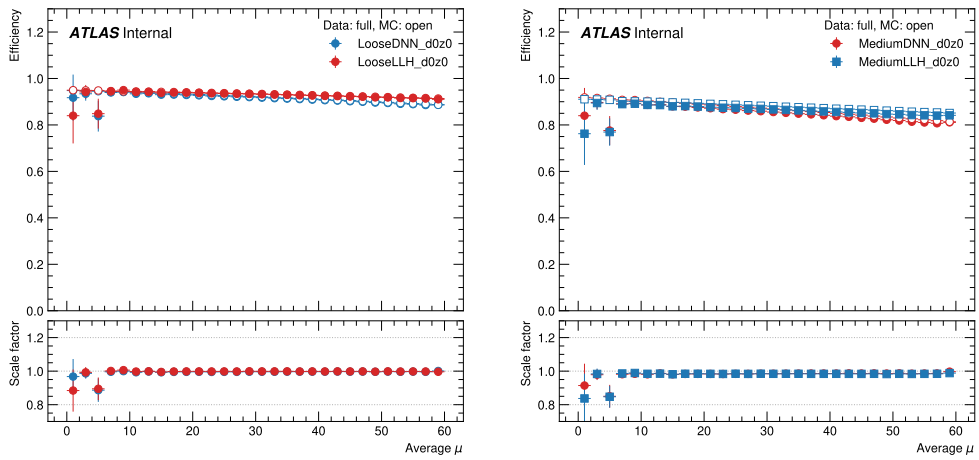


Figure 6.19: Signal identification efficiencies in data and MC, together with SFs, for the DNN menu without CF cuts. The top panel shows the inclusive efficiencies for the three working points, while the bottom panels illustrate the comparison with the LH algorithm in two representative (E_T, η) bins.



(a) Inclusive signal identification efficiency in data and MC, together with SFs, for the three DNN working points without CF cuts.

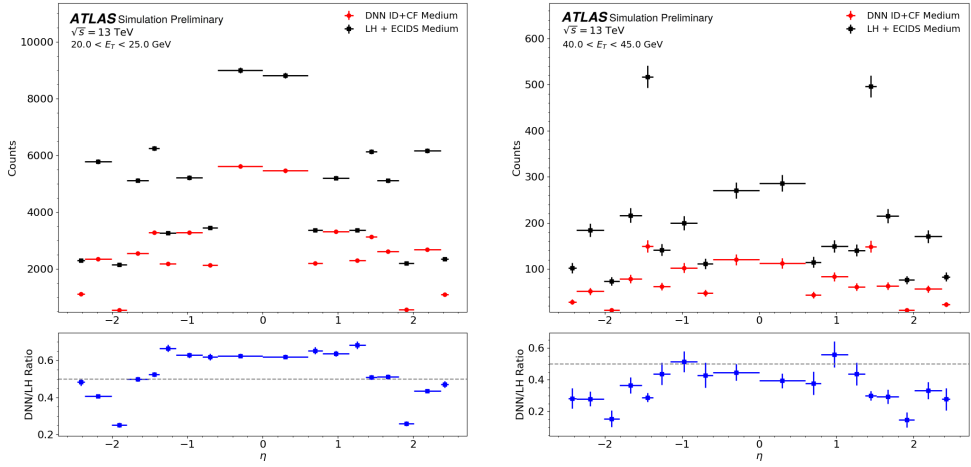


(b) Comparison between DNN and LH in a representative (E_T, η) bin.

(c) Comparison between DNN and LH in another (E_T, η) bin.

Figure 6.20: Signal identification efficiency as a function of μ for the three DNN working points without CF cuts. A comparison between DNN and LH is also shown for the Medium working point.

LH is particularly degraded in the crack region, highlighting the challenges of electron identification in this part of the detector.



(a) Comparison between DNN and LH in a representative (E_T, η) bin.

(b) Comparison between DNN and LH in another (E_T, η) bin.

However, final conclusions on the background performance cannot be drawn by looking at a single MC sample alone. For this reason, it is necessary to also examine real collision data. A complementary validation is performed on same-sign $Z \rightarrow e^+e^-$ events in data, which are largely populated by CF electrons. Figure 6.22 shows the invariant mass distribution around the Z -boson peak, requiring a tag and a probe electron passing the Medium WP of the identification menus displayed in different coloured lines. The identification menu providing the best rejection of CF electrons is the one yielding the lowest curve.

It can be observed that the DNN menu, when only applying ID cuts (black), allows more CF electrons to pass, which is expected since in the original \mathcal{D}_{el} (defined in Eq. 6.5), this class is treated as signal. However, when comparing the LH menu with the dedicated ECIDS method, and the DNN combined with cuts on both \mathcal{D}_{el} and \mathcal{D}_{CF} , not only is the same rejection recovered but it is surpassed, without the need to train a dedicated algorithm. This improvement is mainly due to the inclusion of new variables in the DNN training. A reduction of about 16% in CF electrons is achieved within the [75, 105] GeV interval around the Z -boson mass.

Finally, background rejection values can also be computed directly in collision data as described previously. However, these results are not shown here. Instead, since small variations are observed not only in the background rejection but also in the signal identification performance, we present in Figure 6.23

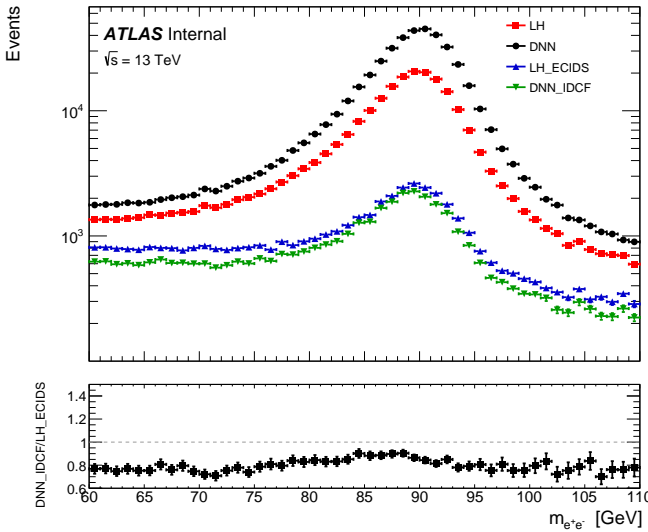


Figure 6.22: Inclusive background efficiency in same-sign $Z \rightarrow e^+e^-$ events for DNN, LH, DNN+CF, and LH+ECIDs. Lower curves indicate better charge-misidentification rejection.

an estimation of the significance for the DNN (ID-only) and LH menus, computed in data as

$$\hat{\sigma} = S_{\text{eff}} \times \sqrt{\text{Bkg}_{\text{rej}}}, \quad (6.9)$$

for each working point of the DNN and LH menus. This metric, derived from the combination of signal efficiency and background rejection, provides a direct figure of merit for the expected sensitivity improvement when moving from LH to the DNN approach.

From these plots, both for the inclusive case in the top row and for the selected η and E_T bins, the overall improvement of the DNN menu over the LH approach is evident. As particularly observed in the background rejection performance, the LH algorithm exhibits a clear degradation in the crack region, which is not present for the DNN. In this case, specific treatments were applied during training, such as masking problematic variables in that region in order to avoid mis-modelling effects.

In addition, from the bottom ratio plots it can be seen that the improvement follows an approximately consistent trend. For intermediate to lower E_T values, the DNN shows its best relative performance, reaching a peak around $E_T = 30$ GeV. Overall, these results indicate that the DNN menu provides a more robust performance particularly in regions with larger background con-

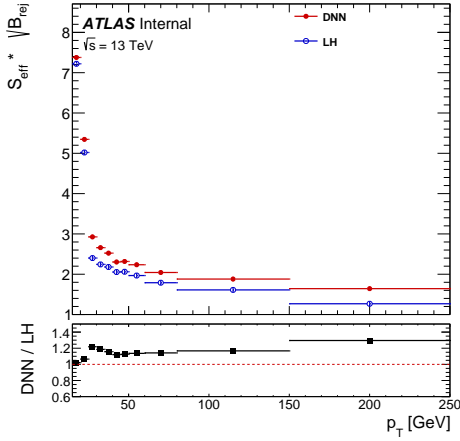
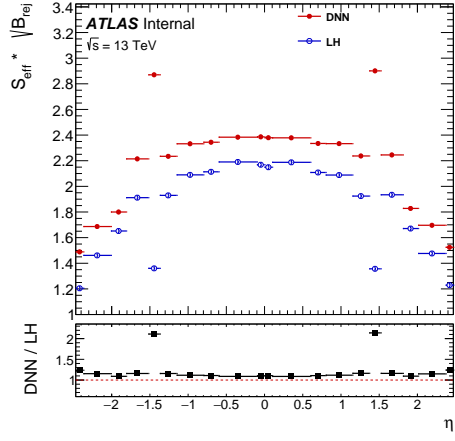
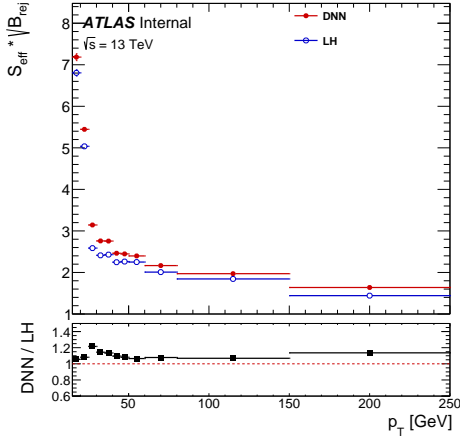
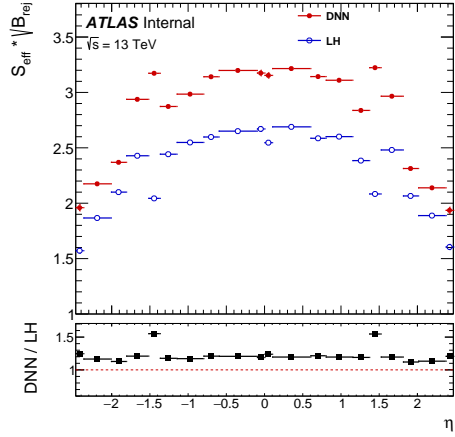
(a) Inclusive significance vs $|\eta|$.(b) Inclusive significance vs E_T .(c) Significance vs E_T , $|\eta| \in [1.37, 1.52]$.(d) Significance vs $|\eta|$, $E_T \in [25, 35]$ GeV.

Figure 6.23: Significance estimator $S_{\text{eff}} \times \sqrt{B_{\text{kg, rej}}}$ computed in data for the DNN and LH identification menus. Top: inclusive measurements versus $|\eta|$ (a) and E_T (b) for the three working points. Bottom: projections in fixed kinematic regions, shown versus E_T at fixed $|\eta|$ (c) and versus $|\eta|$ at fixed E_T (d).

tribution.

Chapter 7

Results

Place your results here.

Chapter 8

Conclusion

Place your conclusion here.

References

- [1] D. Griffiths, *Introduction to Elementary Particles*, John Wiley and Sons, New York, USA (1987). (cit. on p. 3)
- [2] J. Ellis, *Higgs physics*, , 2013. (cit. on p. 3)
- [3] A. Pich, *The standard model of electroweak interactions*, , 2012. (cit. on p. 3)
- [4] A. Djouadi, *The anatomy of electroweak symmetry breaking*, *Physics Reports* **457** (2008) 1–216. (cit. on p. 3)
- [5] C.N. Yang and R.L. Mills, *Conservation of isotopic spin and isotopic gauge invariance*, *Phys. Rev.* **96** (1954) 191. (cit. on p. 3)
- [6] S. Bilenky, *Neutrino oscillations: From a historical perspective to the present status*, *Nuclear Physics B* **908** (2016) 2. (cit. on p. 4)
- [7] T. Ohlsson, *Special issue on “neutrino oscillations: Celebrating the nobel prize in physics 2015” in nuclear physics b*, *Nuclear Physics B* **908** (2016) 1. (cit. on p. 4)
- [8] PARTICLE DATA GROUP Collaboration, *Review of particle physics*, *Phys. Rev. D* **110** (2024) 030001. (cit. on p. 5, 18, 21, and 75)
- [9] V.N. Gribov and L.N. Lipatov, *Deep inelastic ep scattering in perturbation theory*, *Sov. J. Nucl. Phys.* **15** (1972) 438. (cit. on p. 7)
- [10] G. Altarelli and G. Parisi, *Asymptotic freedom in parton language*, *Nuclear Physics B* **126** (1977) 298. (cit. on p. 7)
- [11] Y.L. Dokshitzer, *Calculation of the Structure Functions for Deep Inelastic Scattering and e+ e- Annihilation by Perturbation Theory in Quantum Chromodynamics.*, *Sov. Phys. JETP* **46** (1977) 641. (cit. on p. 7)
- [12] A.D. Martin, W.J. Stirling, R.S. Thorne and G. Watt, *Parton distributions for the lhc*, *The European Physical Journal C* **63** (2009) 189–285. (cit. on p. 7 and 62)
- [13] J.C. Collins and D.E. Soper, *The theorems of perturbative qcd*, *Annual Review of Nuclear and Particle Science* **37** (1987) 383. (cit. on p. 8)
- [14] J.C. Collins, D.E. Soper and G. Sterman, *Factorization of hard processes in qcd*, , 2004. (cit. on p. 8)
- [15] S.L. Glashow, *Partial-symmetries of weak interactions*, *Nuclear Physics* **22** (1961) 579. (cit. on p. 9)
- [16] S. Weinberg, *A model of leptons*, *Phys. Rev. Lett.* **19** (1967) 1264. (cit. on p. 9)
- [17] A. Salam, *Weak and electromagnetic interactions*, in *Selected Papers of Abdus Salam*, pp. 244–254 DOI
[arXiv:https://www.worldscientific.com/doi/pdf/10.1142/9789812795915_0034]. (cit. on p. 9)

- [18] F. Englert and R. Brout, *Broken Symmetry and the Mass of Gauge Vector Mesons*, *Phys. Rev. Lett.* **13** (1964) 321. (cit. on p. 10)
- [19] P.W. Higgs, *Spontaneous Symmetry Breakdown without Massless Bosons*, *Phys. Rev.* **145** (1966) 1156. (cit. on p. 10)
- [20] ATLAS, CMS Collaboration, *Measurements of the Higgs boson production and decay rates and constraints on its couplings from a combined ATLAS and CMS analysis of the LHC pp collision data at $\sqrt{s} = 7$ and 8 TeV*, *JHEP* **08** (2016) 045 [arXiv:1606.02266]. (cit. on p. 12)
- [21] M.E. Peskin and D.V. Schroeder, *An Introduction to quantum field theory*, Addison-Wesley, Reading, USA (1995), 10.1201/9780429503559. (cit. on p. 12)
- [22] ATLAS Collaboration, *Summary plots from the ATLAS Standard Model physics group*, , <https://atlas.web.cern.ch/Atlas/GROUPS/PHYSICS/CombinedSummaryPlots/SM/>, 2019. Accessed: Jun. 12, 2025. (cit. on p. 14)
- [23] D. Clowe, M. Bradač, A.H. Gonzalez, M. Markevitch, S.W. Randall, C. Jones et al., *A direct empirical proof of the existence of dark matter*, *The Astrophysical Journal* **648** (2006) L109–L113. (cit. on p. 14)
- [24] N. Aghanim, Y. Akrami, M. Ashdown, J. Aumont, C. Baccigalupi, M. Ballardini et al., *Planck2018 results: Vi. cosmological parameters*, *Astronomy amp; Astrophysics* **641** (2020) A6. (cit. on p. 14)
- [25] PARTICLE DATA GROUP Collaboration, *Review of particle physics*, *Phys. Rev. D* **98** (2018) 030001. (cit. on p. 15)
- [26] M. Kobayashi and T. Maskawa, *CP-Violation in the Renormalizable Theory of Weak Interaction*, *Progress of Theoretical Physics* **49** (1973) 652. (cit. on p. 16)
- [27] CDF Collaboration, *Observation of top quark production in $\bar{p}p$ collisions with the collider detector at fermilab*, *Phys. Rev. Lett.* **74** (1995) 2626 [arXiv:hep-ex/9503002]. (cit. on p. 16)
- [28] D0 Collaboration, *Observation of the top quark*, *Phys. Rev. Lett.* **74** (1995) 2632 [arXiv:hep-ex/9503003]. (cit. on p. 16)
- [29] K. Lannon, F. Margaroli and C. Neu, *Measurements of the production, decay and properties of the top quark: a review*, *The European Physical Journal C* **72** (2012) . (cit. on p. 18)
- [30] ATLAS Collaboration, *Observation of a new particle in the search for the Standard Model Higgs boson with the ATLAS detector at the LHC*, *Phys. Lett. B* **716** (2012) 1 [arXiv:1207.7214]. (cit. on p. 18 and 32)
- [31] CMS Collaboration, *Observation of a New Boson at a Mass of 125 GeV with the CMS Experiment at the LHC*, *Phys. Lett. B* **716** (2012) 30 [arXiv:1207.7235]. (cit. on p. 18 and 32)
- [32] ATLAS Collaboration, *A detailed map of Higgs boson interactions by the ATLAS experiment ten years after the discovery*, *Nature* **607** (2022) 52 [arXiv:2207.00092]. (cit. on p. 19, 21, 24, 25, 28, and 29)
- [33] CERN, *Cern yellow reports: Monographs, vol 2 (2017): Handbook of lhc higgs cross sections: 4. deciphering the nature of the higgs sector*, , 2017. 10.23731/CYRM-2017-002. (cit. on p. 23)
- [34] C. Englert, A. Freitas, M.M. Mühlleitner, T. Plehn, M. Rauch, M. Spira et al., *Precision Measurements of Higgs Couplings: Implications for New Physics Scales*, *J. Phys. G* **41** (2014) 113001 [arXiv:1403.7191]. (cit. on p. 23)

- [35] B.A. Dobrescu and C.T. Hill, *Electroweak symmetry breaking via top condensation seesaw*, *Phys. Rev. Lett.* **81** (1998) 2634 [arXiv:[hep-ph/9712319](#)]. (cit. on p. 23)
- [36] R.S. Chivukula, B.A. Dobrescu, H. Georgi and C.T. Hill, *Top Quark Seesaw Theory of Electroweak Symmetry Breaking*, *Phys. Rev. D* **59** (1999) 075003 [arXiv:[hep-ph/9809470](#)]. (cit. on p. 23)
- [37] D. Delepine, J.M. Gerard and R. Gonzalez Felipe, *Is the standard Higgs scalar elementary?*, *Phys. Lett. B* **372** (1996) 271 [arXiv:[hep-ph/9512339](#)]. (cit. on p. 23)
- [38] W. Bernreuther, *CP violation and baryogenesis*, *Lect. Notes Phys.* **591** (2002) 237 [arXiv:[hep-ph/0205279](#)]. (cit. on p. 23)
- [39] J. Brod, U. Haisch and J. Zupan, *Constraints on CP-violating Higgs couplings to the third generation*, *JHEP* **11** (2013) 180 [arXiv:[1310.1385](#)]. (cit. on p. 23)
- [40] D. Buttazzo, G. Degrassi, P.P. Giardino, G.F. Giudice, F. Sala, A. Salvio et al., *Investigating the near-criticality of the Higgs boson*, *JHEP* **12** (2013) 089 [arXiv:[1307.3536](#)]. (cit. on p. 23)
- [41] G. Degrassi, P.P. Giardino, F. Maltoni and D. Pagani, *Probing the Higgs self coupling via single Higgs production at the LHC*, *JHEP* **12** (2016) 080 [arXiv:[1607.04251](#)]. (cit. on p. 23)
- [42] J.N. Ng and P. Zakarauskas, *A QCD Parton Calculation of Conjoined Production of Higgs Bosons and Heavy Flavors in $p\bar{p}$ Collision*, *Phys. Rev. D* **29** (1984) 876. (cit. on p. 23)
- [43] Z. Kunszt, *Associated Production of Heavy Higgs Boson with Top Quarks*, *Nucl. Phys. B* **247** (1984) 339. (cit. on p. 23)
- [44] W. Beenakker, S. Dittmaier, M. Kramer, B. Plumper, M. Spira and P.M. Zerwas, *Higgs radiation off top quarks at the Tevatron and the LHC*, *Phys. Rev. Lett.* **87** (2001) 201805 [arXiv:[hep-ph/0107081](#)]. (cit. on p. 23)
- [45] ATLAS Collaboration, *Observation of Higgs boson production in association with a top quark pair at the LHC with the ATLAS detector*, *Phys. Lett. B* **784** (2018) 173 [arXiv:[1806.00425](#)]. (cit. on p. 23)
- [46] CMS Collaboration, *Observation of $t\bar{t}H$ production*, *Phys. Rev. Lett.* **120** (2018) 231801 [arXiv:[1804.02610](#)]. (cit. on p. 23)
- [47] CMS Collaboration, *A portrait of the Higgs boson by the CMS experiment ten years after the discovery.*, *Nature* **607** (2022) 60 [arXiv:[2207.00043](#)]. (cit. on p. 24)
- [48] *Evidence for the higgs boson decay to a z boson and a photon at the lhc*, *Physical Review Letters* **132** (2024) . (cit. on p. 24)
- [49] *Evidence for higgs boson decay to a pair of muons*, *Journal of High Energy Physics* **2021** (2021) . (cit. on p. 24)
- [50] J.R. Andersen et al., *Les houches 2015: Physics at tev colliders standard model working group report*, , 2016. (cit. on p. 25 and 27)
- [51] N. Berger et al., *Simplified Template Cross Sections - Stage 1.1*, arXiv:[1906.02754](#). (cit. on p. 26)
- [52] L. Evans and P. Bryant, *Lhc machine*, *Journal of Instrumentation* **3** (2008) S08001. (cit. on p. 32)
- [53] ATLAS Collaboration, *The atlas experiment at the cern large hadron collider*, *Journal of Instrumentation* **3** (2008) S08003. (cit. on p. 32 and 37)
- [54] CMS Collaboration, *The cms experiment at the cern lhc*, *Journal of Instrumentation* **3** (2008) S08004. (cit. on p. 32)

- [55] ALICE Collaboration, *The alice experiment at the cern lhc*, *Journal of Instrumentation* **3** (2008) S08002. (cit. on p. 32)
- [56] LHCb Collaboration, *The lhcb detector at the lhc*, *Journal of Instrumentation* **3** (2008) S08005. (cit. on p. 32)
- [57] E. Lopienska, *The CERN accelerator complex, layout in 2022. Complexe des accélérateurs du CERN en janvier 2022*, . (cit. on p. 33)
- [58] ATLAS Collaboration, *Luminosity determination in pp collisions at $\sqrt{s} = 13$ tev using the atlas detector at the lhc*, *The European Physical Journal C* **83** (2023) . (cit. on p. 34)
- [59] ATLAS Collaboration, *Atlas data quality operations and performance for 2015–2018 data-taking*, *Journal of Instrumentation* **15** (2020) P04003. (cit. on p. 34)
- [60] ATLAS Collaboration, *Public ATLAS Luminosity Results for Run-3 of the LHC*, Available at <https://twiki.cern.ch/twiki/bin/view/AtlasPublic/LuminosityPublicResultsRun3>, 2025. (cit. on p. 35)
- [61] ATLAS Collaboration, *Public ATLAS Luminosity Results for Run-2 of the LHC*, Available at <https://twiki.cern.ch/twiki/bin/view/AtlasPublic/LuminosityPublicResultsRun2>, 2022. (cit. on p. 35 and 36)
- [62] ATLAS Collaboration, *Luminosity determination in pp collisions at $\sqrt{s} = 8$ tev using the atlas detector at the lhc*, *The European Physical Journal C* **76** (2016) . (cit. on p. 35)
- [63] ATLAS Collaboration, *Primary Vertex identification using deep learning in ATLAS*, (cit. on p. 35) , CERN, Geneva (2023).
- [64] ATLAS Collaboration, *Constituent-level pile-up mitigation techniques in ATLAS*, . (cit. on p. 35)
- [65] G. Soyez, *Pileup mitigation at the lhc: A theorist's view*, *Physics Reports* **803** (2019) 1–158. (cit. on p. 35)
- [66] G. Apollinari, O. Brüning, T. Nakamoto and L. Rossi, *High luminosity large hadron collider hl-lhc*, , 2015. 10.5170/CERN-2015-005.1. (cit. on p. 36)
- [67] F.J. Mangiarotti, S. Ferradas Troitino, M. Duda, M. Bajko, L. Bottura, V. Desbiolles et al., *Powering Performance and Endurance Beyond Design Limits of HL-LHC Low-Beta Quadrupole Model Magnets*, *IEEE Trans. Appl. Supercond.* **31** (2021) 4000805. (cit. on p. 36)
- [68] ATLAS Collaboration, *ATLAS: Detector and physics performance technical design report. Volume 1*, . (cit. on p. 37)
- [69] R.M. Bianchi and A. Collaboration, *ATLAS experiment schematic or layout illustration*, General Photo, 2022. (cit. on p. 38, 49, 68, and 69)
- [70] G. Chatham Strong, *On the impact of selected modern deep-learning techniques to the performance and celerity of classification models in an experimental high-energy physics use case*, *Machine Learning: Science and Technology* **1** (2020) 045006. (cit. on p. 40)
- [71] ATLAS Collaboration, *ATLAS inner detector: Technical Design Report*, 1, Technical design report. ATLAS, CERN, Geneva (1997). (cit. on p. 39)

- [72] ATLAS Collaboration, S. Haywood, L. Rossi, R. Nickerson and A. Romanouk, *ATLAS inner detector: Technical Design Report, 2*, Technical design report. ATLAS, CERN, Geneva (1997). (cit. on p. 39)
- [73] A. Collaboration, *Experiment Briefing: Keeping the ATLAS Inner Detector in perfect alignment*, General Photo, 2020. (cit. on p. 41 and 43)
- [74] ATLAS Collaboration, *ATLAS Insertable B-Layer Technical Design Report*, (cit. on p. 41)
(2010).
- [75] ATLAS Collaboration, *The atlas experiment at the cern large hadron collider: a description of the detector configuration for run 3*, *Journal of Instrumentation* **19** (2024) P05063. (cit. on p. 42)
- [76] C. ATLAS, *Letter of Intent for the Phase-II Upgrade of the ATLAS Experiment*, (cit. on p. 43)
, CERN, Geneva (2012).
- [77] ATLAS Collaboration, *ATLAS liquid-argon calorimeter: Technical Design Report*, Technical design report. ATLAS, CERN, Geneva (1996), [10.17181/CERN.FWRW.FOOQ](https://cds.cern.ch/record/1017181). (cit. on p. 43)
- [78] ATLAS Collaboration, *ATLAS tile calorimeter: Technical Design Report*, Technical design report. ATLAS, CERN, Geneva (1996), [10.17181/CERN.JRBJ.7028](https://cds.cern.ch/record/1017181). (cit. on p. 43)
- [79] ATLAS Collaboration, *Public Liquid-Argon Calorimeter PLots on Detector Status*, Available at <https://twiki.cern.ch/twiki/bin/view/AtlasPublic/LArCaloPublicResultsDetStatus>, 2021. (cit. on p. 45)
- [80] P. Gessinger, H. Grasland, H. Gray, M. Kiehn, F. Klimpel, R. Langenberg et al., *The Acts project: track reconstruction software for HL-LHC and beyond*, *EPJ Web Conf.* **245** (2020) 10003. (cit. on p. 47)
- [81] ATLAS Collaboration, *ATLAS muon spectrometer: Technical Design Report*, Technical design report. ATLAS, CERN, Geneva (1997). (cit. on p. 48)
- [82] B. Stelzer, *The New Small Wheel Upgrade Project of the ATLAS Experiment*, (cit. on p. 48)
, CERN, Geneva (2016), DOI.
- [83] P. Jenni and M. Nessi, *ATLAS Forward Detectors for Luminosity Measurement and Monitoring*, (cit. on p. 49)
, CERN, Geneva (2004).
- [84] S.A. Khalek, B. Allongue, F. Anghinolfi, P. Barrillon, G. Blanchot, S. Blin-Bondil et al., *The alfa roman pot detectors of atlas*, *Journal of Instrumentation* **11** (2016) P11013–P11013. (cit. on p. 50)
- [85] L. Adamczyk et al., *Technical Design Report for the ATLAS Forward Proton Detector*, . (cit. on p. 50)
- [86] ATLAS Collaboration, *Zero Degree Calorimeters for ATLAS*, (cit. on p. 50)
, CERN, Geneva (2007).
- [87] T.A. collaboration, *Operation of the atlas trigger system in run 2*, *Journal of Instrumentation* **15** (2020) P10004. (cit. on p. 50)

- [88] ATLAS Collaboration, *Approved Plots for the Data Acquisition (DAQ) in Run 2*, Available at <https://twiki.cern.ch/twiki/bin/view/AtlasPublic/ApprovedPlotsDAQ>, 2020. (cit. on p. 51)
- [89] S. Schlenker, S. Arfaoui, S. Kersten, D. Hirschbuehl, H. Braun, A. Poblaquev et al., *The ATLAS Detector Control System*, *Conf. Proc. C111010* (2011) MOBAUST02. (cit. on p. 53)
- [90] I. Bird, P. Buncic, F. Carminati, M. Cattaneo, P. Clarke, I. Fisk et al., *Update of the Computing Models of the WLCG and the LHC Experiments*, (cit. on p. 53) (2014).
- [91] A. Buckley, J. Butterworth, S. Gieseke, D. Grellscheid, S. Höche, H. Hoeth et al., *General-purpose event generators for lhc physics*, *Physics Reports* **504** (2011) 145. (cit. on p. 55)
- [92] T. Gleisberg, S. Höche, F. Krauss, M. Schönher, S. Schumann, F. Siegert et al., *Event generation with sherpa 1.1*, *Journal of High Energy Physics* **2009** (2009) 007–007. (cit. on p. 56)
- [93] G.C. Fox and S. Wolfram, *A model for parton showers in qcd*, *Nuclear Physics B* **168** (1980) 285. (cit. on p. 57)
- [94] M.L. Mangano, M. Moretti and R. Pittau, *Multijet matrix elements and shower evolution in hadronic collisions: Wbb+n-jets as a case study*, *Nuclear Physics B* **632** (2002) 343. (cit. on p. 57)
- [95] S. Catani, F. Krauss, B.R. Webber and R. Kuhn, *Qcd matrix elements + parton showers*, *Journal of High Energy Physics* **2001** (2001) 063–063. (cit. on p. 57)
- [96] R. Frederix and S. Frixione, *Merging meets matching in mc@nlo*, *Journal of High Energy Physics* **2012** (2012) . (cit. on p. 57)
- [97] B. Andersson, G. Gustafson, G. Ingelman and T. Sjöstrand, *Parton fragmentation and string dynamics*, *Physics Reports* **97** (1983) 31. (cit. on p. 57)
- [98] J.-C. Winter, F. Krauss and G. Soff, *A modified cluster-hadronisation model*, *The European Physical Journal C* **36** (2004) 381–395. (cit. on p. 57)
- [99] S. Agostinelli, J. Allison, K. Amako, J. Apostolakis, H. Araujo, P. Arce et al., *Geant4—a simulation toolkit*, *Nuclear Instruments and Methods in Physics Research Section A: Accelerators, Spectrometers, Detectors and Associated Equipment* **506** (2003) 250. (cit. on p. 58)
- [100] K. Edmonds, S. Fleischmann, T. Lenz, C. Magass, J. Mechnich and A. Salzburger, *The Fast ATLAS Track Simulation (FATRAS)*, (cit. on p. 58) , CERN, Geneva (2008).
- [101] C. ATLAS, M. Beckingham, M. Duehrssen, E. Schmidt, M. Shapiro, M. Venturi et al., *The simulation principle and performance of the ATLAS fast calorimeter simulation FastCaloSim*, (cit. on p. 58) , CERN, Geneva (2010).
- [102] T. Sjöstrand, S. Ask, J.R. Christiansen, R. Corke, N. Desai, P. Ilten et al., *An introduction to pythia 8.2*, *Computer Physics Communications* **191** (2015) 159. (cit. on p. 59)
- [103] M. Bähr, S. Gieseke, M.A. Gigg, D. Grellscheid, K. Hamilton, O. Latunde-Dada et al., *Herwig++ physics and manual*, *The European Physical Journal C* **58** (2008) 639–707. (cit. on p. 59)

- [104] E. Bothmann, G. Singh Chahal, S. Höche, J. Krause, F. Krauss, S. Kuttimalai et al., *Event generation with sherpa 2.2*, *SciPost Physics* **7** (2019) . (cit. on p. 59)
- [105] J. Alwall, R. Frederix, S. Frixione, V. Hirschi, F. Maltoni, O. Mattelaer et al., *The automated computation of tree-level and next-to-leading order differential cross sections, and their matching to parton shower simulations*, *Journal of High Energy Physics* **2014** (2014) . (cit. on p. 59)
- [106] S. Frixione, G. Ridolfi and P. Nason, *A positive-weight next-to-leading-order monte carlo for heavy flavour hadroproduction*, *Journal of High Energy Physics* **2007** (2007) 126–126. (cit. on p. 60)
- [107] N. Davidson, T. Przedzinski and Z. Was, *Photos interface in c++; technical and physics documentation*, , 2015. (cit. on p. 60)
- [108] P. Golonka and Z. Was, *Photos monte carlo: a precision tool for qed correctionsin z and w decays*, *The European Physical Journal C* **45** (2006) 97–107. (cit. on p. 60)
- [109] D.J. Lange, *The evtgen particle decay simulation package*, *Nuclear Instruments and Methods in Physics Research Section A: Accelerators, Spectrometers, Detectors and Associated Equipment* **462** (2001) 152. (cit. on p. 60 and 62)
- [110] ATLAS Pythia 8 tunes to 7 TeV data, (cit. on p. 61 and 62) , CERN, Geneva (2014).
- [111] ATLAS Collaboration, *Studies on top-quark Monte Carlo modelling for Top2016*, (cit. on p. 61) , CERN, Geneva (2016).
- [112] C. Anastasiou, C. Duhr, F. Dulat, F. Herzog and B. Mistlberger, *Higgs boson gluon-fusion production in qcd at three loops*, *Phys. Rev. Lett.* **114** (2015) 212001. (cit. on p. 61)
- [113] C. Anastasiou, C. Duhr, F. Dulat, E. Furlan, T. Gehrmann, F. Herzog et al., *High precision determination of the gluon fusion higgs boson cross-section at the lhc*, , 2016. (cit. on p. 61)
- [114] R.V. Harlander and K.J. Ozeren, *Finite top mass effects for hadronic higgs production at next-to-next-to-leading order*, *Journal of High Energy Physics* **2009** (2009) 088–088. (cit. on p. 61)
- [115] R.V. Harlander and K.J. Ozeren, *Top mass effects in higgs production at next-to-next-to-leading order qcd: Virtual corrections*, *Physics Letters B* **679** (2009) 467–472. (cit. on p. 61)
- [116] R.V. Harlander, H. Mantler, S. Marzani and K.J. Ozeren, *Higgs production in gluon fusion at next-to-next-to-leading order qcd for finite top mass*, *The European Physical Journal C* **66** (2010) 359–372. (cit. on p. 61)
- [117] A. Pak, M. Rogal and M. Steinhauser, *Finite top quark mass effects in nnlo higgs boson production at lhc*, *Journal of High Energy Physics* **2010** (2010) . (cit. on p. 61)
- [118] S. Actis, G. Passarino, C. Sturm and S. Uccirati, *Nlo electroweak corrections to higgs boson production at hadron colliders*, *Physics Letters B* **670** (2008) 12–17. (cit. on p. 61)
- [119] M. Bonetti, K. Melnikov and L. Tancredi, *Higher order corrections to mixed qcd-ew contributions to higgs boson production in gluon fusion*, *Physical Review D* **97** (2018) . (cit. on p. 61)
- [120] J. Butterworth, S. Carrazza, A. Cooper-Sarkar, A.D. Roeck, J. Feltesse, S. Forte et al., *Pdf4lhc recommendations for lhc run ii*, *Journal of Physics G: Nuclear and Particle Physics* **43** (2016) 023001. (cit. on p. 61)

- [121] P. Bolzoni, F. Maltoni, S.-O. Moch and M. Zaro, *Higgs boson production via vector-boson fusion at next-to-next-to-leading order in qcd*, *Physical Review Letters* **105** (2010) . (cit. on p. 62)
- [122] M. Ciccolini, D. A. and D. S., *Electroweak and qcd corrections to higgs production via vector-boson fusion at the cern lhc*, *Physical Review D* **77** (2008) . (cit. on p. 62)
- [123] M.L. Ciccolini, S. Dittmaier and M. Krämer, *Electroweak radiative corrections to associatedwhandzhproduction at hadron colliders*, *Physical Review D* **68** (2003) . (cit. on p. 62)
- [124] A. Denner, S. Dittmaier, S. Kallweit and A. Mück, *Hawk 2.0: A monte carlo program for higgs production in vector-boson fusion and higgs strahlung at hadron colliders*, *Computer Physics Communications* **195** (2015) 161–171. (cit. on p. 62)
- [125] R.V. Harlander, A. Kulesza, V. Theeuwes and T. Zirke, *Soft gluon resummation for gluon-induced higgs strahlung*, *Journal of High Energy Physics* **2014** (2014) . (cit. on p. 62)
- [126] L. Altenkamp, S. Dittmaier, R.V. Harlander, H. Rzehak and T.J.E. Zirke, *Gluon-induced higgs-strahlung at next-to-leading order qcd*, *Journal of High Energy Physics* **2013** (2013) . (cit. on p. 62)
- [127] O. Brein, R.V. Harlander, M. Wiesemann and T. Zirke, *Top-quark mediated effects in hadronic higgs-strahlung*, *The European Physical Journal C* **72** (2012) . (cit. on p. 62)
- [128] R.V. Harlander, J. Klappert, S. Liebler and L. Simon, *vh@nnlo-v2: new physics in higgs strahlung*, *Journal of High Energy Physics* **2018** (2018) . (cit. on p. 62)
- [129] O. Brein, R.V. Harlander and T.J. Zirke, *vh@nnlo—higgs strahlung at hadron colliders*, *Computer Physics Communications* **184** (2013) 998–1003. (cit. on p. 62)
- [130] S. Frixione, V. Hirschi, D. Pagani, H.S. Shao and M. Zaro, *Electroweak and qcd corrections to top-pair hadroproduction in association with heavy bosons*, , 2015. (cit. on p. 62)
- [131] Y. Zhang, W.-G. Ma, R.-Y. Zhang, C. Chen and L. Guo, *Qcd nlo and ew nlo corrections tojmmml:math xmlns:mml="http://www.w3.org/1998/math/mathml" altimg="si1.gif" overflow="scroll" jmmml:mi \dot{z} tj/mml:mi \dot{z} jmmml:mover accent="true" jmmml:mrow \dot{z} jmmml:mi \dot{z} tj/mml:mi \dot{z} j/mml:mrow \dot{z} jmmml:mrow \dot{z} jmmml:mo stretchy="false" \dot{z} ⁻j/mml:mo \dot{z} j/mml:mrow \dot{z} j/mml:mover \dot{z} jmmml:mi \dot{z} hj/mml:mi \dot{z} j/mml:math \dot{z} product with top quark decays at hadron collider*, *Physics Letters B* **738** (2014) 1–5. (cit. on p. 62)
- [132] S. Dawson, C. Jackson, L.H. Orr, L. Reina and D. Wackerth, *Associated higgs boson production with top quarks at the cern large hadron collider: Nlo qcd corrections*, *Physical Review D* **68** (2003) . (cit. on p. 62)
- [133] W. Beenakker, S. Dittmaier, M. Krämer, B. Plümper, M. Spira and P. Zerwas, *Nlo qcd corrections to production in hadron collisions*, *Nuclear Physics B* **653** (2003) 151–203. (cit. on p. 62)
- [134] J. Bellm, S. Gieseke, D. Grellscheid, P. Kirchgæßer, F. Loschaj, G. Nail et al., *Herwig 7.1 release note*, , 2017. (cit. on p. 62)
- [135] A. Djouadi, J. Kalinowski and M. Spira, *HDECAY: a program for Higgs boson decays in the Standard Model and its supersymmetric extension*, *Comput. Phys. Commun.* **108** (1998) 56 [arXiv:hep-ph/9704448]. (cit. on p. 62)
- [136] M. Spira, *QCD Effects in Higgs Physics*, *Fortsch. Phys.* **46** (1998) 203 [arXiv:hep-ph/9705337]. (cit. on p. 62)

- [137] A. Djouadi, M.M. Mühlleitner and M. Spira, *Decays of Supersymmetric Particles: the Program SUSY-HIT (SUspect-SdecaY-Hdecay-InTerface)*, *Acta Phys. Polon. B* **38** (2007) 635 [arXiv:[hep-ph/0609292](#)]. (cit. on p. 62)
- [138] A. Bredenstein, A. Denner, S. Dittmaier and M.M. Weber, *Radiative corrections to the semileptonic and hadronic Higgs-boson decays $H \rightarrow WW/ZZ \rightarrow 4 \text{ fermions}$* , *JHEP* **02** (2007) 080 [arXiv:[hep-ph/0611234](#)]. (cit. on p. 62)
- [139] A. Bredenstein, A. Denner, S. Dittmaier and M.M. Weber, *Precise predictions for the Higgs-boson decay $H \rightarrow WW/ZZ \rightarrow 4 \text{ leptons}$* , *Phys. Rev. D* **74** (2006) 013004 [arXiv:[hep-ph/0604011](#)]. (cit. on p. 62)
- [140] A. Bredenstein, A. Denner, S. Dittmaier and M.M. Weber, *Precision calculations for the Higgs decays $H \rightarrow ZZ/WW \rightarrow 4 \text{ leptons}$* , *Nucl. Phys. Proc. Suppl.* **160** (2006) 131 [arXiv:[hep-ph/0607060](#)]. (cit. on p. 62)
- [141] T. Gleisberg and S. Höche, *Comix, a new matrix element generator*, *Journal of High Energy Physics* **2008** (2008) 039–039. (cit. on p. 63)
- [142] F. Buccioni, J.-N. Lang, J.M. Lindert, P. Maierhöfer, S. Pozzorini, H. Zhang et al., *Openloops 2*, *The European Physical Journal C* **79** (2019) . (cit. on p. 63)
- [143] F. Cascioli, P. Maierhöfer and S. Pozzorini, *Scattering amplitudes with open loops*, *Physical Review Letters* **108** (2012) . (cit. on p. 63)
- [144] A. Denner, S. Dittmaier and L. Hofer, *Collier: A fortran-based complex one-loop library in extended regularizations*, *Computer Physics Communications* **212** (2017) 220–238. (cit. on p. 63)
- [145] ATLAS Collaboration, *Studies on top-quark Monte Carlo modelling with Sherpa and MG5 a MC@NLO*, (cit.onp.63), , CERN, Geneva (2017).
- [146] M. Aliev, H. Lacker, U. Langenfeld, S. Moch, P. Uwer and M. Wiedermann, *Hathor – hadronic top and heavy quarks cross section calculator*, *Computer Physics Communications* **182** (2011) 1034–1046. (cit. on p. 63)
- [147] ATLAS Collaboration, *Performance of the atlas track reconstruction algorithms in dense environments in lhc run 2*, *The European Physical Journal C* **77** (2017) . (cit. on p. 68 and 92)
- [148] R. Frühwirth, *Application of kalman filtering to track and vertex fitting*, *Nuclear Instruments and Methods in Physics Research Section A: Accelerators, Spectrometers, Detectors and Associated Equipment* **262** (1987) 444. (cit. on p. 68)
- [149] ATLAS Collaboration, *Reconstruction of primary vertices at the atlas experiment in run 1 proton–proton collisions at the lhc*, *The European Physical Journal C* **77** (2017) . (cit. on p. 69)
- [150] ATLAS Collaboration, *Vertex Reconstruction Performance of the ATLAS Detector at $\sqrt{s} = 13 \text{ TeV}$* , (cit.onp.69), , CERN, Geneva (2015).
- [151] ATLAS Collaboration, *ATLAS Track and Vertex Reconstruction for Run-3 and High-Luminosity LHC*, . (cit. on p. 69)
- [152] ATLAS Collaboration, *Topological cell clustering in the atlas calorimeters and its performance in lhc run 1*, *The European Physical Journal C* **77** (2017) . (cit. on p. 69)

- [153] G. Aad, B. Abbott, D.C. Abbott, A.A. Abud, K. Abeling, D.K. Abhayasinghe et al., *Muon reconstruction and identification efficiency in atlas using the full run 2 pp collision data set at*

$$\sqrt{s} = 13$$

tev, The European Physical Journal C **81** (2021) . (cit. on p. 70 and 71)

- [154] M. Cacciari, G.P. Salam and G. Soyez, *The anti- k_t jet clustering algorithm*, *Journal of High Energy Physics* **2008** (2008) 063–063. (cit. on p. 72)

- [155] M. Aaboud, G. Aad, B. Abbott, J. Abdallah, O. Abdinov, B. Abeloos et al., *Jet reconstruction and performance using particle flow with the atlas detector*, *The European Physical Journal C* **77** (2017) . (cit. on p. 73)

- [156] *Jet energy scale and resolution measured in proton–proton collisions at*

$$\sqrt{s} = 13$$

tev with the atlas detector, The European Physical Journal C **81** (2021) . (cit. on p. 73)

- [157] *Jet energy scale measurements and their systematic uncertainties in proton-proton collisions at $\sqrt{s} = 13\text{ TeV}$ with the atlas detector*, *Physical Review D* **96** (2017) . (cit. on p. 73)

- [158] *Tagging and suppression of pileup jets*, (cit. on p. 73)
, CERN, Geneva (2014).

- [159] *Atlas b-jet identification performance and efficiency measurement with*

$$t\bar{t}$$

events in pp collisions at

$$\sqrt{s} = 13$$

tev, The European Physical Journal C **79** (2019) . (cit. on p. 74)

- [160] *Atlas flavour-tagging algorithms for the lhc run 2 pp collision dataset*, *The European Physical Journal C* **83** (2023) . (cit. on p. 74)

- [161] *Atlas flavour-tagging algorithms for the lhc run 2 pp collision dataset*, *The European Physical Journal C* **83** (2023) . (cit. on p. 74)

- [162] ATLAS Collaboration, *Transforming jet flavour tagging at ATLAS*, arXiv:[2505.19689](https://arxiv.org/abs/2505.19689). (cit. on p. 74 and 75)

- [163] ATLAS Collaboration, *Reconstruction, Identification, and Calibration of hadronically decaying tau leptons with the ATLAS detector for the LHC Run 3 and reprocessed Run 2 data*, (cit. on p. 75 and 76)
, CERN, Geneva (2022).

- [164] M. Aly, T. Dado, A. Held, M. Pinamonti and L. Valery, *TRExFitter (1.0.0)*, Zenodo (2025), [10.5281/zenodo.14849541](https://doi.org/10.5281/zenodo.14849541). (cit. on p. 77)

- [165] ROOT Collaboration, *HistFactory: A tool for creating statistical models for use with RooFit and RooStats*, CERN-OPEN-2012-016, New York U., New York (2012), DOI. (cit. on p. 77)

- [166] W. Verkerke and D. Kirkby, *The RooFit toolkit for data modeling*, arXiv:[physics/0306116](https://arxiv.org/abs/physics/0306116). (cit. on p. 77)

- [167] L. Moneta, K. Belasco, K. Cranmer, S. Kreiss, A. Lazzaro, D. Piparo et al., *The RooStats Project*, arXiv:1009.1003. (cit. on p. 77)
- [168] I. Goodfellow, Y. Bengio and A. Courville, *Deep Learning*, MIT Press (2016). (cit. on p. 78)
- [169] A. Hoecker, P. Speckmayer, J. Stelzer, J. Therhaag, E. von Toerne, H. Voss et al., *Tmva - toolkit for multivariate data analysis*, , 2009. (cit. on p. 79, 87, and 95)
- [170] J. Neyman and E.S. Pearson, *On the Problem of the Most Efficient Tests of Statistical Hypotheses*, *Phil. Trans. Roy. Soc. Lond. A* **231** (1933) 289. (cit. on p. 79)
- [171] A.L. Maas, *Rectifier nonlinearities improve neural network acoustic models*, 2013, <https://api.semanticscholar.org/CorpusID:16489696>. (cit. on p. 82)
- [172] D. Hendrycks and K. Gimpel, *Gaussian error linear units (gelus)*, , 2023. (cit. on p. 82)
- [173] S. Ioffe and C. Szegedy, *Batch normalization: Accelerating deep network training by reducing internal covariate shift*, , 2015. (cit. on p. 84)
- [174] D.P. Kingma and J. Ba, *Adam: A method for stochastic optimization*, , 2017. (cit. on p. 84)
- [175] D.E. Rumelhart, G.E. Hinton and R.J. Williams, *Learning representations by back-propagating errors*, *Nature* **323** (1986) 533. (cit. on p. 84)
- [176] M. Abadi, A. Agarwal, P. Barham, E. Brevdo, Z. Chen, C. Citro et al., *TensorFlow: Large-scale machine learning on heterogeneous systems*, , 2015. Software available from tensorflow.org. (cit. on p. 84 and 110)
- [177] A. Paszke, S. Gross, F. Massa, A. Lerer, J. Bradbury, G. Chanan et al., *Pytorch: An imperative style, high-performance deep learning library*, , 2019. (cit. on p. 84)
- [178] D. Guest, J. Smith, M. Paganini, M. Kagan, M. Lanfermann, A. Krasznahorkay et al., *lwtnn: v2.13*, . 10.5281/zenodo.597221. (cit. on p. 85)
- [179] D.H. Guest, J.W. Smith, M. Paganini, M. Kagan, M. Lanfermann, A. Krasznahorkay et al., *lwtnn/lwtnn: v2.14.1*, , Dec., 2024. 10.5281/zenodo.14276439. (cit. on p. 85)
- [180] F. Pedregosa, G. Varoquaux, A. Gramfort, V. Michel, B. Thirion, O. Grisel et al., *Scikit-learn: Machine learning in python*, , 2018. (cit. on p. 85)
- [181] Coadou, Yann, *Boosted decision trees and applications*, *EPJ Web of Conferences* **55** (2013) 02004. (cit. on p. 86)
- [182] T. Chen and C. Guestrin, *Xgboost: A scalable tree boosting system*, in *Proceedings of the 22nd ACM SIGKDD International Conference on Knowledge Discovery and Data Mining*, KDD '16, (New York, NY, USA), p. 785–794, Association for Computing Machinery, 2016, DOI. (cit. on p. 87)
- [183] ATLAS Collaboration, *ATLAS Event Displays Public Repository*, Available at https://atlaspo.cern.ch/public/event_display/, 2025. (cit. on p. 90)
- [184] ATLAS Collaboration, *Electron reconstruction and identification in the ATLAS experiment using the 2015 and 2016 LHC proton-proton collision data at $\sqrt{s} = 13$ TeV*, *Eur. Phys. J. C* **79** (2019) 639 [arXiv:1902.04655]. (cit. on p. 91, 95, 96, 103, 104, 105, and 119)
- [185] ATLAS Collaboration, *Electron and photon reconstruction and performance in ATLAS using a dynamical, topological cell clustering-based approach*, (cit. on p. 91), , CERN, Geneva (2017).

- [186] W. Lampl, S. Laplace, D. Lelas, P. Loch, H. Ma, S. Menke et al., *Calorimeter Clustering Algorithms*, (cit. on p. 91) , CERN, Geneva (2008).
- [187] R. Frühwirth, *Application of kalman filtering to track and vertex fitting, Nuclear Instruments and Methods in Physics Research Section A: Accelerators, Spectrometers, Detectors and Associated Equipment* **262** (1987) 444. (cit. on p. 92)
- [188] ATLAS Collaboration, *Electron and photon performance measurements with the ATLAS detector using the 2015-2017 LHC proton-proton collision data*, *JINST* **14** (2019) P12006 [arXiv:1908.00005]. (cit. on p. 93 and 95)
- [189] L.M. Flores, *Identifying electrons and searching for electroweak r-parity violating supersymmetry at atlas*, , June, 2022. (cit. on p. 96)
- [190] ATLAS Collaboration, *Identification of electrons using a deep neural network in the ATLAS experiment*, (cit. on p. 97, 99, 103, 107, 110, and 111) , CERN, Geneva (2022).
- [191] TAGANDPROBE *software for e/γ reconstruction and identification measurements*, . (cit. on p. 98)
- [192] A. Carnelli, F. Deliot and H. Bachacou, *Qualification task report: charge flip rejection study using a DNN*, (cit. on p. 104) , CERN, Geneva (2023).
- [193] J.E. Puddefoot, *Electron identification and Tuning in preparation for Run-3*, (cit. on p. 105) , CERN, Geneva (2021).
- [194] ATLAS Collaboration, *Electron and photon efficiencies in lhc run 2 with the atlas experiment*, *Journal of High Energy Physics* **2024** (2024) . (cit. on p. 121)
- [195] E.M. Rüttinger, *Electron identification efficiency and W+W cross section measurements with the ATLAS detector*, Ph.D. thesis, Sheffield U., year =. 10.1007/978-3-319-73930-4. (cit. on p. 124)

Appendix

In a paper, an appendix is used for technical details that would otherwise disturb the flow of the paper.

List of Acronyms

- ALICE** A Large Ion Collider Experiment. 32
- ATLAS** A Toroidal LHC ApparatuS. 32, 34–36
- BEH** Brout–Englert–Higgs. 10, 12
- BSM** Beyond the Standard Model. 23, 28
- CERN** Conseil Européen pour la Recherche Nucléaire. 31
- CKM** Cabibbo-Kobayashi-Maskawa. 13, 15, 16
- CMS** Compact Muon Solenoid. 32
- DM** dark matter. 14
- EW** Electroweak. 8, 10, 12, 15, 16
- ggF** gluon-gluon fusion. 16, 23
- LHC** Large Hadron Collider. 12, 16–19, 21, 22, 24, 31, 32, 34
- LHCb** LHC beauty. 32
- LO** leading order. 16, 20
- PDF** parton distribution function. 7, 8
- QCD** Quantum Chromodynamics. 4, 6, 8, 20, 22
- QED** Quantum Electrodynamics. 6, 12
- SM** Standard Model. 3, 4, 14–16, 18, 20–22, 24, 25, 28, 29, 31, 43
- WIMP** weakly interacting massive particle. 14

Acknowledgements

The **atlaslatex** package contains the acknowledgements that were valid at the time of the release you are using. These can be found in the **acknowledgements** subdirectory. When your ATLAS paper or PUB/CONF note is ready to be published, download the latest set of acknowledgements from:

<https://twiki.cern.ch/twiki/bin/view/AtlasProtected/PubComAcknowledgements>